HEAT TRANSFER TO A VAPOR BUBBLE SUSPENDED NEAR OR ATTACHED TO A SOLID PLATE

by

Lin Huang

A dissertation submitted to the Graduate Faculty in Engineering
in partial fulfillment of the requirements for the degree of
Doctor of Philosophy, The City University of New York

1996

The manuscript has been read and accepted for the Graduate Faculty in Engineering in satisfaction of the dissertation requirement for the degree of Doctor of Philosophy.

6/28/96
Date

Professor
Chair of Examination Committee

6/28/96
Date

Professor Gerard G. Lowen
Executive Officer

Prof. Zeev Dagan Mentor
Prof. David Rumschitzki
Co-Mentor
Prof. Charles Maldarelli
Prof. Peter Ganatos
Prof. Demetrius Papageorgiou
Department of Mathematics
New Jersey Institute of Technology

The City University of New York

ABSTRACT

HEAT TRANSFER TO A VAPOR BUBBLE SUSPENDED NEAR OR ATTACHED TO A SOLID PLATE

by Lin H[illegible]g

Advisers: Professor Zeev Dagan & Professor David Rumschitzki

This thesis examines the dramatic heat transfer enhancement relative to vapor-bubble-free heat transfer associated with the nucleate boiling incipience. When the vapor-liquid interface is at equilibrium, we find that the heat transfer at small Reynolds, Peclet, Capillary and Bond numbers is conductive and quasi-static, and the bubble is spherical. We find that this mechanism alone is sufficient to account for the observed enhancements and their experimentally observed scalings, without recourse to convective models. We examine embryonic vapor bubbles in the liquid that are either attached or adjacent to a nearby heating solid plate. The solid plate and liquid layer are both of finite depth and one may freely prescribe the temperatures on their far surfaces. Both layers may either be finite or infinite in the transverse direction. The former with periodic boundary conditions mimics bubble-bubble interactions of an evenly distributed collection of identical vapor bubbles. Different physical and geometrical settings reveal the fundamental mechanism of the nucleate pool boiling heat transfer. They include different conductivity ratio of the liquid and solid; different solid and liquid layer thicknesses; different contact angles when the bubble is attached to the solid-liquid interface and the distances from the bubble to the solid-liquid interface when bubble is detached; and most importantly, different numbers of bubbles per unit area.

We use these quasi-static calculations to follow the growth of an incipient bubble from micron to millimeter size and examine how its size scales with time and how the heat transfer scales with bubble density and wall superheat. We

calculate a postiori and carefully follow all of the non-dimensional groups and confirm that the Capillary and Bond numbers do/indeed/remain small throughout the bubble growth until before the gravitational forces become important. The Reynolds and Peclet numbers, based on the bubbles radius, are quite large in many cases suggesting that in the bulk liquid the heat transfer might be convective and the flow turbulent. However, a careful investigation of the heat fluxes reveals that even though there is significant fluid convection near the bubble apex, practically all of the heat transfer to the bubble takes place in a very small region, near the contact line of an attached bubble. Using a local length to characterize the scales in this region leads to Peclet (and Reynolds) numbers that are indeed small in the region where the vast majority of the heat transfer takes place, thus ensuring the accuracy of the magnitude of the calculated heat transfer enhancement affiliated to conduction.

Acknowledgment

Special thanks go to Professor Zeev Dagan, who has led me through this challenging yet exciting process to solve the mystery of boiling, one of the most commonly observed yet the least understood phenomenon which had defied human curiosity since the time our fire making ancestor first walked the earth. I also express my gratitude to Professor David Rumschitzki, who took time to guide me, painstakingly, through every step to perfect this dissertation, not only technically, but also grammatically. Without his effort, it would be impossible to have this dissertation in its present form. I would also like to thank Professor Peter Ganatos, who has the reputation of being always very kind and truly helpful to every student in the department, and Professor Charles Maldarelli, for his invaluable comments and suggestions.

I would also like to thank Professor Gerard G. Lowen, the Excecutive Officer of the Ph.D Programs in the School of Engineering, particularly, for his constant support and administrative guidance which has made the whole course of studying at the City College a unique and an enjoyable experience in my life.

It has been my mother's dream to see her children achieving the highest degree in education, as her husband, who suffers the Alzheimer's disease, did a half century ago. However, the political turmoil in China during the 60's and 70's had deprived her children of rights to receive such an education. Only Xiaoping Deng's "Open Door Policy" would make her dream come true.

This research was partially funded by grant from _____ and partially from The City University of New York

Table of Contents

List of Tables and Figures

Chapter III

Chapter IV

Chapter I

Chapter II

Chapter III

Chapter IV

Chapter V

Chapter I

INTRODUCTION

Boiling heat transfer has attracted considerable interest since the 1930's due to the rapid advancement of modern engineering applications in high power, high density systems such as nuclear reactors and rocket engineering. In addition, the microelectronics industry has succeeded in greatly increasing circuit integration density, thereby creating heat dissipation problems. Nevertheless, a comprehensive theory of boiling that can predict the rate of heat transfer from a solid interface to a liquid is still unavailable. The limited progress in the theoretical understanding of this fundamental problem stems from the fact that complex interactions of hydrodynamic and thermal processes that are intractable by conventional mathematical techniques characterize boiling heat transfer. The widely scattered results stemming from apparently identical experiments only highlight the frustration experimentalists and engineers experience. The proposed research aims to develop a mathematical model that can elucidate the heat transfer enhancement mechanism in nucleate boiling.

Figure I.1, a plot of the heat flux from a heating solid to a liquid versus the superheating of the wall above the liquid's saturation temperature, is a typical boiling curve. With small wall superheating ($(T_w - T_{sat}) \leq 4°C$), natural convection buoys the slightly less dense, hotter fluid near the heating surface upwards, thereby drawing cooler fluids towards the surfaces. At about 4°C superheating, vapor bubbles begin to form in the heating surface's irregularities, but not until about 9°C superheating do these bubbles interact to form jets and columns of bubbles. The single and multiple bubble phenomena comprise the nucleate boiling regime, which extends to about 30°C superheat. Beyond 30°C, there is a hysteresis regime called transit boiling followed, at about 200°C by film boiling.

To deal with the proposed boiling heat transfer problem we shall focus on a theory for pool boiling heat transfer in the nucleate boiling regime. In many respects, nucleate pool boiling heat transfer is the simplest mode of boiling, compared with transition or flow boiling heat transfer, because its scalings decouple the heat transfer from the hydrodynamics. Yet, it has defied rigorous theoretical analysis due to the intricate bubble growth process and irregular bubble geometry.

The commonly accepted mechanism (Figure I.2) for nucleate boiling heat transfer enhancement is similar to that of natural convection. That is, a vapor bubble displaces hot liquid around it upwards as it forms and draws cooler fluid to its underside as it detaches. We shall argue that long before this convective phenomena becomes important, conduction to an incipient attached or just detached micro-bubble and bubble-bubble interactions can already account for a two order of magnitude heat transfer enhancement. Thus, we argue, that conduction to the contact line region for attached bubble and through the thin film separating a just-detached bubble from the heating solid, is the primary mechanism of nucleate boiling heat transfer enhancement.

The growth of an embryonic vapor bubble near a solid-liquid interface has been the subject of extensive study for its fundamental importance in understanding the phenomena of heterogeneous nucleate boiling incipience and boiling heat transfer. Hsu and Graham (1976) review most of the early work on this subject. Because the thermal and hydrodynamic processes couple non-linearly, and because of the complicated, transient geometry of the liquid-vapor interface, this problem has defied exact theoretical analysis. Similarly, due to the complexity of local geometric and physical properties, together with the difficulties in accurate temperature and heat flux measurements at micro scales, You *et al.* (1990) show wildly scattered experimental nucleate boiling incipience results for ostensibly

identical conditions. Local property variations must then play a prominent role in the observed heat transfer at overall apparently identical conditions.

For a small bubble at its infancy stage with small Peclet and Bond numbers, surface tension and hydrodynamic forces determine the interfacial geometry (Forster and Zuber, 1955), while inertial and gravitational effects are negligible. Under these conditions the interface retains a nearly spherical shape, and the instantaneous radius characterizes the instantaneous bubble geometry. Previous bubble phase change studies have concentrated on spherically symmetric bubble growth problems, although this shape is well justified only for bubbles in unbounded media (Scriven, 1959). Fyodorov and Klimenko (1989) solve the heat transfer problem of a spherical bubble growing tangent to a plane at vanishing contact angle. Their model attempts to examine the heat transfer in the micro-layer region between the bubble and the adjacent solid-liquid boundary. Lee and Nydahl (1989) attack this problem more directly by considering a spherical vapor bubble and a conical liquid micro-layer near a solid plate. Several other numerical studies consider bubble growth with various simplifications (Madhaven and Mesler, 1970; Guy and Ledwidge, 1973; Zijl *et al.* 1979). Kim and Kaviany (1990) offer a numerical technique that can treat a large class of phase-change problems with moving boundaries, but apply it only to Scriven's case of a spherical bubble in an unbounded liquid. Recently, Sadhal (1989) has presented the first analytical solution for conductive heat transfer to a vapor bubble growing slowly, i.e., quasistatically due to liquid evaporation, on or near a solid boundary in toroidal and bipolar coordinate systems. Although Sadhal's elegant solutions reveal the important role that solid thermal properties play in determining the conductive heat transfer rate, the solutions require unbounded domains and far field temperatures in both the solid and liquid that are each uniform and equal to each other. With these limitations, Sadhal's solutions cannot describe the most important cases when heat input derives solely from the solid wall and a positive heat flux exists

across the solid-liquid interface; and when multiple nearby bubbles co-exist and interact with each other hydrodynamically and thermally. Both of these cases are fundamental to the boiling heat transfer problem, and our work will address them.

In order to simplify the problem we examine the nucleate boiling regime by focusing on a single nucleate vapor bubble in a transversely infinite domain or, to model bubble-bubble interactions, periodically distributed vapor bubbles on or near a solid heating wall. The solution of this heat transfer problem will establish the local conditions that initiate and regulate the process of boiling. We shall then examine a slowly growing bubble from its infancy stage towards its departure from the solid-liquid interface, but only up to the point where the fluid mechanics become important. The heat transfer problem associated with this growing bubble will reveal how the local conditions regulate bubble growth, the importance of conductive heat transfer and how the growing bubbles interact with each other. The most relevant measure is the consequent heat transfer enhancement from incipient nucleate boiling, and its thorough study should determine the dominant fundamental mechanism of nucleate boiling heat transfer.

Figure I.1

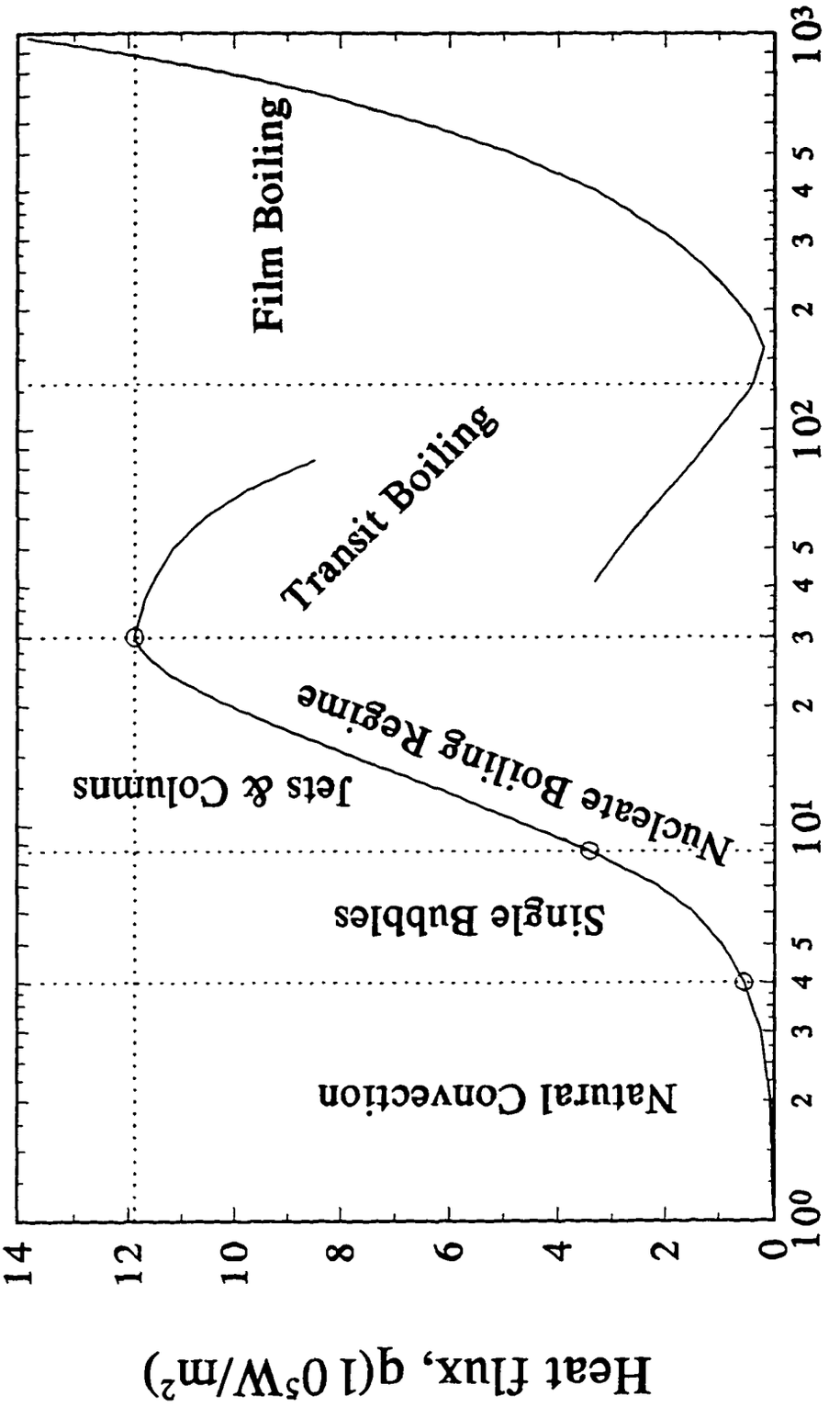

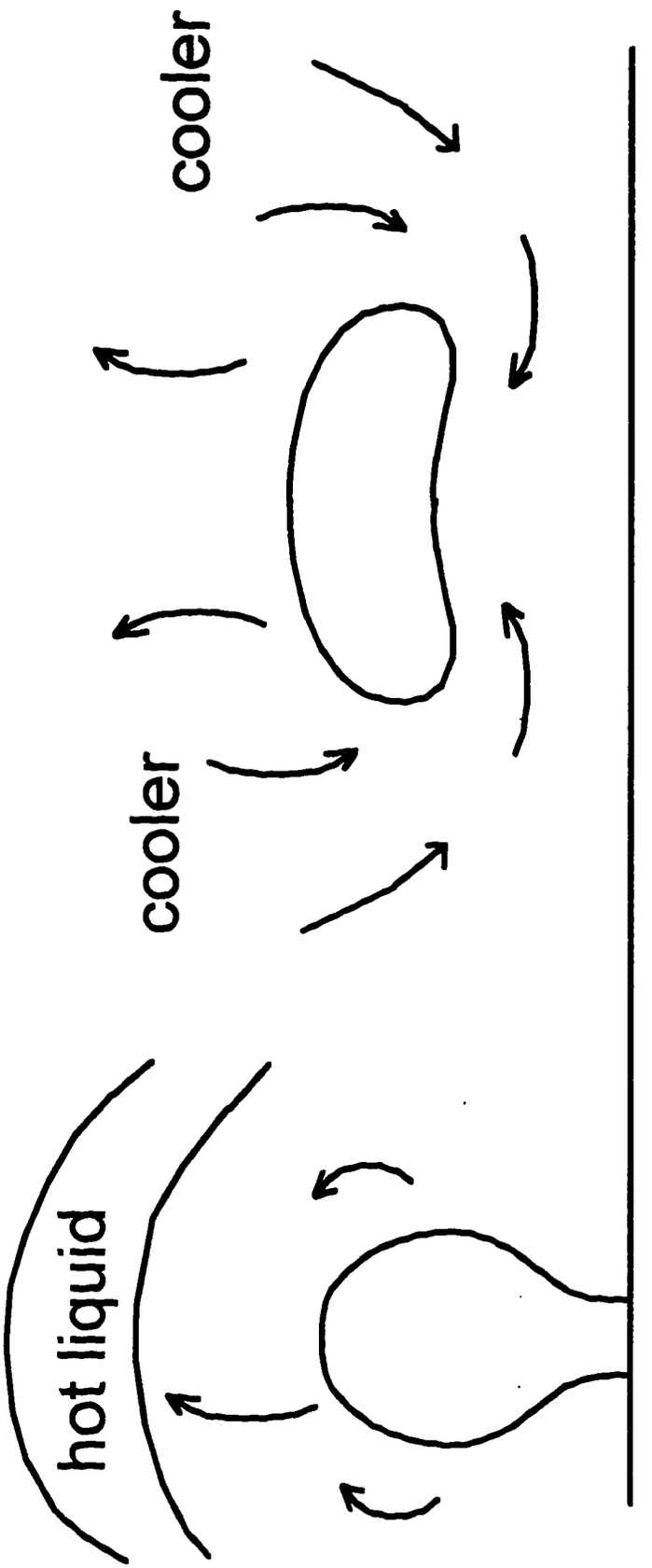

Figure I.2 Agitation

Chapter II

GENERAL FORMULATION

II.1 Four Distinct Cases

II.1.1 Suspended Bubble in Semi-infinite Domains

The proposed study consists of a series of related problems of increasing complexity. The simplest problem is the conductive heat transfer to a spherical vapor bubble embryo suspended in a liquid layer near a solid plate, both of finite thickness. As boundary conditions one may specify either the temperatures or the heat fluxes far from the liquid-solid interface. This situation can model the regions close to a heating wall. Free buoyant flows, sometimes violent and turbulent, homogenize the bulk liquid temperature. However, a lack of sufficient convective heat transfer within the viscous boundary layer can lead to a steep temperature gradient near the solid heating wall. That is, within both the thermal and viscous boundary layers, conductive heat transfer can prevail and one can assume a uniform temperature gradient across the composite structure. It is natural to examine the influence that the solid and liquid thermal properties, the cross-layer heat flux and the local geometry (such as the distance from the bubble to the heating wall and the thickness of solid and liquid layers) exerts on the bubble's growth rate. The first solution uses a multipole collocation technique to calculate the effects of these parameters on the Nusselt number, the dimensionless efficiency of heat transfer to the vapor bubble. This solution should reduce to Sadhal's result when the solid and liquid thicknesses are sufficiently large and overall temperature gradient vanishes.

II.1.2 Suspended Bubble in a Finite Cell

The above single bubble-infinite lateral domain approach cannot examine how increasing lateral bubble density changes the rate of heat transfer. Thus the

second problem employs a boundary integral representation to repeat the above calculations on a domain that is laterally bounded and periodic. Adjusting the cell size mimics the effect of having nearby, evenly distributed bubbles. It allows one to assess if the interaction between the neighboring bubbles is an important nucleate boiling heat transfer mechanism. Large cell calculations should agree with the collocation results. It is natural then to ask if there is a qualitative difference in the heat transfer if the bubble is attached to the solid interface and thus maintains a dry spot there.

II.1.3 Attached Bubble in a Finite Cell

The third problem extends the previous calculations by allowing a spherical vapor bubble segment to be attached to the solid-liquid interface, inside a finite, composite, periodic cell at quasistatic conditions. This situation is markedly more complex and requires special care because the contact line surrounding the dry spot between the vapor and the heating solid presents both geometrical and physical singularities. In order to overcome these singularities, the calculation requires the temperature gradient profile to asymptotically approach a limit related to Sadhal's analytical solution close to the contact line and utilizes a special mesh technique there to accomplish this. Again, by increasing both the radius and the thicknesses of the cell and equating both far field temperatures, the solutions should converge to the Sadhal's attached bubble results. On the other hand, the cases where the size of the cell approaches that of the bubble challenge the legitimacy of requiring the limit based on Sadhal's solution, which was derived for infinite lateral domains, to describe the contact line region. We derived an analytical approach to resolve the small cell problem's asymptotics as well. These solutions, relevant to strong bubble-bubble interactions, explain the observed dramatic heat transfer enhancements at bubble incipience.

II.1.4 Slow Growing Bubble in Finite Cell

Finally, our future work will depart from the completely quasistatic frame work above; it will follow slow bubble growth from incipience to the point where either the fluid mechanics becomes important or the bubble Bond number becomes large enough for gravity to elongate it and with capillarity, to cause it to snap off, whichever comes first. We impose small enough overall temperature gradients so that growth is slow and fluid flow is unimportant as long as possible. Thus the free surface is always in the equilibrium shape that surface tension and gravity alone dictate. This model's goal is to predict the bubble emission frequency, bubblr size upon detachement and the overall heat transfer enhancement during a bubble's life cycle.

II.2 Scales

Consider a vapor bubble of radius a' on or near a solid-liquid interface. The thicknesses of the solid and liquid layers are h′ for the solid and H′ for the liquid. The solid and liquid densities and thermal conductivities are ρ_s, κ_s and ρ_ℓ, κ_ℓ respectively. For the vapor phase, we consider the limiting case where its density, viscosity and thermal diffusivity are much smaller than those for the liquid. So, the behaviors of the vapor and liquid phases decouple. The distance d′ from the planar solid-liquid interface to the center of the spherical bubble is positive (negative) when the bubble's center is above (bellow) the interface. The system may be either infinite in extent in the directions parallel to the solid-liquid interface or, for the bubble-bubble interaction calculations, finite and of size R'_c with periodic temperature distributions that one mimics by using an insulating boundary condition there. We consider only axisymmetric bubbles and so the "periodic" cell, despite abuse of geometry, is a cylinder of radius R'_c, with center at the center of the bubble and height h′+H′. Let's define both cylindrical (R', Z', ψ) and spherical

(r', θ, ψ) coordinate systems with origins at the center of the spherical bubble. Axisymmetry disallows any ψ dependence.

In principle, the growth of an incipient vapor bubble is an unsteady conductive/convective heat transfer problem with a moving interface. The volume changes by virtue of local evaporation of liquid along the liquid-vapor boundary and the interface moves by virtue of both evaporation and flow kinematics. One cannot specify the instantaneous shape of this boundary, but rather its determination is part of the problem solution. However, the major application of these calculations is to the boiling water, and for sufficiently small vapor bubbles the problem simplifies significantly. Even under the assumption that interfacial vaporization is instantaneous and that the liquid-vapor interface is everywhere always at the saturation temperature T_v', vapor bubble growth still has four characteristic time scales; their relative sizes dictate the simplifications that are appropriate. The time scale over which the liquid of thermal diffusivity α_ℓ conducts heat over distances characteristic of the bubble radius a' is $t_d \cong a'^2/\alpha_\ell$. Viscosity ν_ℓ diffuses vorticity and characteristic fluid motions over time scales $t_\nu \cong a'^2/\nu_\ell$, and surface tension σ acts on the interfacial shape against viscosity over times $t_s \cong (a'\rho_\ell \nu_\ell)/\sigma$. Finally, the bubble grows over a time scale $t_g \cong a'/\dot{a}'$ where $\dot{a}'$ represents the characteristic time rate of change of the bubble's radius. In our problem, the fluid properties and the far field temperatures specify this quantity. Thus, if h_{fg} is the heat of vaporization of the liquid of specific heat c_ℓ and thermal conductivity $\kappa_\ell = \rho_\ell c_\ell \alpha_\ell$, $T_{s\ell}' := \dfrac{T_f' \kappa h' + T_s' H'}{\kappa h' + H'}$ is the steady solid-liquid interfacial temperature in the absence, i.e., far from, a bubble, and $\Delta T' := T_{s\ell}' - T_v' = \dfrac{(T_f' - T_v')\kappa h' + (T_s' - T_v')H'}{\kappa h' + H'}$; then, $\dot{a}'$ is simply $\dot{a}' = \kappa_\ell \Delta T' / (a' \rho_v h_{fg})$.

Our focus is to describe the system over time scales of the order t_d. If $t_g \cong a'/\dot{a}' >> t_v \cong a'^2/\nu_\ell$, and $t_g \cong a'/\dot{a}' >> t_d \cong a'^2/\alpha_\ell$, then the bubble growth is slow relative to both heat transfer and fluid motions; thus one may treat the problem quasistatically. That is, the steady state temperature and fluid velocity fields apply at each instantaneous bubble size. The first inequality is equivalent to $Re := a'\dot{a}'/\nu_\ell << 1$, and the second to $Pe := a'\dot{a}'/\alpha_\ell = RePr_\ell << 1$ (the Prandtl number $Pr_\ell := \nu_\ell/\alpha_\ell$). This latter condition also states that convective heat transfer is insignificant with respect to conductive transfer. Finally, if $t_s \cong (a'\rho_\ell\nu_\ell)/\sigma << t_g \cong a'/\dot{a}'$, or $Ca = u'\mu/\sigma << 1$, then the bubble is always at its Young-Laplace shape, which, for small Bond number $Bond := (g\Delta\rho a'^2)/\sigma$, is simply spherical.

For water at one atmospheric pressure under saturation conditions, $h_{fg} = 2257$ kJ/kg, $\rho_v = 0.60$ kg/m^3, $\rho_\ell = 958$ kg/m^3, $c_\ell = 4216$ J/kg/°K, $\alpha_\ell = 0.168 \times 10^{-6}$ m^2/s, $\nu_\ell = 0.2818\times10^{-6}$ m^2/sec, $\sigma = 0.0589$ kg/s^2, and $\kappa_\ell = 0.680$ J/m/°K/s. With these parameters, one has:

$$Pr_\ell = \nu_\ell/\alpha_\ell \cong 1.$$

$$Re = \frac{a'\dot{a}'}{\nu_\ell} \cong \frac{\kappa_\ell \Delta T'}{\nu_\ell \rho_v h_{fg}} \cong \frac{0.68 \times \Delta T'}{0.2818 \times 10^{-6} \times 0.60 \times 2.257 \times 10^6} = 1.8 \times \Delta T',$$

$$Pe = \frac{a'\dot{a}'}{\alpha_\ell} = Re\frac{\nu_\ell}{\alpha_\ell} = RePr_\ell \cong \frac{Re \times 0.2818 \times 10^{-6}}{0.1684 \times 10^{-6}} = 3.03 \times \Delta T'.$$

Obviously, both Pe and Re numbers can be very small if the temperature difference $\Delta T'$ is sufficiently small. For the Ca number, we have,

$Ca = u'\mu/\sigma \cong \dot{a}'\nu_\ell\rho_\ell/\sigma \cong \frac{\kappa_\ell \Delta T'}{\rho_v h_{fg}} \frac{\nu_\ell \rho_\ell}{\sigma a'} \cong 2.3 \times 10^{-9} \times \frac{\Delta T'}{a'}$, which can be small if $\Delta T'$ ensures small Pe and Re, and if $a' >> (10^{-9})\ \Delta T'$. These conditions guarantee

that the Capillary number is small so the surface tension prevails over flow throughout, and the bubbles maintain Young-Laplace shapes.

Finally, if Bond number is small, the bubble always keeps a spherical shape. Under the above conditions, it is easy to see that $Bond = \frac{g\Delta\rho a'^2}{\sigma} = \frac{9.8 \times 957}{0.0589} \times a'^2 = 0.16 \times 10^6 \times a'^2$. So, for sub-millimeter bubbles, i.e., $10^{-9}\Delta T' << a' << 10^{-3}$, gravity does not affect the bubble shape significantly and they remain spherical as long as the other assumptions hold.

II.3 Governing Equation and Boundary Conditions

For the case of Dirichlet boundary condition at the far solid wall, it is convenient to define the dimensionless (unprimed) temperature as $T_\pm := (T'_\pm - T'_v)/(T'_s - T'_v)$, where the subscripts + and - denote the liquid and solid phases, respectively, and subscripts $v\ell$, $s\ell$ and vs denote boundary conditions at the two-phase interfaces (s = solid, ℓ = liquid, v = vapor), while subscripts f and s denote boundary conditions at the liquid free surface and the far solid wall, respectively. If the boundary condition at the far solid wall is a Neumann one, with the dimensional heat flux j_s given there, then one can use the same dimensionless temperature, but T_s is now a calculated quantity for the bubble-free system. The spherical vapor bubble's radius a' scales all coordinates and lengths, and $\kappa := \kappa_\ell/\kappa_s$. We denote all the dimensional length and temperature scales with primes, and all dimensionless ones without primes.

For the scalings as in the last subsection, the governing equations for both the liquid and solid regions are:

$$\nabla^2 T_\pm = 0. \qquad \text{(II.0)}$$

The non-dimensional boundary conditions are: On the liquid free surface the temperature is a uniform, prescribed constant, due to the existence of a thermal

sublayer next to a uniform liquid bulk temperature. On the solid wall, one can either prescribe a constant temperature or a constant flux.

$$\begin{cases} \begin{cases} T_+ = T_f & \text{at} \quad Z = H - d \\ T_- = T_s & \text{at} \quad Z = -h - d \end{cases} & \text{Dirichlet} \\ \dfrac{\partial T_-}{\partial Z} = j_s := \dfrac{j_s' a'}{\kappa_s (T_s' - T_v')} \quad \text{at} \quad Z = -h - d & \text{Neumann.} \end{cases} \qquad \text{(II.1)}$$

Note that, due to the higher solid thermal conductivity, if the solid plate is not sufficiently thin, the flux and temperature on the solid wall are almost uniform. So, for simplicity, we shall present mainly results for the case of a prescribed temperature on the solid wall. On the liquid-solid interface, the temperature and heat flux are continuous,

$$\kappa \nabla T_+ \cdot \vec{n} = \nabla T_- \cdot \vec{n} \quad \text{and} \quad (T_{s\ell} :=) T_+ = T_- \text{ at} \quad Z = -d, \qquad \text{(II.2)}$$

where $\vec{n}$ is a unit normal vector perpendicular to the solid-liquid interface, and the liquid-vapor interface of the bubble is at the uniform saturation temperature T_v, i.e.,

$$(T_{v\ell} :=) T_+ = 0 \quad \text{at} \quad r = 1, Z \geq -d. \qquad \text{(II.3)}$$

If the bubble is attached to the solid interface with a contact angle φ, there will be a solid-vapor interface as well. In this case, the temperatures and heat fluxes should also be continuous. However, since we assume that $\rho_v << \rho_\ell$, $\kappa_v << \kappa_\ell$, these conditions simply reduce to a single, insulating boundary condition, i.e.,

$$\frac{\partial T_+}{\partial Z} = 0 \quad \text{at} \quad Z = -d, \quad \text{for} \quad 0 \leq R \leq \sin\varphi. \qquad \text{(II.4)}$$

For finite cell configurations, periodicity requires the radial flux on the lateral cell boundary to be zero, or

$$\frac{\partial T_{\pm}}{\partial R} = 0 \qquad R = R_c. \qquad \text{(II.5)}$$

Finally, in the future work we shall need a kinematic-evaporative boundary condition to allow calculations of the position of the moving vapor-liquid interface. We shall discuss this condition when we come to that problem.

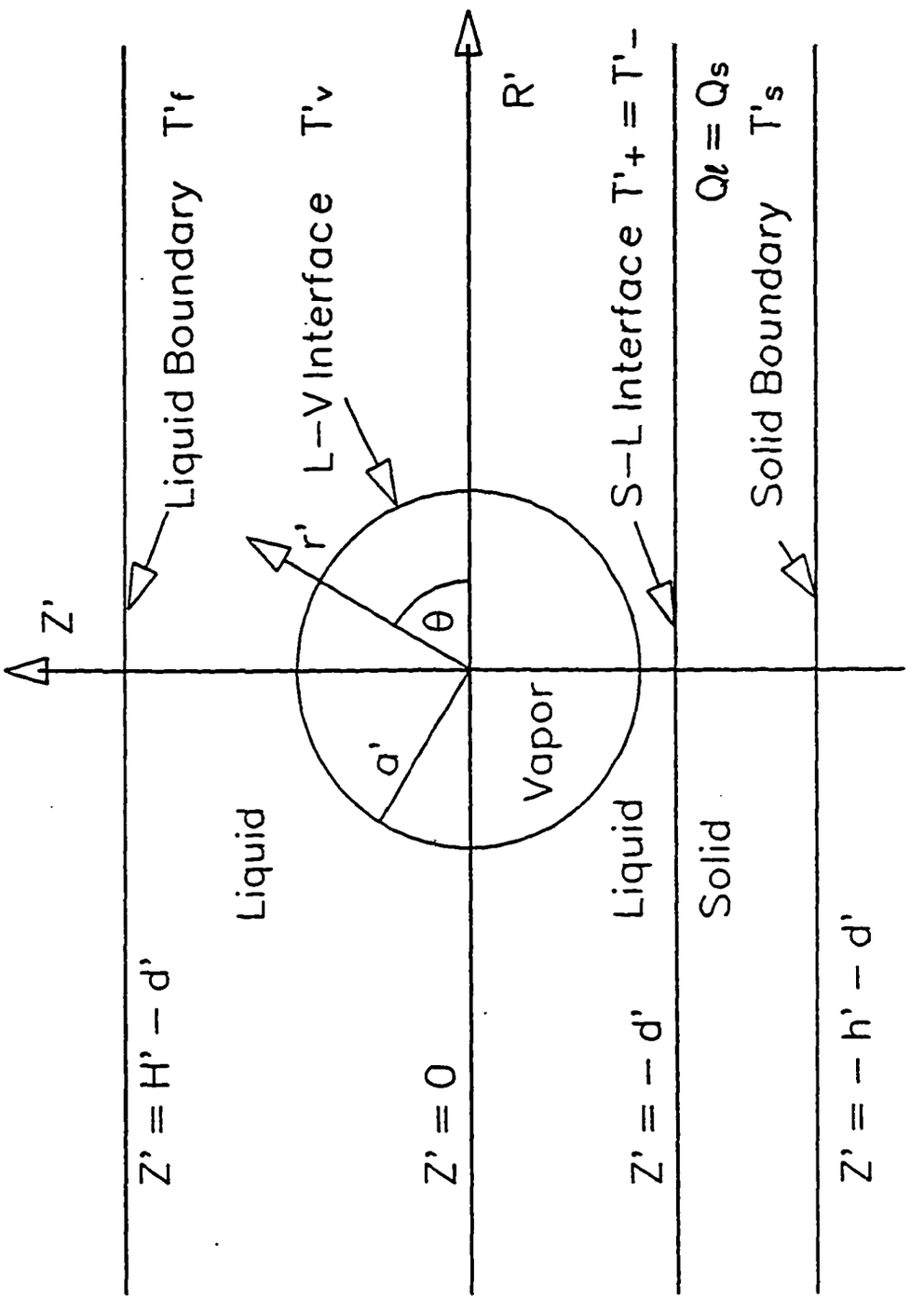

Figure II.1 Suspended Bubble In Semi–Infinite Liquid

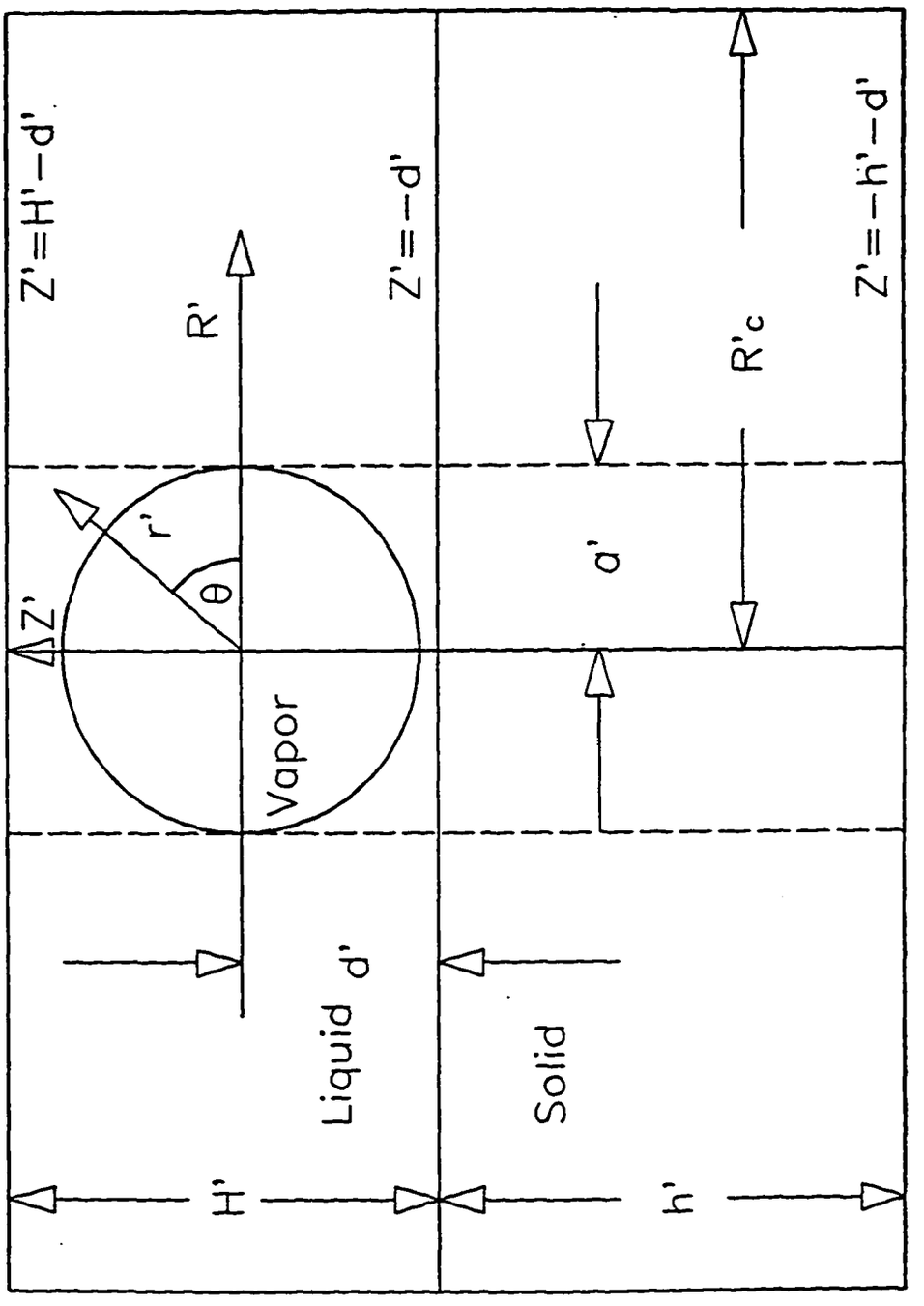

Figure II.2 Suspended Bubble in Finite Cell

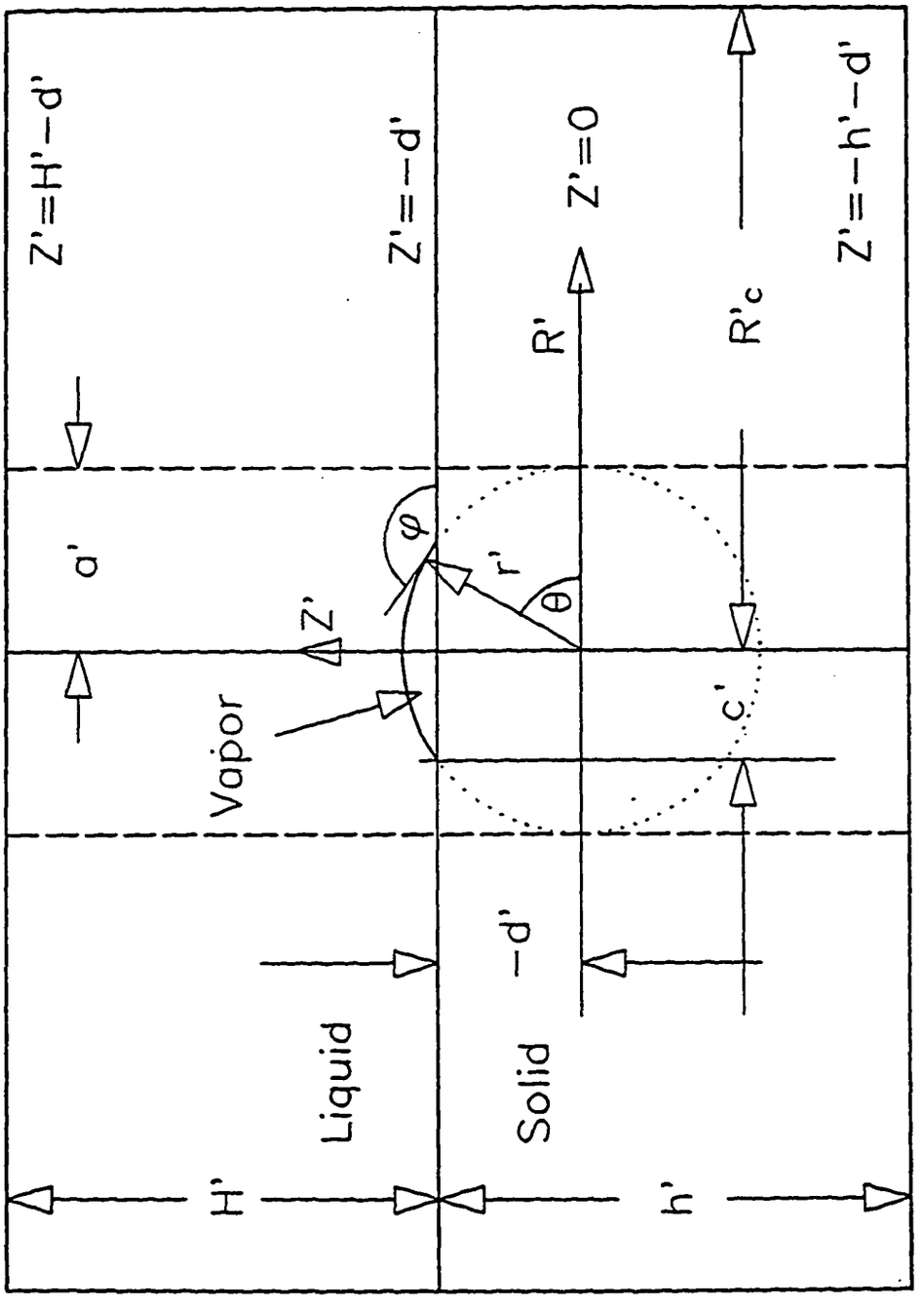

Figure II.3 Attached Bubble In Cell

Chapter III

HEAT TRANSFER TO A SPHERICAL BUBBLE SUSPENDED IN A LIQUID LAYER ADJACENT TO A SOLID WALL BOTH OF FINITE THICKNESS

III.1 Formulation

Let us begin with the case of a spherical bubble near, but not attached to the solid-liquid interface. The purposes for this calculation are:

1) To set up a new practical mathematical model to deal with a suspended vapor bubble in a fluid of finite depth. The solutions provide a measure of the heat transfer enhancement that the vapor bubble's presence near the heating wall creates and the corresponding instantaneous bubble growth rate it drives;

2) To clearly delineate how the system parameters, i.e., the cross interface temperature difference, the solid-liquid conductivities, the solid and liquid thicknesses and the bubble position, affect the heat transfer enhancement and bubble growth rate;

3) To establish a bridge between Sadhal's existing analytical solution for the solid and liquid layers of infinite thicknesses and extents parallel to the solid-liquid interface and the proposed solutions for layers of finite thicknesses and finite R_e. The present solution has limiting cases that should match both of these solutions.

As long as the bubble is spherical, there exists a particularly efficient method of solution. We employ a multipole collocation technique based on the superposition of the two fundamental solutions of the steady heat conduction equation in spherical and in cylindrical coordinates, together with a linear temperature field that is valid far from the vapor bubble.

$$T_+ = E_+ + F_+ Z + T_+^{spherical} + T_+^{cylindrical} \qquad \text{liquid} \qquad \text{(III.1)}$$

$$T_- = E_- + F_- Z + T_-^{cylindrical} \qquad \text{solid.} \qquad \text{(III.2)}$$

The superscripts *spherical* and *cylindrical* denote the corresponding fundamental solutions

$$T_+^{cylindrical} = \int_0^\infty [c_1(\chi)\cosh\chi(Z+d) + c_2(\chi)\sinh\chi(Z+d)]J_0(\chi R)d\chi, \quad \text{(III.3)}$$

$$T_-^{cylindrical} = \int_0^\infty [c_3(\chi)\cosh\chi(Z+d) + c_4(\chi)\sinh\chi(Z+d)]J_0(\chi R)d\chi, \quad \text{(III.4)}$$

$$T_+^{spherical} = \sum_{n=0}^\infty \frac{a_n P_n(\sin\theta)}{r^{n+1}}. \quad \text{(III.5)}$$

Here $J_0(\chi R)$ is Bessel function of order zero and $P_n(\sin\theta)$ is the n^{th} Legendre polynomial. The boundary conditions determine the constants $E_\pm$ and $F_\pm$ and the functions $c_1(\chi)$, $c_2(\chi)$, $c_3(\chi)$, $c_4(\chi)$ of χ. Upon application of the boundary conditions at the far liquid and solid surfaces and at the liquid-solid interface, one can rewrite the solutions in terms of a single set of coefficients $\{a_n\}$ (see section III.2 for details). For the case of a prescribed temperature at the far solid surface, the solutions are,

$$T_+ = E_+ + F_+ Z + \sum_{n=0}^\infty a_n \{\frac{P_n(\sin\theta)}{r^{n+1}} - \int_0^\infty \frac{\chi^n J_0(\chi R)}{F(\chi) n!} d\chi$$
$$[(-1)^n \sinh\chi(H-Z-d)\,(\cosh\chi h - \kappa\sinh\chi h)\, e^{-\chi d} + \quad \text{(III.6)}$$
$$+ (\cosh\chi h\, \sinh\chi(Z+d) + \kappa\sinh\chi h\, \cosh\chi(Z+d))\, e^{-\chi(H-d)}]\}$$

$$T_- = E_- + F_- Z +$$
$$+ \kappa\sum_{n=0}^\infty a_n \int_0^\infty \frac{[(-1)^n e^{\chi(H-d)} - e^{-\chi(H-d)}]\sinh\chi(h+Z+d)\,\chi^n J_0(\chi R)}{F(\chi) n!} d\chi, \quad \text{(III.7)}$$

where

$$F(\chi) = \cosh\chi h\, \sinh\chi H + \kappa\sinh\chi h\, \cosh\chi H, \quad \text{(III.8)}$$

$$E_+ = \frac{T_f(d+\kappa h) + H - d}{H+\kappa h},\ E_- = \frac{T_f\kappa(d+h) + H - \kappa d}{H+\kappa h},\ F_+ = \frac{F_-}{\kappa} = \frac{T_f - 1}{H+\kappa h}. \quad \text{(III.9)}$$

Note that

$$T_{\pm} = E_{\pm} + F_{\pm} Z \qquad \text{as} \qquad \sqrt{Z^2 + R^2} \to \infty. \tag{III.10}$$

Similar equations hold for the case of a prescribed heat flux at the far solid surface. The final boundary condition (II.3) requiring $T_{+v} = 0$ on the spherical interface determines the infinite set of constant coefficients $\{a_n\}$ that remains. A numerical multipole collocation technique applies this boundary condition on the spherical bubble interface. We repeat the numerical computations with increasing numbers of discrete boundary collocation points on the spherical interface until the

$$Q'_v = 2\pi\kappa_\ell a'^2 \int_0^\pi \frac{\partial T'_+}{\partial r'} \cos\theta d\theta$$ the bubble,

$$Q'_v = 2\pi\kappa_\ell a'^2 \int_0^\pi \frac{\partial T'_+}{\partial r'} \cos\theta d\theta \tag{III.11}$$

in its dimensional form, becomes independent of the number of collocation points. A convenient way to represent the results and to compare them with the bubble free case, is to express the solution in terms of the dimensionless Nusselt number which is the ratio of the actual heat transferred to the bubble to a characteristic amount based on the solid's far face's temperature and the liquid's conductivity.

$$Nu = \frac{Q'_v}{4\pi a' \kappa_\ell (T'_s - T'_v)} = \frac{1}{2} \int_0^\pi \frac{\partial T_+}{\partial r} \cos\theta d\theta . \tag{III.12}$$

In order to present the problem's solutions for all values of the free liquid surface temperature T_f, we exploit the linearity of the problem and write the general solution as a linear combination of two specific cases. The first temperature field $T^1_{\pm}$ is the solution of original problem with the temperature T_f on the liquid free surface, Z = H-d, set to one in (II.4). This situation describes a bubble at constant temperature $T_v = 0$ with the far liquid and solid surfaces at the

higher temperature $T_f = T_s = 1$. The second case $T_{\pm}^0$ differs only in that the liquid free surface temperature is $T_f = 0$. Here, both the bubble and the liquid free surface are at the saturation, $T_f = T_v = 0$, while the temperature $T_s = 1$ on the plate at $Z = -(d + h)$ is higher. The solution for an arbitrary liquid free surface temperature T_f is

$$T_{\pm} = T_{\pm}^1 T_f + T_{\pm}^0 (1 - T_f). \qquad \text{(III.13)}$$

Note that $c_1(\chi),...,c_4(\chi)$ are independent of T_f but the applications of Equation (III.6) and (III.7), on the other hand, are not.

III.2 Numerical Collocation Procedure

Below we describe the technique used to determine the unknown coefficients in Equations (III.3), (III.4) and (III.5). First, Hankel transforming the four boundary conditions (II.1) and (II.2) on the planar surfaces solves for the unknown functions $c_1(\chi),...,c_4(\chi)$ exactly in terms of the Legendre expansion coefficients $\{a_n\}$. Second, the application of the multipole collocation technique to the boundary condition on the spherical interface determines these Legendre coefficients.

In order to carry out this application of boundary conditions (II.1), (II.2) and (II.4), one must rewrite the spherical solution (III.5) in cylindrical coordinates via the coordinate transformation $\sin\theta = Z/\sqrt{Z^2 + R^2}$, and $r = \sqrt{R^2 + Z^2}$. Consequently, these boundary conditions become

$$\sum_{n=0}^{\infty} \frac{a_n P_n\left(\dfrac{H-d}{\sqrt{R^2 + (H-d)^2}}\right)}{\left[R^2 + (H-d)^2\right]^{(n+1)/2}} + \qquad \text{(III.14)}$$

$$+ \int_0^{\infty} \left[c_1(\chi)\cosh\chi H + c_2(\chi)\sinh\chi H\right] J_0(\chi R)\, d\chi = 0$$

$$\kappa\sum_{n=0}^{\infty}\frac{\partial}{\partial Z}\left(\frac{a_n P_n\left(\frac{Z}{\sqrt{R^2+Z^2}}\right)}{\left[R^2+Z^2\right]^{(n+1)/2}}\right)\Big|_{Z=-d}-\int_0^{\infty}\left[c_4(\chi)-\kappa c_2(\chi)\right]\chi J_0(\chi R)d\chi=0 \qquad \text{(III.15)}$$

$$\sum_{n=0}^{\infty}\frac{a_n P_n\left(\frac{-d}{\sqrt{R^2+d^2}}\right)}{\left[R^2+d^2\right]^{(n+1)/2}}+\int_0^{\infty}\left[c_1(\chi)-c_3(\chi)\right]J_0(\chi R)d\chi=0 \qquad \text{(III.16)}$$

$$\int_0^{\infty}\left[c_3(\chi)\cosh\chi h-c_4(\chi)\sinh\chi h\right]J_0(\chi R)d\chi=0, \qquad \text{(III.17)}$$

on the liquid free surface (III.14), the solid-liquid interface (III.15, III.16) and the far solid surface (III.17). A Hankel transformation allows analytical inversion with the integral identity

$$\int_0^{\infty}P_n\left(\frac{1}{\left[\rho^2+Z^2\right]^{(n+1)/2}}\frac{Z}{\sqrt{\rho^2+Z^2}}\right)\rho J_0(\rho\chi)d\rho=\frac{\chi^{n-1}}{n!}\left(\frac{|Z|}{Z}\right)^n e^{-\chi|Z|}. \qquad \text{(III.18)}$$

(III.14-III.16) result in three expressions for the functions $c_1(\chi),\ldots,c_4(\chi)$ in terms of the unknown constant coefficients $\{a_n\}$, while Equation (III.17) yields $c_3(\chi)\cosh\chi h = c_4(\chi)\sinh\chi h$. Together, one has four linear algebraic equations for the four unknown functions. Substitution back into equations (III.3)-(III.5) yields the temperature fields (III.6) - (III.7).

To satisfy the remaining boundary condition (II.3) on the bubble interface, one substitutes for the cylindrical coordinates (R,Z) in terms of the spherical coordinates, $R = r\cos\theta$ and $Z = r\sin\theta$ in Equation (III.6) and sets $r = 1$ to get

$$\sum_{n=0}^{\infty}a_n\{P_n(\sin\theta)-\int_0^{\infty}\frac{\chi^n J_n(\chi\cos\theta)}{F(\chi)n!}d\chi[((-1)^n\sinh\chi(H-\sin\theta-d)$$
$$(\cosh\chi h-\kappa\sinh\chi h)e^{-\chi d}+(\cosh\chi h\sinh\chi(\sin\theta+d)+ \qquad \text{(III.19)}$$
$$\kappa\sinh\chi h\cosh\chi(\sin\theta+d))e^{-\chi(H-d)}]\}=-(E_+ + F_+\sin\theta)$$

We now apply the multipole collocation technique, that Gluckman *et al.* (1971) and Ganatos *et al.* (1980) developed and that Chen *et al.* recently (1991) applied in a study of thermo-capillary motion of a sphere in a tube, to determine the remaining set of unknown constant coefficients $\{a_n\}$. The collocation procedure keeps only a_0 through a_{M-1} in the summation, and solves for them by requiring that (III.19) be exactly satisfied at M discrete collocation points θ_i: $i = 0,...,M-1$ on the surface of the sphere. The result is a set of M linear algebraic equations for the M coefficients a_i: $i = 0,...,M-1$. To select the collocation points for $-\pi/2 < \theta < \pi/2$, each of which, due to the geometric symmetry, actually describes a ring on the sphere, one begins by selecting a point at each pole, $\theta_0 = \pi/2$ and $\theta_{M-1} = -\pi/2$. To avoid singular behavior at the equator $\theta = 0$, one selects two points, $\theta = \pm\varepsilon$ with $\varepsilon = 0.01°$ as collocation points. Finally one completes the node selection by subdividing the quadrants into arcs of equal length. At each θ_i, one evaluates the integrals in (III.19) numerically, and solves the resulting set of equations by a standard matrix inversion technique. When M is sufficiently large we find the numerical values of $\{a_n\}$ begin to converge.

Our numerical computations proceed until achieving convergence to four significant digits. To check the accuracy of the computation, we compare our computations for $T_f = 1$, $H = h \to \infty$ with Sadhal's (1989) analytical solution for a bubble in a semi-infinite liquid medium near a solid wall of infinite thickness, with $T_f = T_s = 1$. Our calculations approximate the semi-infinite geometries by setting both thicknesses of the liquid and solid layers be 10^{20}. Table III.1 presents the Nusselt number *Nu* results for four values 0.001, 0.01, 0.1 and 2.0, of the conductivity ratio κ, for increasing numbers of collocation points M and for decreasing value of the dimensionless gap thickness δ. For large gap thicknesses ($\delta > 0.25$) the computations converge to Sadhal's exact result with only eight collocation points. The number of collocation points required to achieve the

desired accuracy increases with decreasing gap thickness δ. The smallest gap thickness considered ($\delta = 0.001$) requires 56 collocation points to obtain three significant digit accuracy when $\kappa = 0.001$. As the conductivity ratio κ increases, the calculation requires fewer points for the same accuracy. For example, $\kappa = 2.0$ only requires 12 collocation points for the desired accuracy. Clearly, the convergence rate is faster, i.e., M is smaller, when the temperature field is more uniform and contains no steep temperature gradients. When the gap thickness and the liquid conductivity are small, such steep temperature gradients appear in the region between the bubble interface and the solid plate and thus require a larger number of collocation points (more terms in the series) to accurately describe the temperature field. For a gap thickness smaller than $\delta = 0.001$, the numerical computations become prohibitively long, and the collocation technique is not always viable.

III.3 Results for the Spherical Bubble Adjacent to a Heating Wall

Let us begin with a brief discussion of how the temperature profiles vary with the parameters before moving on to the Nusselt numbers. Figures III.1 shows the dimensionless temperature distributions at the solid-liquid interface as a function of the cylindrical radial distance R for $H = h = 5$ for various values of κ and δ. For small gaps δ and poorly conducting solids (κ is large), there are lateral temperature gradients, and thus lateral heat transfer at the solid-liquid interface beneath the bubble. These gradients disappear beyond a bubble radius and are relatively insensitive to the far away free liquid interface temperature T_f. Inversely, at large δ or smaller κ, the solid-liquid interface becomes isothermal.

Due to the large number of geometric and thermal parameters that influence the heat transfer, we focus our attention on several distinct cases which provide sufficient qualitative information on the general thermal behavior of the present system. We present the results as plots (Figure III.2 - III.4) of Nusselt

number versus the ratio κ of liquid to solid conductivities, with the distance $\delta = (d' - a')/2a'$ between the bubble and the solid wall and the larger thickness H as parameters. There are nine figures corresponding to three ratios of thickness of 0.1, 1 and 10, each for $T_f = 1$, $T_f = 0$ and $T_f = -1$. By far the most important of the parameters is the distance δ between the bubble and the solid-liquid interface. All of the Figure III.2 - III.4 show an up to a factor of four increase in the Nusselt number for $\delta = 0.001$ for highly conducting solids (small κ) and any value of $H > 3$ or T_f. This *Nu* enhancement effect disappears quickly. By the time the position of the bubble is one bubble diameter away from the solid-liquid interface ($\delta = 1$), the Nusselt number is about one or less. For $T_f = -1$, it can even go negative as more heat escapes from the bubble towards the free surface than enters it from solid, particularly for thin liquid layers (H small). Sadhal (1989) showed that for the unbounded geometry, $Nu = 1$ when the conductivities of the liquid and solid are equal, and is insensitive to all other parameters.

The next most important effect is the ratio of conductivities. All of the figures show a decrease in the Nusselt number enhancement as the solid conductivity decreases. Alternately, as κ_s increases (κ decreases from 0.1), the Nusselt number increases, almost linearly on this semi-log plot and more severely for smaller δ, and then levels off, becoming independent of κ. Note that the smaller δ, the larger the regime of κ where Nu seems to be linear in ln(κ). In fact, for zero bubble-solid gap thickness, Sadhal (1989) found that to the leading order in κ,

$$Nu \approx -\ln(2\kappa) \qquad \text{(III.20)}$$

The physical basis for Nu becomes independent of κ for non-zero distance between the bubble and the solid-liquid interface is that for sufficiently small κ, the solid is not an effective barrier to heat transfer (compare the isotherms in figure IV.8 with those in IV.9 for the same T_f). Thus the solid-liquid interface is almost at T_s and

the entire temperature jump $T_s - T_v$ transpired over the distance between the bubble and the solid-liquid interface. Since it is the temperature gradient near the bubble which characterizes the heat transfer, further decrease in κ does not affect Nusselt number. As the ratio H/h goes up, the solid layer becomes thinner and this is similar to a small increase in κ_s; this effect is only significant for large κ, since at small κ *Nu* is independent of κ.

Due to the choice of de-dimensionalization, varying H is the way one accesses the effect of bubble size. From the figures, for vanishingly small bubbles (H large), the solution approaches Sadhal's since the bubble does not feel the finiteness of the layer thickness (see Figure III.2a - III.4a). The comparison with Sadhal is only meaningful for $T_s = T_f = 1$, since that is the only case to which Sadhal's solution applies. For large bubbles, bubble size is only significant if the bubble fills almost the entire distance between the solid-liquid and the liquid free surfaces.Increasing the bubble size (decreasing H) brings the liquid free surface closer to the bubble. For $T_f = 1$, the liquid free surface is a source of heat for the bubble and thus bringing it closer increases Nusselt number. On the other hand, for $T_f < 1$, the liquid free surface is a heat sink that competes with bubble, and bring it closer has the opposite effect. It also leads to a lower value of Nusselt number relative to $T_f = 1$ due to reduced heating. In fact for $T_f = -1$, it lowers Nu by actually cooling the bubble, but only when the liquid is effectually conducting relative to the solid (large κ). These effects are only noticeable for very thin liquid layers.

Table III.1: Comparison of the exact (Sadhal, 1989) and collocation Nusselt numbers for (a) $\kappa = 0.001$, (b) $\kappa = 0.01$ (c) $\kappa = 0.1$, and (d) $\kappa = 2.0$

No. M of points	$\delta = 0.5$	$\delta = 0.25$	$\delta = 0.1$	$\delta = 0.01$	$\delta = 0.001$
8	1.3401	1.5336	1.8614	3.0902	9.3481
12			1.8615	2.8998	5.5669
20			1.8615	2.8824	4.1830
36				2.8833	3.9651
44					3.9628
52					3.9642
56					3.9649
Exact	1.3401	1.5337	1.8615	2.8833	3.9669

(a) $\kappa = 0.001$

No. M of points	$\delta = 0.5$	$\delta = 0.25$	$\delta = 0.1$	$\delta = 0.01$	$\delta = 0.001$
8	1.3319	1.5185	1.8297	2.8913	5.5848
12		1.8298	2.7477	4.1509	4.1509
20			1.8298	2.7353	3.5765
36				2.7360	3.4915
44					3.4917
52					3.4939
Exact	1.3319	1.5185	1.8298	2.7360	3.4939

(b) $\kappa = 0.01$

No. M of points	$\delta = 0.5$	$\delta = 0.25$	$\delta = 0.1$	$\delta = 0.01$	$\delta = 0.001$
8	1.2617	1.3943	1.5894	1.9746	2.1288
12			1.5895	1.9571	2.0754
20			1.5895	1.9565	2.0657
36				1.9566	2.0659
44					2.0660
Exact	1.2617	1.3943	1.5895	1.9566	2.0660

(c) $\kappa = 0.1$

No. M of points	$\delta = 0.5$	$\delta = 0.25$	$\delta = 0.1$	$\delta = 0.01$	$\delta = 0.001$
8	0.9235	0.9012	0.881	0.865	0.8632
12					0.8633
Exact	0.9235	0.9012	0.881	0.865	0.8633

(d) $\kappa = 2.0$

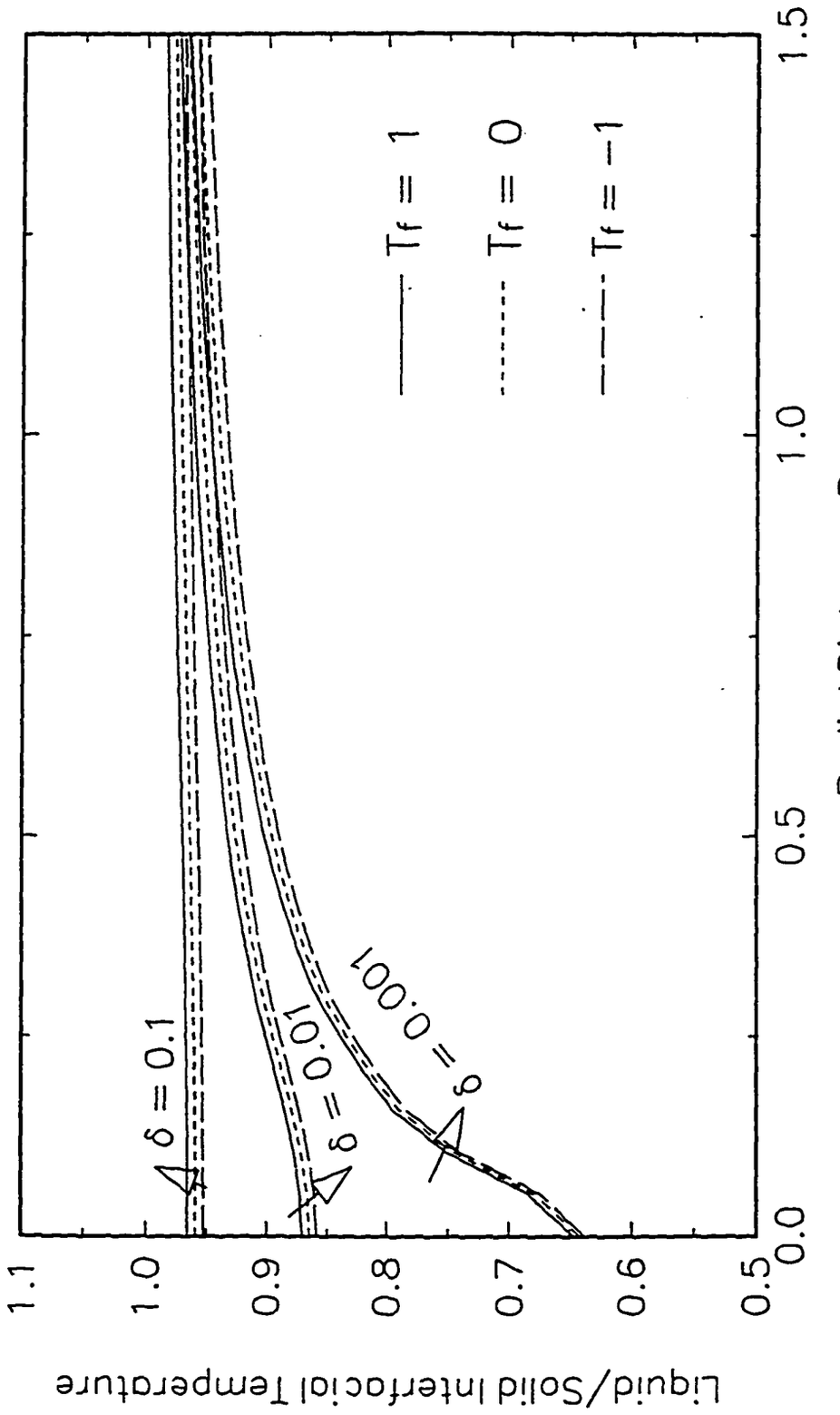

Figure III.1 (a)

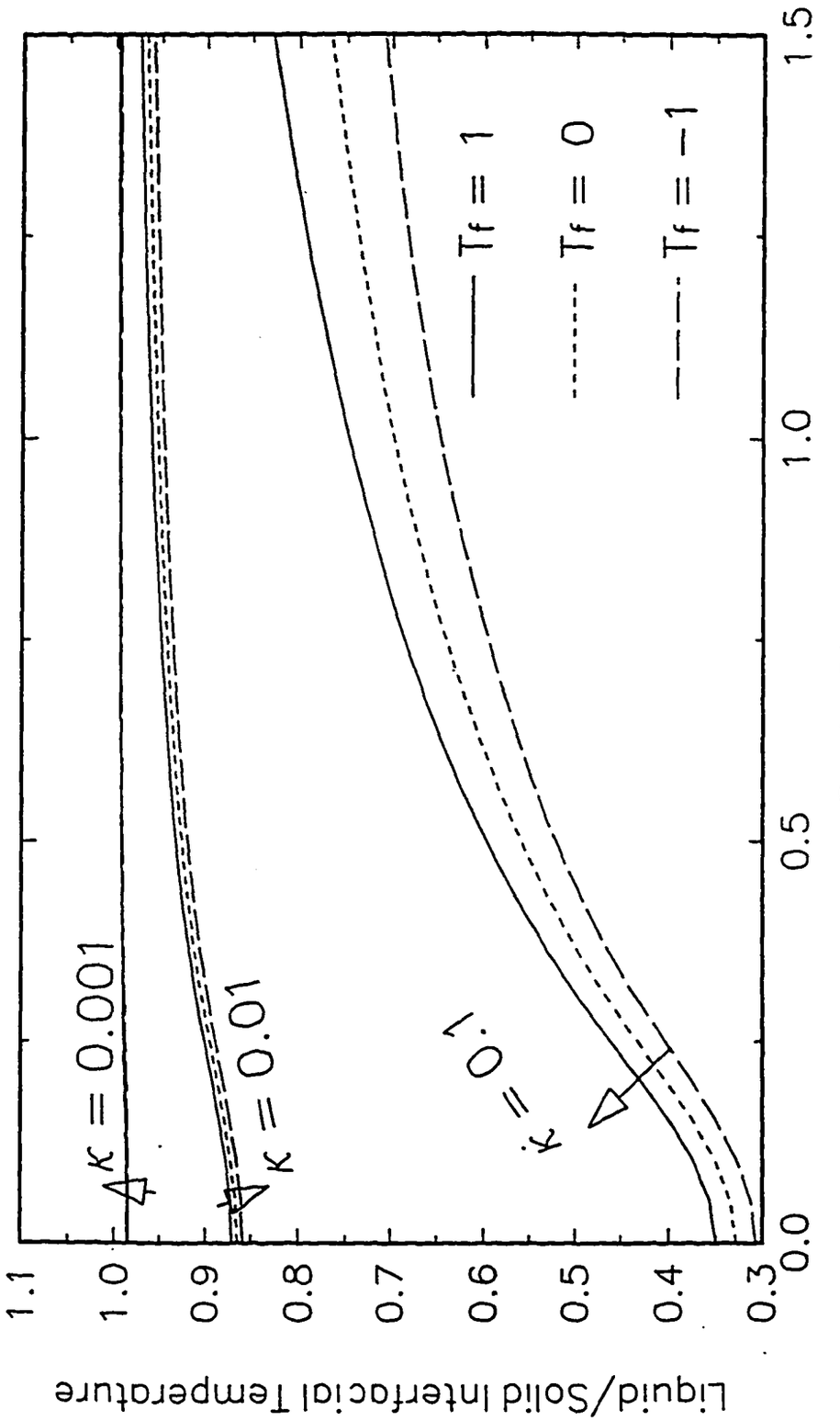

Figure III.1 (b)

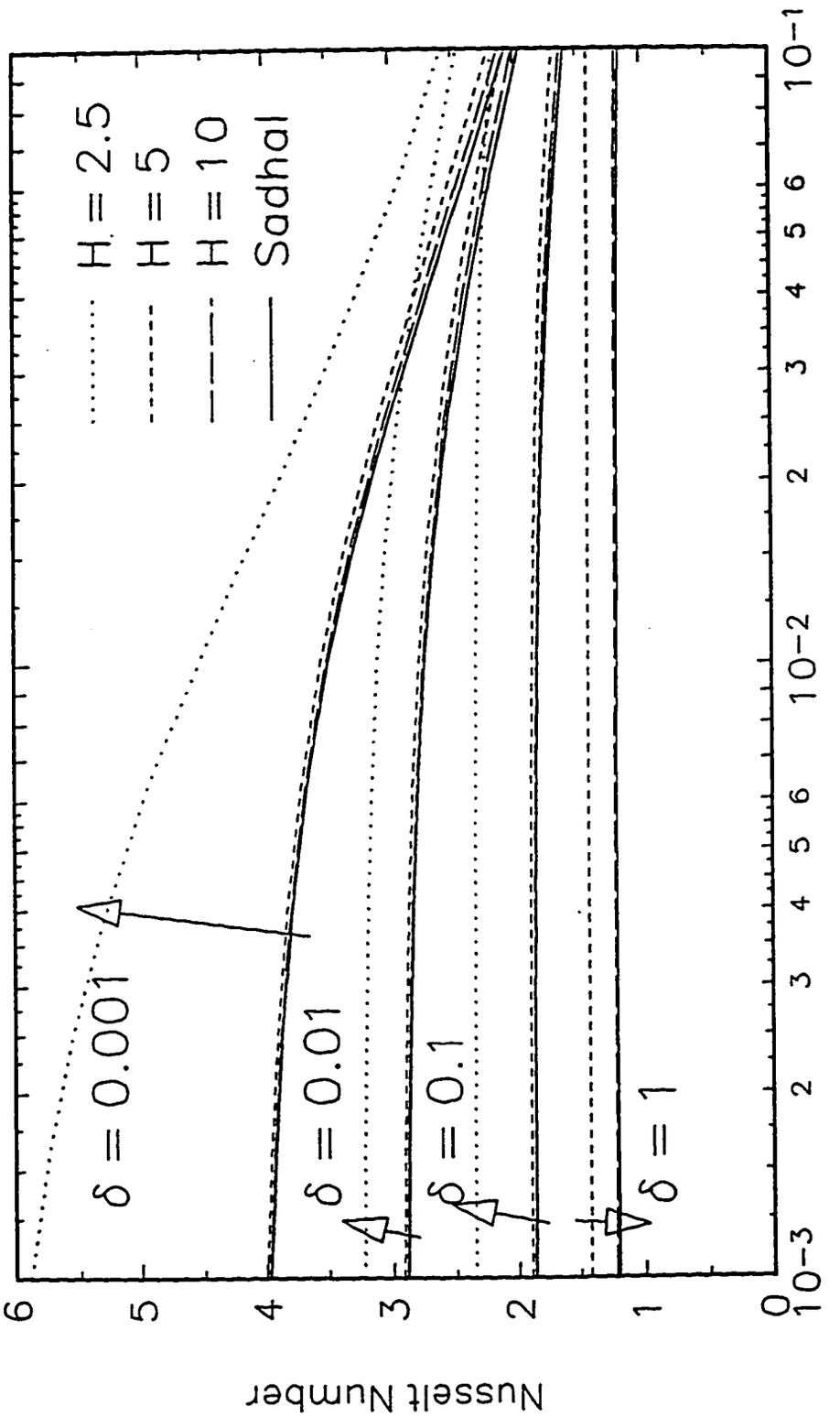

Figure III.2(a)
$T_f=1$, $T_s=1$, $h/H=1$

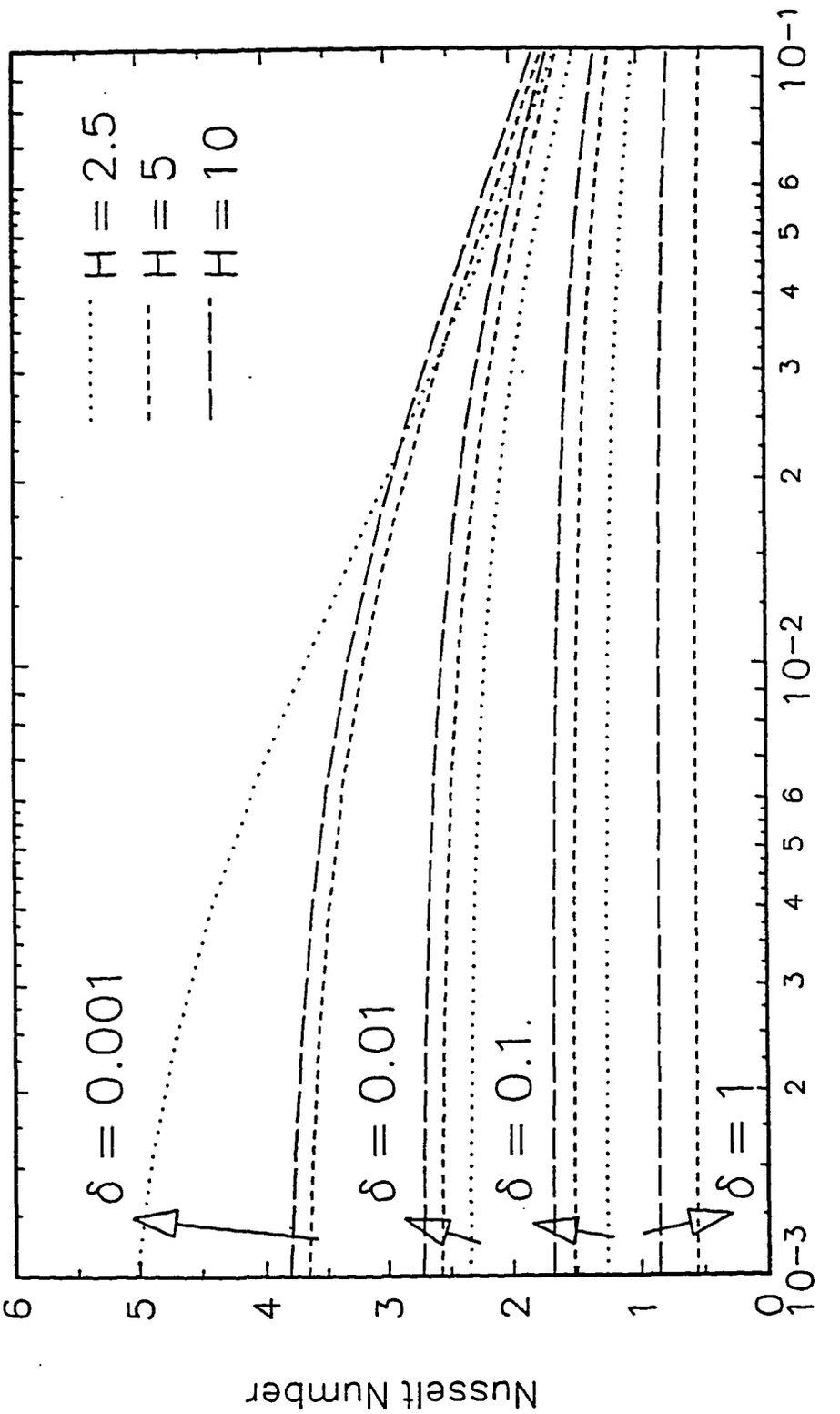

Figure III.2(b)
$T_f=0$, $T_s=1$, $h/H=1$

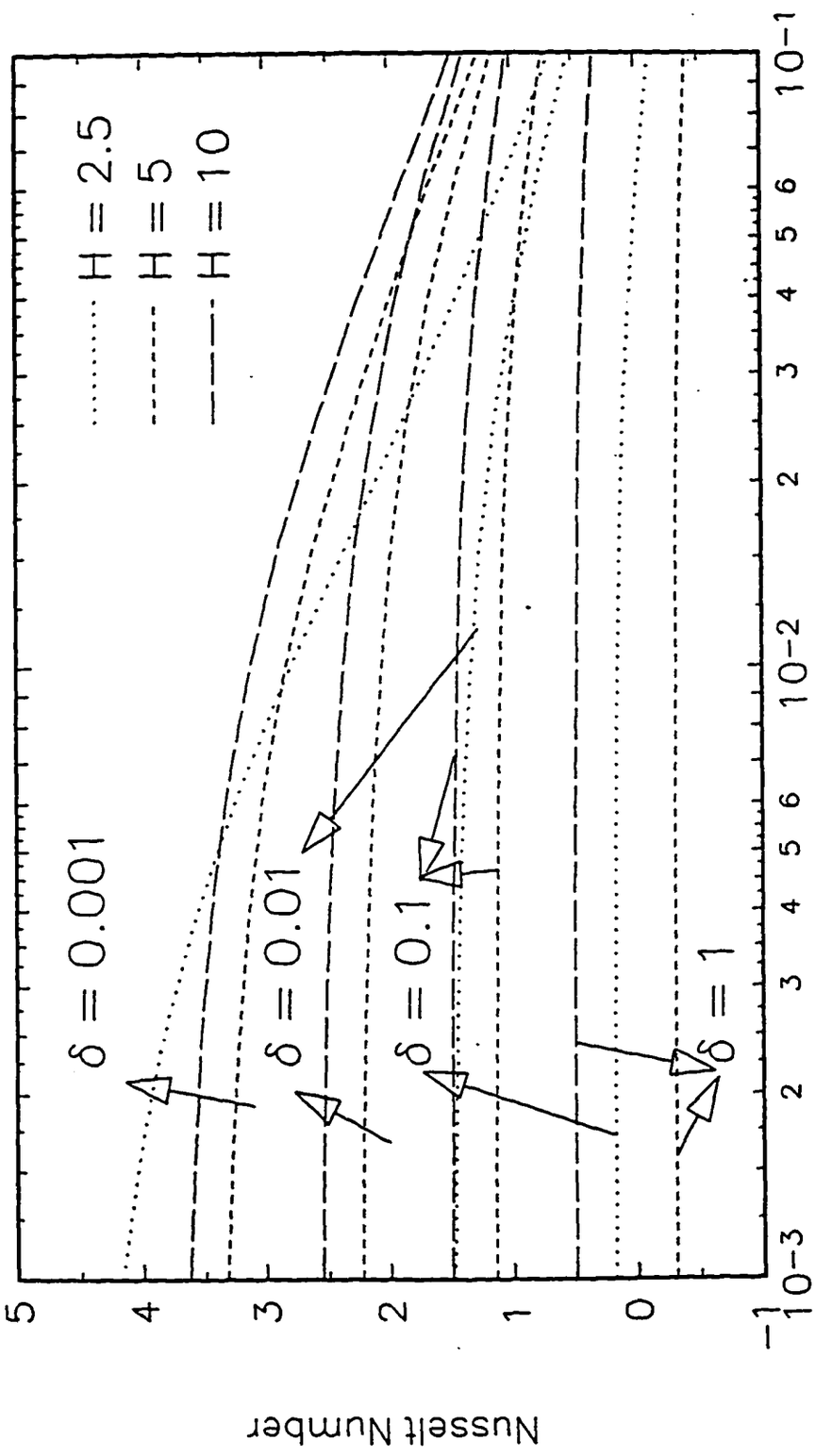

Figure III.2(c)
$T_r=-1$, $T_s=1$, $h/H=1$

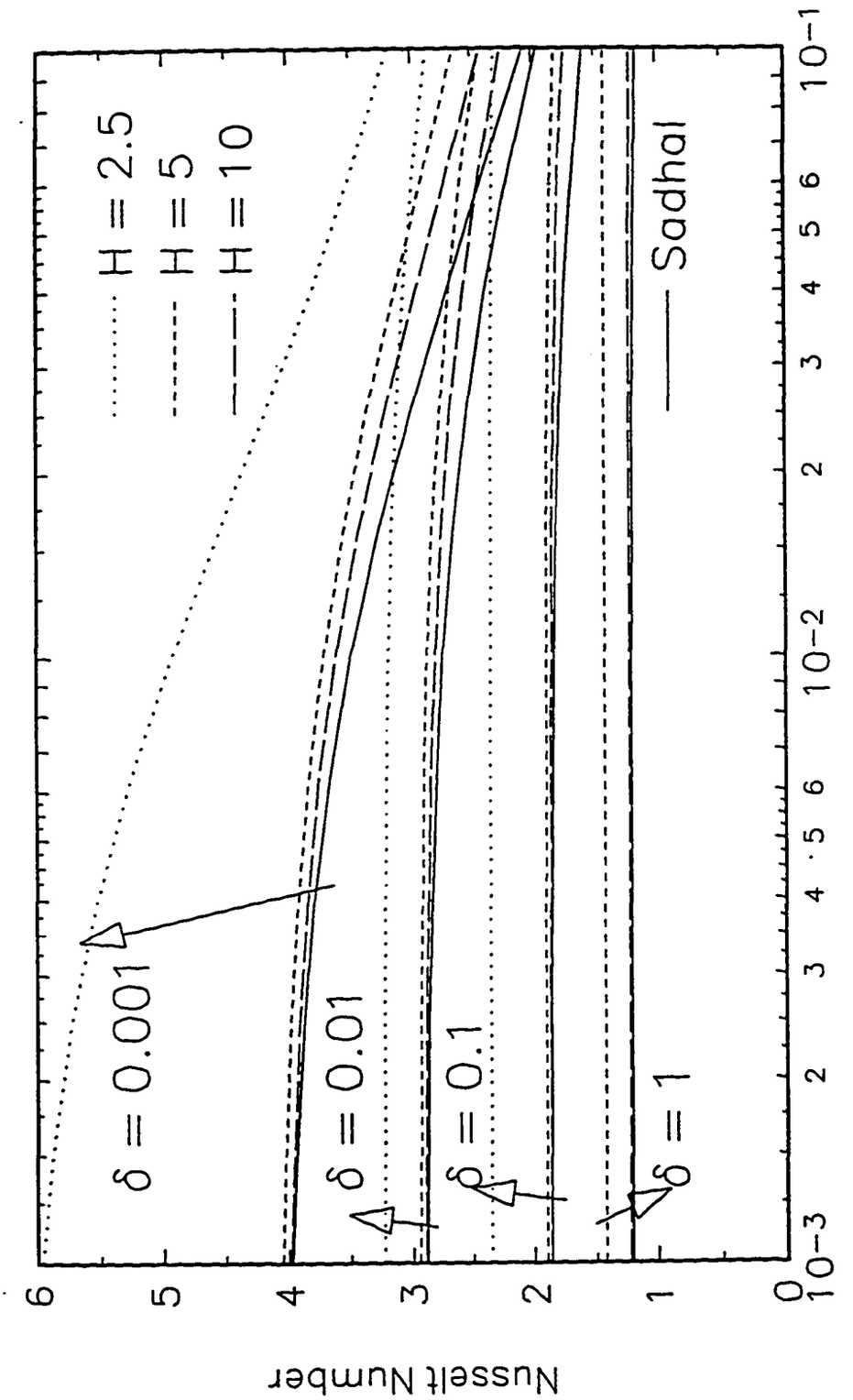

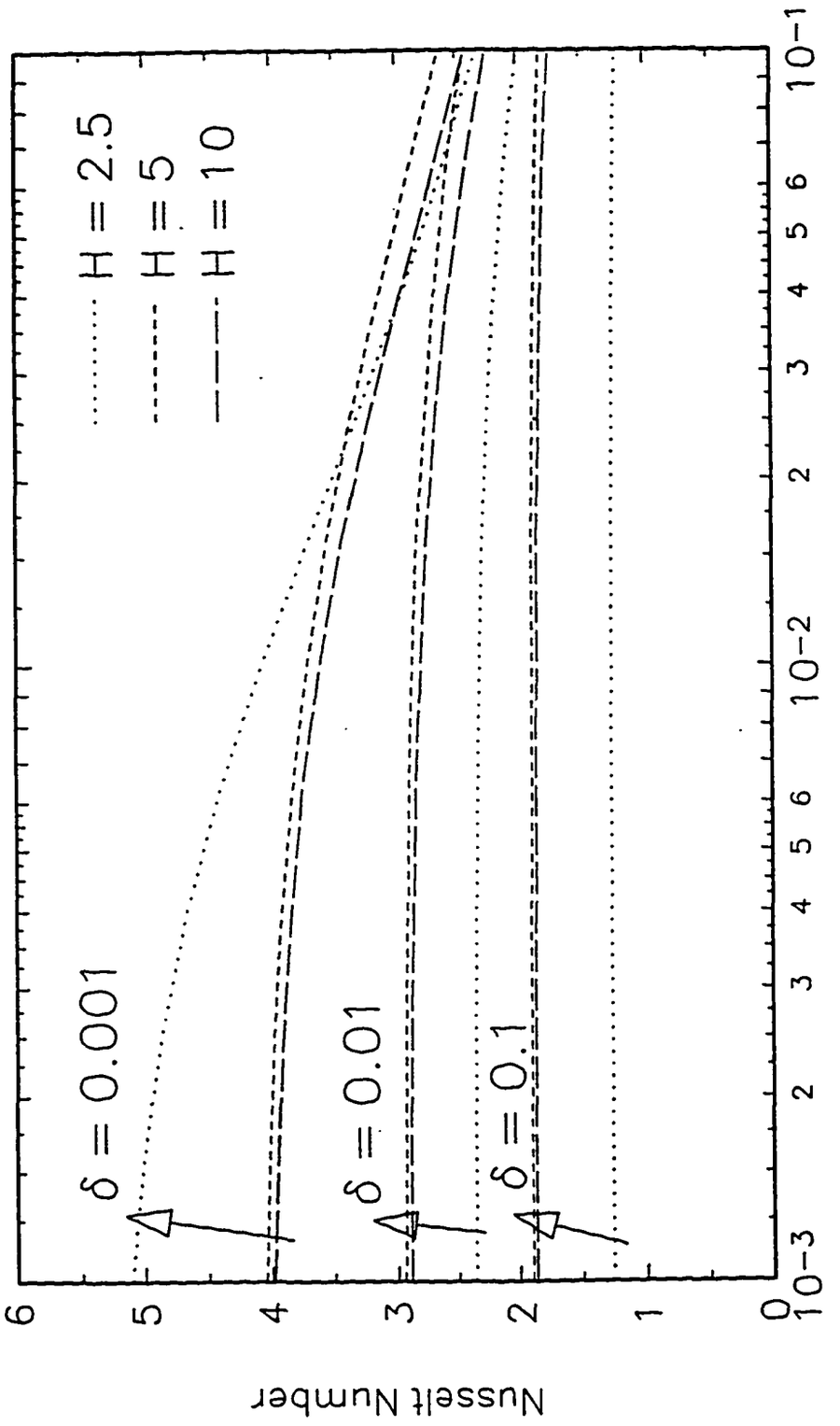

Figure. III.3(b)
$T_f=0$, $T_s=1$, $h/H=0.1$

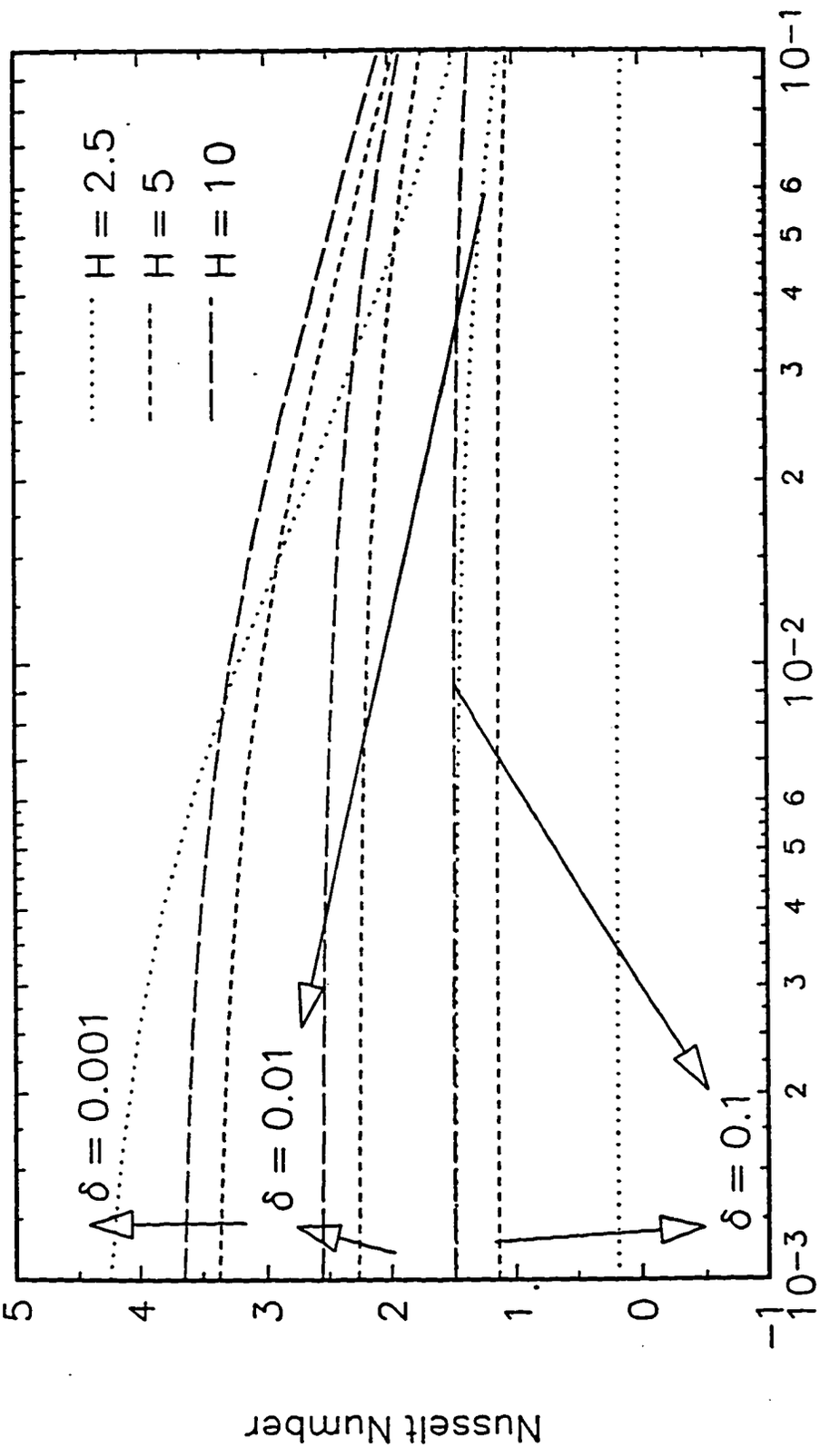

Figure III.3(c)
$T_f=-1$, $T_s=1$, $h/H=0.1$

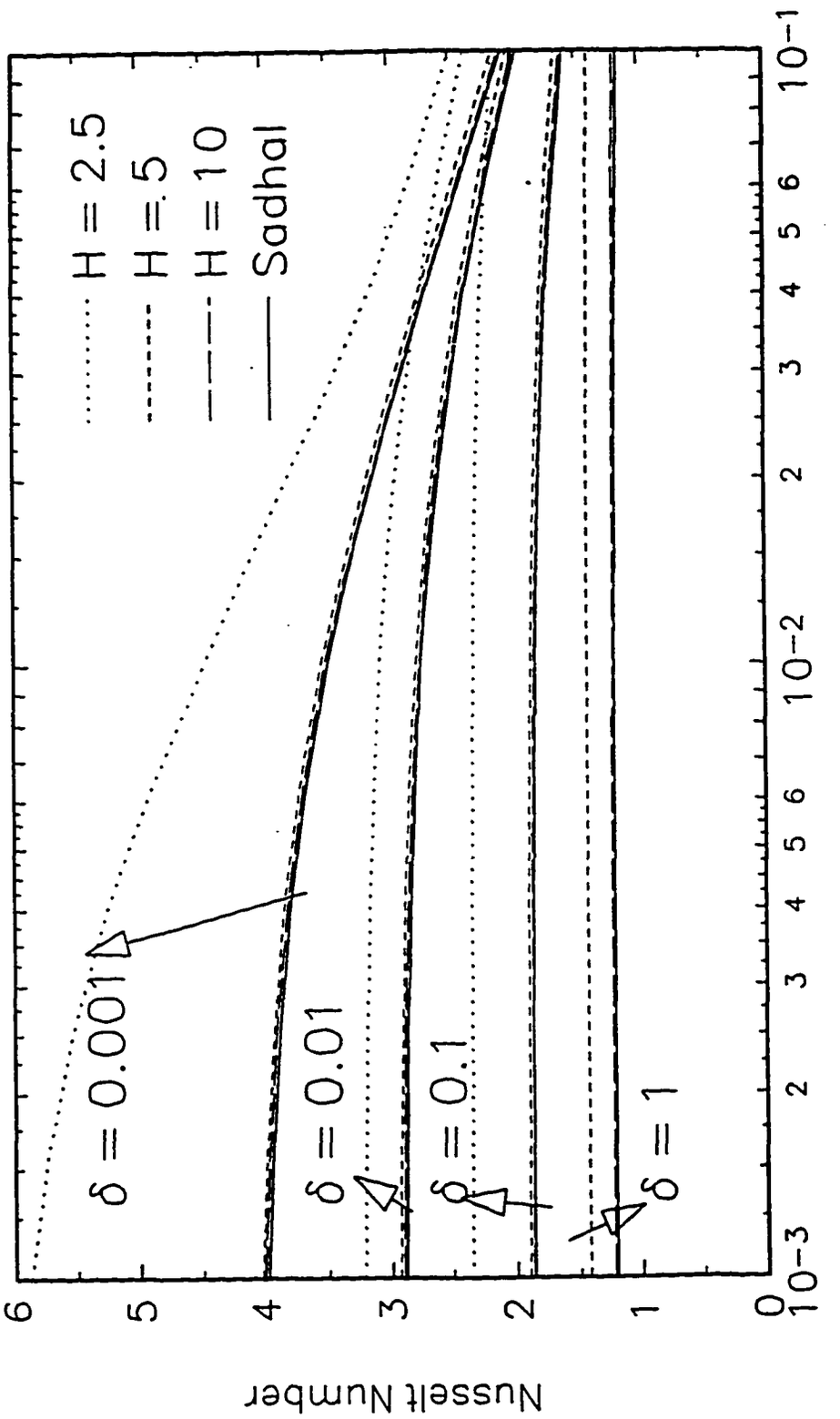

Figure III.4(a)
$T_f=1$, $T_s=1$, $h/H=10$

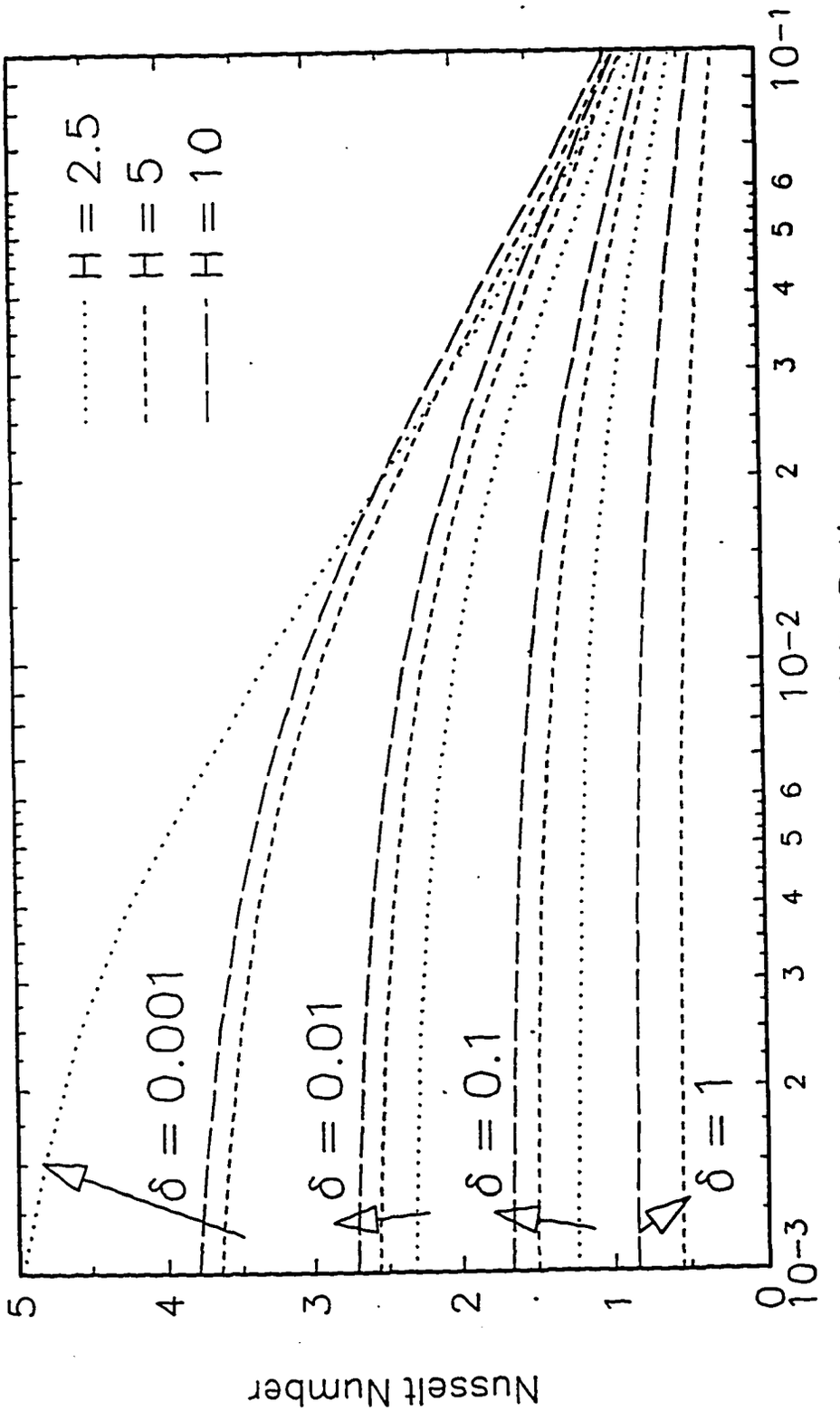

Figure III.4(b)
$T_f=0$, $T_s=1$, $h/H=10$

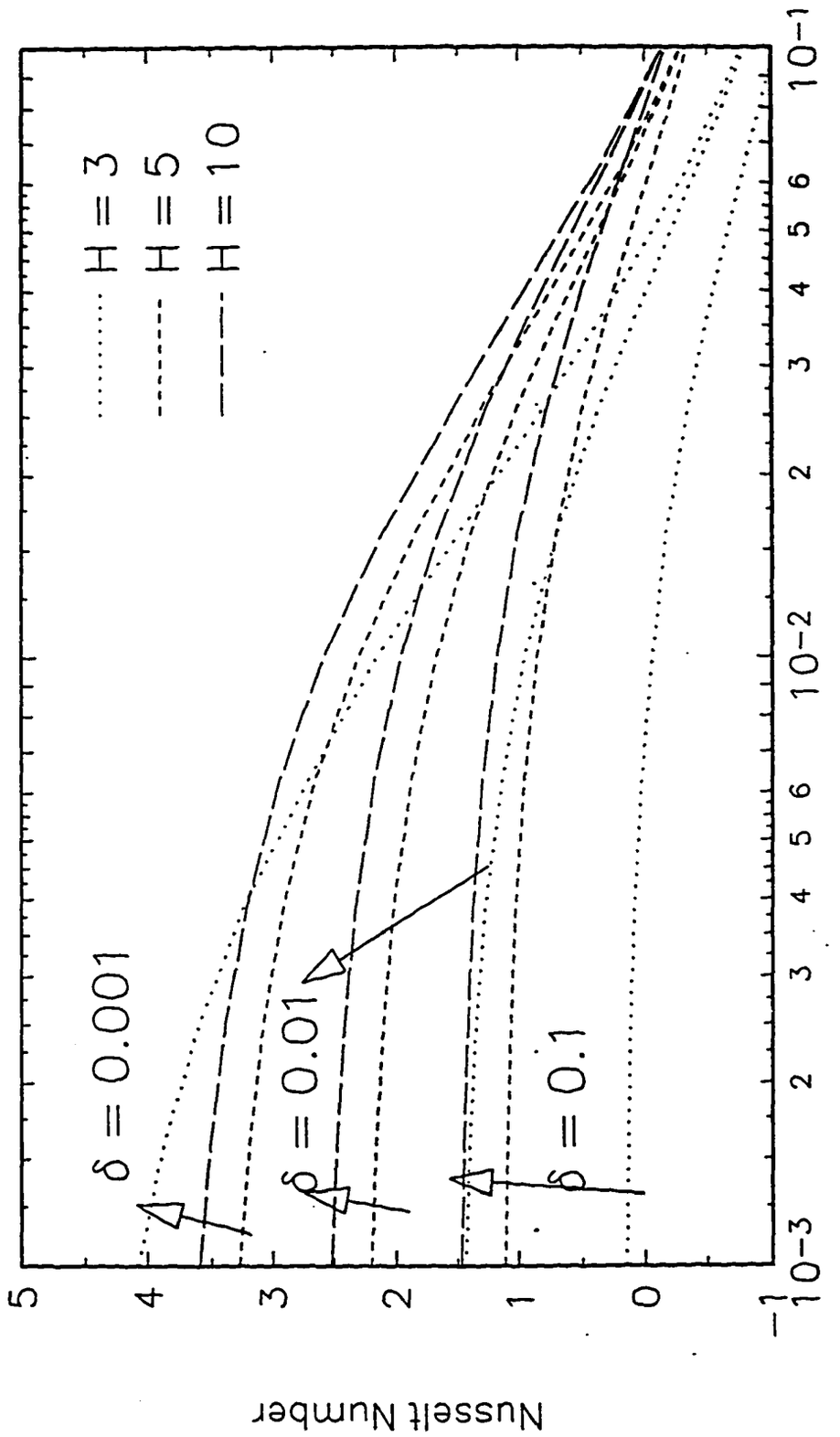

Figure III.4(c)
$T_f=-1$, $T_s=1$, $h/H=10$

Chapter IV

HEAT TRANSFER TO A SPHERICAL BUBBLE SUSPENDED IN LIQUID-SOLID COMPOSITE CELL OF FINITE DIMENSION BOTH NORMAL AND PARALLEL TO THE LIQUID-SOLID INTERFACE

IV.1 A vapor Bubble Suspended near a Solid Heating Wall.

IV.1.1 Formulation

The extension of the problems of a single vapor bubble near a heating wall to the case of many bubbles near a heating plate is clearly of great importance. Since conductive transfer between the solid wall and an adjacent bubble can greatly enhance heat transfer, the presence of many bubbles may increase it even more dramatically. A simplified model of a single bubble bounded laterally by an insulated, axisymmetric cylindrical surface of radius R_c (scaled by the bubble radius a') can describe a uniform spatial distribution of bubbles near the solid plate. The purpose of this calculation is

1) To reveal the effect of bubble density on the heat transfer enhancement;
2) To explore the proposed interactions between adjacent bubbles,
3) To reveal the influence of the system parameters such as the liquid and solid thicknesses, the distance between the bubble and the solid-liquid interface, the liquid-to-solid conductivity ratio and the domain width in domains of finite size parallel to the solid-liquid interface; and
4) to establish a test platform to verify the validity of further improved models.

This modified problem consists of a bubble suspended axisymmetrically in a liquid layer of thickness H above a solid cylinder of thickness h, both of radius R_c. Since the governing equations $\nabla^2 T_{\pm} = 0$ and boundary conditions (II.1,2,3) are

valid here as well and only require the additional insulating condition (II.5) at $R = R_c$, one can utilize the boundary integral technique (Bakr, 1986; Pozrikidis, 1993) to solve this problem. The boundary integral technique facilitates the numerical solution of linear problems such as Laplace equations in domains for which the Green's functions are known. It relies on Green's second identity which gives an integral relationship between any two solutions of the differential equation and some or all of the boundary conditions in question. By choosing the Green's function as one of these two solutions the volume integral reduces simply to the value of the dependent variable at the field point and the reciprocal theorem equates it to an integral over the boundary surface. Separate equations provide expressions for the dependent variable when the field point is in the interior (subscript p) or on the boundary (subscript q) of the domain of calculation. The reduction in dimensionality, from three to two, in general, or from two to one in axisymmetric problems, reduces computation times so dramatically as to make the method attractive.

For our problem the liquid boundary consists of the cylindrical surface at $R = R_c$ for $z > -d$, the solid-liquid interface $Z = -d$, the liquid free surface $Z = H - d$ and the bubble surface $R = 1$. The solid's surface consists of the cylindrical surface $R = R_c$ for $Z < -d$, the solid-liquid interface $Z = -d$ and the solid surface at $Z = -(d + h)$. Let

$$m := \frac{2\sqrt{R_p R_q}}{\sqrt{[(R_p + R_q)^2 + (Z_p - Z_q)^2]}} \qquad \text{(IV.1)}$$

and $E(m)$ and $K(m)$ be the complete elliptic integrals of first and second kinds, respectively, defined as

$$E(m) = \int_0^{\frac{\pi}{2}} \sqrt{1 - m^2 \sin^2 \alpha}\, d\alpha \qquad \text{(IV.2)}$$

$$K(m)=\int_0^{\frac{\pi}{2}}\frac{d\alpha}{\sqrt{1-m^2\sin^2\alpha}}. \qquad \text{(IV.3)}$$

Let the unit normal $\vec{n}$ to the boundary surface have components $\vec{n}=n_R\vec{e}_R+n_Z\vec{e}_Z$. Also, let Φ be the appropriate axisymmetric Greens function,

$$\Phi(R_q,Z_q,R_p,Z_p)=\frac{1}{2\pi}\int_0^{2\pi}\Phi(\bar{r}_q,\bar{z}_q)d\theta_q=\frac{mK(m)}{4\pi^2\sqrt{R_pR_q}} \qquad \text{(IV.4)}$$

whose gradient is

$$\begin{aligned}\nabla_q\Phi(R_q,Z_q,R_p,Z_p)=&\\ &\frac{m}{8\pi^2R_q\sqrt{R_pR_q}}\left[E(m)\frac{R_p^2-R_q^2+(Z_p-Z_p)^2}{(R_p-R_p)^2+(Z_p-Z_p)^2}-K(m)\right]n_{R_q}\\ &+\frac{m}{4\pi^2\sqrt{R_pR_q}}E(m)\frac{Z_p-Z_p}{(R_p-R_p)^2+(Z_p-Z_p)^2}n_{Z_q}\end{aligned} \qquad \text{(IV.5)}$$

The integral representation of the axisymmetric temperature distribution $T(R_p,Z_p)$, in the domain bounded by a surface Γ_q is:

$$\begin{aligned}T(R_p,Z_p)+2\pi\int_{\Gamma_q}T(R_q,Z_q)\nabla_q\Phi(R_q,Z_q,R_p,Z_p)R_q d\Gamma_q&\\ =2\pi\int_{\Gamma_q}\Phi(R_q,Z_q,R_p,Z_p)\nabla_q T(R_q,Z_q)R_q d\Gamma_q&\end{aligned} \qquad \text{(IV.6)}$$

The required boundary integral equation, follows by letting the field point approach the boundary. Some manipulations give

$$\begin{aligned}C(P)T(R_p,Z_p)+2\pi\int_{\Gamma_q}T(R_q,Z_q)\nabla_q\Phi(R_q,Z_q,R_p,Z_p)R_q d\Gamma_q&\\ =2\pi\int_{\Gamma_q}\Phi(R_q,Z_q,R_p,Z_p)\nabla_q T(R_q,Z_q)R_q d\Gamma_q,&\end{aligned} \qquad \text{(IV.7)}$$

where C(P) is further determined by the fact that, when the temperature is uniform on the boundary, the net heat flux there should be zero.

IV.1.2 Results

These boundary integral calculations have a new parameter, the cell size R_c, not available in the previous sections and we present curves that show its effect. Naturally, in order to verify the calculation methods, one must check, as Figure IV.1 and Figure IV.2 do, that the boundary integral results agree with the boundary collocation curves for large cell size R_c. Figure IV.1 shows that when R_c is 10, the collocation results approach Sadhal's solution when the thickness H of the liquid layer increases for all positive δ (negative δ corresponds to the attached bubble which we address in the next section), while the boundary integral results and the collocation's closely match each other. In Figure IV.2, the boundary integral results clearly approach those of the collocation technique's as R_c increases. (The H = 4 curve in Figure IV.1 and the collocation curves in Figure IV.2 rise for large δ because at $T_f = 1$ the bubble begins to derive heat from the free liquid surface, which is very close to the bubble for large δ and small H).

In Figure IV.2, the $R_c = 1.2$ curve is the only one for which the gap between the bubble and R_c is small compared with the bubble's radius, and there is a qualitative shift downward from the $R_c = 1.5$ curve. Basically, with such tight insulating boundaries, the bubble can only draw heat from the metal surface directly below (and the liquid free surface above, when $T_f = 1$) it, and not from the parts of these surfaces that are a bit further from the bubble - which are available for large R_c. Put another way, there is no region of the solid-liquid interface far enough from the bubble to achieve a temperature close to one, which would lead to a large heat flux from there towards the bubble from neighboring parts of the solid-liquid interface. Figures IV.3 and Figures IV.4 also exhibit the effects of finite R_c, i.e., of bubble-bubble interactions. Since the unit cell is now finite, it is meaningful to calculate the heat transfer enhancement due to the bubble's existence, i.e, the total heat transferred Q across the solid-liquid interface in the

presence of the bubble relative to that Q in a bubble free system, and the fraction $\sigma_{vs} = Q_v/Q_s$ of the heat crossing the solid-liquid interface that the bubble absorbs by vaporizing liquid at its periphery. Note that since Q_v in equation (III.11) represents the total rate at which the bubble absorbs heat, the increase in the bubble heat absorption is directly proportional to the increase in the Nusselt number. Figure IV.3, a plot of $\sigma_{s\ell} = Q/Q$ as a function of the fraction $\omega := (a/R_c)^2$ (where a is the radius of the bubble, R_c is the radius of the cell) of the solid-liquid interface covered by the projected area of the bubble, shows that the enhancement can be enormous (~100) as the bubble becomes large ($\omega \to 1$) and very close ($\delta \to 0$) to the solid surface. This is reasonable because forcing a zero temperature interface very close to solid-liquid interface over much of the cell causes a huge thermal gradient and concomitant heat transfer over the bubble-solid gap. Indeed, Figure IV.4 shows that when the bubble area is more than 0.1 of the cell's, almost all of the heat crossing the solid-liquid interface ends up in the bubble for a thick liquid layer. For a thin layer the same trend holds, but the corresponding area fraction is higher. These effects disappear as the bubble's projected area becomes a smaller fraction of the cell's area and as the bubble moves away from the wall, i.e., $\delta\uparrow$. For the same reason as before, a thinner solid layer at fixed κ ($h\downarrow$) has a effect similar to decreasing κ, thereby bringing the solid-liquid interface closer to T_s and increase the heat transfer. Although the qualitative behavior shown may not be surprising, it is important to emphasize the quantitative impact of the bubble density on the heat transfer rate. The heat transfer rate can be enhanced by up to two orders of magnitude (100 times), when the bubble density is high, the gap width is small, and the solid plate thickness is much smaller than that of the liquid layer. This order of the increasing in the heating rate is comparable to the increase observed in nucleate boiling. It further suggests that conduction might be the primary mode of heat transfer in nucleate boiling.

Finally, in nucleate boiling the presence of a bubble can inhibit bubble nucleation in an adjacent nucleation site. Eddington and Kenning (1978) show that there are many more cavities on a solid surface which satisfy the activation condition than nucleate boiling actually activates. They attributed their failure to activate to thermal interference from already active sites. The present model, despite its simplicity, appears to confirm this conclusion. For a cell radius R_c of 3 or less, the bubble absorbs about 85% of the heat crossing the solid wall thereby leaving too little to activate an adjacent nucleation site. Note that plots in Figure IV.5 and Figure IV.6 of the isotherms far from the bubble for $R_c = 5$, and $R_c = 2.5$ show large lateral heat transfer towards the bubble, leaving little to activate a new site there. The bubble also significantly lowers the solid-liquid interfacial temperature profile in its vicinity which in turn prevents the otherwise promising vapor embryos from forming.

IV.2. Attached Bubble

IV.2.1 Formulation

Due to the facts that the bubble heat transfer is dramatically higher the closer the bubble is to the wall and that bubbles begin on the wall before the detaching, it is natural to examine the case of a bubble attached to the wall and to expect its effect on the overall heat transfer to be profound. .We anticipate that the solid properties will impact the rate of the heat transfer more strongly when the bubble is attached to the solid wall. This Section considers a vapor bubble whose shape is a segment of a sphere that is attached to a solid-liquid interface and forms an insulating dry spot there. The bubble lies in a liquid layer of finite depth in an axisymmetric composite cell of finite radius R_c, as before. The geometric and physical settings are the same as in the previous section except that the bubble is now attached to the solid-liquid interface. Thus the insulating condition (II.4) at

$Z = -d$, $0 \leq R \leq \sin\varphi$ is also in force there. The contact angle φ is measured in the liquid between the solid-liquid interface and the liquid-vapor interface.

Experiments find that the heat transfer increases drastically with the incipience of the pool boiling. Explanations range from the convective heat transfer, which one also observes during the pre-pool boiling period, to the interactions between adjacent bubbles. According to the latter, bubble frequency plays an important role in the heat sweeping. Less frequent bubble emission allows a neighboring site to restore its heat capacity and to become active, while frequent emissions from one site inhibit neighboring sites. It is probably the bubble frequency effect that has made it difficult to observe inhibition activities, despite the existence of plausible statistical results. Thus this study examines the effect of the system parameters, which now include φ as a measure of its dynamic position not only on the overall heat transfer, but more importantly, on the bubble's influences on its neighborhood. We shall again look at how bubble density affects the heat enhancement $\sigma_{s\ell}$ in the presence of a distribution of bubbles relative to the bubble-free case, and the fraction σ_{vs} of the heat crossing the solid-liquid interface that ends up in the bubble. As in the last section, the insulating cell boundary at $R = R_c$ models a uniform distribution of simultaneously growing bubbles. Although there is only one bubble in this periodic configuration, the latter measure σ_{vs} indicate how strongly the existence of the bubble changes the local temperature and heat flux distributions; this knowledge should lend insight into how an attached or detached bubble could activate or deactivate an adjacent site (Chekanov 1977 and Calka and Judd 1985).

Even though, we analyze the problem only in the limited regime imposed by the ordering of the time scales in chapter 1, ignoring the problems of the bubble non-axisymmetry, transient convection and turbulence, we show that conductive heat transfer alone to a bubble on or close to a solid wall can be significant enough

to qualitatively account for many of the observed phenomena, including bubble-bubble interactions.

Before turning to the results we briefly discuss a technical difficulty that arises for the first time in the attached bubble case. We leave the details to the appendix. Due to the existence of a three-phase contact-line, both the geometric and physical boundary conditions become singular there. That is, the insulating boundary conditions of the dry spot, the temperature and flux continuity conditions of the liquid-solid interface, and the zero temperature condition of the bubble surface all overlap there. This contact line region will turn out to be critical in this study. First, the most banal effect is that the singular temperature and the flux profiles near the contact line should cause the numerical solutions to behave very poorly in that region. On the other hand, since the contact line is likely the site of the strongest heat sink capacity of the bubble, one cannot simply paper it over. We treat this region with special care to ensure the accuracy of the numerical solution. To avoid singularities at the contact line, we develop both a special meshing technique and an asymptotic analytic solution. The technique assumes that as long as R_c is not too close to one, the form of the temperature field in the region immediately adjacent to the contact region is insensitive to far away conditions, such as the temperatures at $Z = H - d$ and $Z = -(h - d)$. Thus Sadhal's (1989) analytical solution should, in an asymptotic form, apply there. The asymptotic temperature distributions around the contact line then are:

$$T_+ = A^*\sqrt{2\cosh\xi - 2\cos\eta}\,e^{-\xi/2}e^{-\xi\beta}\,\sin\beta(\varphi-\eta)\,\cos\pi\beta \qquad \text{(IV.8)}$$

$$T_- = A^*\sqrt{2\cosh\xi - 2\cos\eta}\,e^{-\xi/2}e^{-\xi\beta}\,\cos\beta(\eta+\pi)\,\sin\varphi\beta\,. \qquad \text{(IV.9)}$$

where $\eta = \arctan\left(\dfrac{2c(Z+d)}{(Z+d)^2+R^2-c^2}\right)$ and $\xi = \tanh^{-1}\left(\dfrac{2cR}{(Z+d)^2+c^2+R^2}\right)$ are the toroidal coordinates, and A is an arbitrary constant that an overall heat balance fixes.

One applies this asymptotic solution on a circular ring that intersects the vapor-liquid, liquid-solid and solid-vapor interfaces at right angles very close to the contact line angles (see Figure IV.15a). One then excludes the region enclosed by this ring, which includes small parts of the solid-vapor and liquid-vapor interfaces, from the domain of the boundary integral calculations and adjoins the ring's boundary to Γ. The asymptotic solution prescribes the normal flux on this ring portion of the boundary. For R_c close to one (very little wetted area) we use a different limiting case described in the appendix. Within the boundary integral domain, the technique generates a dense mesh on the ring near the contact line to provide sufficient node points to discretize the temperature and heat flux fields in the vicinity of the singularities. The node points become sparsely distributed wherever accuracy requirements permit a reduction in the bandwidth.

IV.2.2 Results

When the bubble is attached at small contact angles, the dry spot's radius c' may be smaller than the radius a' of the bubble's projection onto the solid-liquid interface. Since for large bubble/cell ratios, the latter is more pertinent, we modify the definition $\omega := (\bar{a}/R_c)^2$ to account for this, where

$$\bar{a} = \begin{cases} c' & \text{when } \varphi \geq 90° \\ a' & \text{when } \varphi \leq 90° \end{cases}.$$

When the bubble detaches, this definition agrees with the previous one.

Let us begin by examining the isotherms for various liquid free surface temperatures. Figures IV.7 - 9 show the temperature distributions for a cell of $H = h = R_c = 5$, $\kappa = 0.1$ and a contact angle $\varphi = 8°$ for temperatures $T_f = 1, 0, -1$, together with the magnifications of the contact line regions. The temperature distribution is symmetric about the cell axis and periodic at the edge of the cell.

The highly concentrated isothermal lines in the contact line region show an extremely high heat flux, indicating that the major evaporation takes place there.

Figure IV.8 shows that the solid-liquid interfacial temperature is lower at the edge of the cell when $T_f = 0$, and there is a substantial amount of heat transfer towards the liquid free surface in contrast to Figure IV.7, where it was a heat source. Figure IV.9 shows that a condensation region can even exist on the top of the bubble when $T_f = -1$. We omit most of the isothermal lines in the solid for $T_f = -1$ since their shapes are almost identical to the other cases, and differ only in their magnitudes. The contact line regions of the three cases are nearly the same due to the Sadhal limit involved, although the magnitudes of the local gradients decrease as the liquid free surface goes from being a heat source ($T_f = 1$) to a heat sink ($T_f = -1$).

1) *The Influence of Bubble attachment on Heat Transfer*: Figure IV.10 depicts the effect of bubble position δ on the heat enhancement σ_{st} for zero liquid free surface temperature Tf. In Figure IV.10, $R_c = H = h = 5$, and $\delta = (d-1)/2$. Recall that d is positive when the bubble is detached or when $\varphi < 90°$ and negative for $\varphi > 90°$. Thus δ positive, zero and negative correspond to detached, tangential and attached bubbles, respectively.

The most startling feature of figure IV.10 is the enormous increase in the total heat transferred that occurs as soon as the bubble attaches to the solid surface. For $\kappa = 0.001$, this can easily be an order of magnitude. The reason for this is that as long as the bubble does not touch the solid, the solid's high conductivity relative to that of the liquid serves only to bring the solid-liquid interface to a temperature essentially equal to that of its far solid face (Figures IV.5, $R_c = 5$). From there the temperature in the liquid has to drop to the saturation temperature over the gap between the bubble and the solid surface; the product of the low liquid thermal conductivity times this temperature gradient,

which balances the product of the larger κ_s and the solid's thermal gradient, dictates the heat transfer. However, once the bubble touches the solid, along the contact line, the *solid's* temperature must be equal to the saturation temperature there (compare Figures IV.5 with Figures IV.7 - Figures IV.9). Thus there must be steep gradient in the solid itself normal to the solid-liquid interface in order to accomplish this. Its coupling to the large κ_s leads to huge heat transfer enhancement. This accounts for the enhancement becoming very sensitive to κ as soon as the bubble attaches to the solid-liquid interface, and for the inverse thickness of the solid layer only playing a role for large κ (poorly conducting solid) at $\delta < 0$. Since the dry spot is insulating, its temperature can exceed T_v and approach the solid far surface temperature but the result is then radial transfer parallel to the solid surface towards the contact line.

Moreover, the more conducting the solid with an attached bubble, the steeper lateral temperature gradients along the solid-liquid interface. It is worth noticing that the enhancement goes through a maximum for fixed κ and ω as δ decreases. This is simply due to the fact that for a bubble of fixed radius, a decrease in δ from zero first increase the size of the dry spot and thus the length of the contact line, with ω unchanged, but then, as $\delta < 1/2$, both decrease together.

2) *The Influence of Bubble Density on the Heat Transfer*. Figure IV.11 shows the major influence of bubble crowding on heat transfer enhancement. The solid and liquid layer thicknesses are $H = h = 5$, and $T_f = 0$ for both $\kappa = 0.01$ and $\kappa = 0.001$ and three different contact angles $\varphi = 30°$, $90°$, $150°$ characterize the bubble positions. Here one sees that as the bubble takes more of the cell's area, i.e., bubble density increases the heat transfer enhancement grows, up to two orders of magnitude for $\kappa = 0.001$. The reason for this further enhancement is that when the bubble is only a small fraction of the cell, there is a substantial region of the cell far from the contact line's influence, where the solid-liquid interface can maintain a temperature close to that of its far surface. However, as the bubble

begins to fill a significant portion of the cell, i.e., as the bubble density rises, the regions that can maintain high solid-liquid interfacial temperature shrink and disappear and a large axial gradient, with concomitantly large heat transfer, forms more or less uniformly across the solid. This phenomenon can explain the sudden burst in the heat transfer rate associated with the incipience of nucleate pool boiling. The contact angle $30° < \varphi < 150°$ has only a minor effect since it changes the dry spot area by less than a factor of two. As the bubble fills up the cell ($\omega \rightarrow 1$), it is no longer clear that Sadhal's limit is reasonable and another limiting scaling applies (See the appendix for details). Finally, note that all curves in Figure IV.11 converge to unity when the ω approaches zero, i.e., for large cells or tiny bubbles, the overall enhanced heat flow in the whole cell induced by the existence of the bubble becomes insignificant.

3) *An active nucleate site inhibits neighboring sites:*. Figure IV.11 examines the fraction σ_{vs} of heat derived from the solid that goes towards liquid vaporization. For various bubble positions and ratios of conductivities, 95% of the total heat that passes through the solid-liquid interface finds its way to the liquid-vapor interface when the radius of the cell is smaller than 2.3, regardless of δ or κ. When the radius of the cell is about 3 ($\omega \approx 0.11$), more than 80% of the heat passing through the solid-liquid interface enters the bubble, with only weak bubble position dependence. Obviously, the bubble acts as a major heat sink that monopolizes a considerable amount of the heat in its vicinity. As it grows, and occupies more of the cell, any heat transferring toward the liquid free surface must pass around the bubble. When the bubble density is high, the radial gradient in the directions of the bubbles are large, thereby forcing most of the heat towards the bubbles and not allowing it to build vapor to bypass them. This may be the cause of the observed inhibition activity in Eddington and Kenning (1978). On the other hand, when the distance between bubbles is large, the heat sink capacity of a single bubble is insufficient to disturb the heat transfer (compare with isotherms for

$R_c = 5$ cases) normal to the solid-liquid interface far from the bubble. So, the bubble emission *frequency* determines the overall heat transfer rate. Less frequent bubble formation at a site followed by a detachment of a small bubble can allow neighboring sites to activate quickly; when they release their bubbles, the initial site can reactivate. In contrast, frequent bubble formation at one site and the growth of a large bubble there do not allow neighboring sites to activate and thus can inhibit the overall heat transfer. Of course a better understanding of these processes requires consideration of the effects that lead to bubble snap off, including those that determine snap-off time and volume.

Appendix A

ASYMPTOTIC TECHNIQUES FOR THE CONTACT REGION AND THE MESH GENERATING METHOD

As noted in the text, the three-phase contact line appears to be singular and requires special treatment. Our approach is to exclude it from the domain of the boundary integral problem and to develop an exact analytic solution for its vicinity. We then use this analytical solution to prescribe the temperature flux to within an arbitrary constant along the portion of the boundary integral domain's boundary created to delete the contact region. We shall call this region the "asymptotic region."

To obtain the asymptotic solution in question we require that the form of the temperature profile and the large gradients very close to the contact line, i.e., within a distance much less that the bubble radius a', must be insensitive to conditions far, i.e., at distance much greater than a' from the contact line. This insensitivity applies to the functional form of the temperature profiles, but not to their magnitudes, since their magnitudes impact the overall heat transfer, which is a global quantity. Thus we begin by reviewing the exact solution of Sadhal (1989) for a spherical vapor bubble attached to a solid-liquid interface and expand it for a small distance from the contact line. We then multiply the result by the scale factor, and determine its value by a requiring the boundary integral result to agree with the asymptotic result along the part of the phase boundaries close to the asymptotic region.

Sadhal's solution (1989) is in terms of toroidal coordinates (ξ, η, ψ) (see Figure IV.13), which one can write in terms of the usual cylindrical coordinates (R, Z, ψ) as

$$Z + d = \frac{c \sin \eta}{\cosh \xi - \cos \eta} \qquad R = \frac{c \sinh \xi}{\cosh \xi - \cos \eta} \qquad \text{(IV.10)}$$

$$\eta = \arctan\left(\frac{2c(Z+d)}{(Z+d)^2+R^2-c^2}\right) \qquad \xi = \tanh^{-1}\left(\frac{2cR}{(Z+d)^2+c^2+R^2}\right). \quad \text{(IV.11)}$$

Here, c is the radius of the contact line, or the dry spot. In this coordinate system, the solid-liquid interface is $\eta = 0$, $0 \le \xi \le \infty$; the liquid-vapor interface is $\eta = \varphi$, the contact angle of the bubble measured inside the liquid, and $0 \le \xi \le \infty$; and solid-vapor interface is $\eta = -\pi$, $0 \le \xi \le \infty$. Laplace's equation

$$\nabla^2 T = \frac{\partial}{\partial\eta}\left(\frac{\sinh\xi}{\cosh\xi-\cos\eta}\frac{\partial T}{\partial\eta}\right)+\frac{\partial}{\partial\xi}\left(\frac{\sinh\xi}{\cosh\xi-\cos\eta}\frac{\partial T}{\partial\xi}\right)=0 \qquad \text{(IV.12)}$$

governs the temperature distributions in both the solid and liquid.

The boundary conditions (II.1)-(II.4) in the toroidal coordinates are

$$T_+(\xi,\varphi) = T_v; \qquad \text{(IV.13)}$$

$$T_+(\xi,0) = T_-(\xi,0); \qquad \kappa\frac{\partial T_+(\xi,0)}{\partial\eta} = \frac{\partial T_-(\xi,0)}{\partial\eta}; \qquad \text{(IV.14)}$$

$$\frac{\partial T_-(\xi,-\pi)}{\partial\eta} = 0. \qquad \text{(IV.15)}$$

Note that the far fields of the liquid and solid $Z = \pm\infty$ are compressed into $\eta = \xi = 0$ where $T_\pm(\xi,\eta) \xrightarrow[\xi=\eta=0]{} T_\infty$. Thus, Sadhal assumes that the far field temperatures in both the liquid and the solid, each of which is necessarily infinite in extent, are both equal, and presumably satisfy $T_\infty > T_v$. Nevertheless, one can non-dimensionalize temperature via $\hat{T} := (T' - T'_\infty)/(T'_v - T'_\infty)$. This definition is different from the previous one defined in Chapter II, where $T_\pm := (T'_\pm - T'_v)/(T'_s - T'_v)$. The new definition is made to utilize equality (IV.20) below.

Since Laplace's equation is separable in toroidal coordinates, one can solve this problem by standard methods. The temperature distributions are

$$T_+ = \sqrt{2\cosh\xi - 2\cos\eta}\int_0^\infty \left(\phi_1(\tau)\cosh(\eta\tau) + \phi_2(\tau)\sinh(\eta\tau)\right)K_\tau(\cosh\xi)d\tau \qquad \text{(IV.16)}$$

$$T_- = \sqrt{2\cosh\xi - 2\cos\eta}\int_0^\infty \left(\phi_3(\tau)\cosh(\eta\tau) + \phi_4(\tau)\sinh(\eta\tau)\right)K_\tau(\cosh\xi)d\tau \qquad \text{(IV.17)}$$

where

$$K_\tau(\cosh\xi) := P_{-\frac{1}{2}+i\lambda}(\cosh\xi) = \frac{2}{\pi\tanh(\pi\tau)}\int_\xi^\infty \frac{\sin(\rho\tau)d\rho}{\sqrt{2\cosh\rho - 2\cosh\xi}} \qquad \text{(IV.18)}$$

is the Legendre function of complex degree and $\phi_1(\tau)$ - $\phi_4(\tau)$ are unknown functions to be determined by the boundary conditions. To solve for $\phi_1(\tau)$ - $\phi_4(\tau)$, one makes use of transforms:

$$\begin{cases} f(\xi) = \int_0^\infty g(\tau)K_\tau(\cosh\xi)d\tau \\ g(\tau) = \tau\tanh(\pi\tau)\int_0^\infty f(\xi)K_\tau(\cosh\xi)\sinh\xi d\xi \end{cases} \qquad 0 \le \xi \le \infty \qquad \text{(IV.19)}$$

and the integral identity

$$\sqrt{2\cosh\xi - 2\cos\eta}\int_0^\infty \frac{\cosh\tau(\eta-\pi)}{\cosh\tau\pi}K_\tau(\cosh\xi)d\tau = 1. \qquad \text{(IV.20)}$$

By transforming (IV.13)-(IV.15), with (IV.19) and using (IV.20), one finds the functions $\phi_1(\tau)$ - $\phi_4(\tau)$. The temperature distributions become

$$\hat{T}_+ = \sqrt{2\cosh\xi - 2\cos\eta}$$
$$\int_0^\infty \frac{\cosh\tau(\varphi-\pi)\cosh\eta\tau\,[\kappa+\tanh\pi\tau\tanh\eta\tau]K_{i\tau}(\cosh\xi)d\tau}{\cosh\tau\pi\cosh\varphi\tau\,[\kappa+\tanh\pi\tau\tanh\varphi\tau]} \qquad \text{(IV.21)}$$

$$\hat{T}_- = \kappa\sqrt{2\cosh\xi - 2\cos\eta}$$
$$\int_0^\infty \frac{\cosh\tau(\varphi-\pi)\ \cosh\tau(\pi+\eta)\,K_{i\tau}(\cosh\xi)d\tau}{\cosh^2\pi\tau\ \cosh\varphi\tau\,[\kappa+\tanh\pi\tau\tanh\varphi\tau]} \qquad \text{(IV.22)}$$

By substituting (IV.18) into (IV.21) and (IV.22), one has

$$\hat{T}_+ = \sqrt{2\cosh\xi - 2\cos\eta}\int_\xi^\infty \frac{\sin(\rho\tau)d\rho}{\sqrt{2\cosh\rho - 2\cosh\xi}}$$
$$\int_0^\infty \frac{2\cosh\tau(\varphi-\pi)\cosh\eta\tau\,[\kappa+\tanh\pi\tau\tanh\eta\tau]d\tau}{\pi\sinh\tau\pi\cosh\varphi\tau\,[\kappa+\tanh\pi\tau\tanh\varphi\tau]}, \qquad \text{(IV.23)}$$

$$\hat{T}_- = \kappa\sqrt{2\cosh\xi - 2\cos\eta}\int_\xi^\infty \frac{\sin(\rho\tau)d\rho}{\sqrt{2\cosh\rho - 2\cosh\xi}}$$
$$\int_0^\infty \frac{2\cosh\tau(\varphi-\pi)\ \cosh\tau(\pi+\eta)\,d\tau}{\pi\cosh\pi\tau\ \sinh\pi\tau\cosh\varphi\tau\,[\kappa+\tanh\pi\tau\tanh\varphi\tau]}. \qquad \text{(IV.24)}$$

Keeping in mind that $\sin\rho\tau = \tau\int_0^\rho \cos\mu\tau\,d\mu$, one can rewrite (IV.23) and (IV.24) as

$$\hat{T}_+ = \sqrt{2\cosh\xi - 2\cos\eta}\int_\xi^\infty \frac{\tau\int_0^\rho \cos\mu\tau\,d\mu d\rho}{\sqrt{2\cosh\rho - 2\cosh\xi}}$$
$$\int_0^\infty \frac{2\cosh\tau(\varphi-\pi)\cosh\eta\tau\,[\kappa+\tanh\pi\tau\tanh\eta\tau]d\tau}{\pi\sinh\tau\pi\cosh\varphi\tau\,[\kappa+\tanh\pi\tau\tanh\varphi\tau]}, \qquad \text{(IV.25)}$$

$$\hat{T}_- = \kappa\sqrt{2\cosh\xi - 2\cos\eta}\int_\xi^\infty \frac{\tau\int_0^\rho \cos\mu\tau\,d\mu d\rho}{\sqrt{2\cosh\rho - 2\cosh\xi}}$$
$$\int_0^\infty \frac{2\cosh\tau(\varphi-\pi)\ \cosh\tau(\pi+\eta)\,d\tau}{\pi\cosh\pi\tau\ \sinh\pi\tau\cosh\varphi\tau\,[\kappa+\tanh\pi\tau\tanh\varphi\tau]}, \qquad \text{(IV.26)}$$

which lead to

$$\hat{T}_+ = \frac{2}{\pi}\sqrt{2\cosh\xi - 2\cos\eta}\int_{\xi}^{\infty}\frac{d\rho}{\sqrt{2\cosh\rho - 2\cosh\xi}}\int_{0}^{\rho}d\mu \int_{0}^{\infty}\frac{\cosh(\varphi-\pi)\tau\,\tau\cos\mu\tau\,(\kappa\cosh\pi\tau\cosh\eta\tau + \sinh\pi\tau\sinh\eta\tau)d\tau}{\sinh\pi\tau\,(\kappa\cosh\varphi\tau\cosh\pi\tau + \sinh\pi\tau\sinh\varphi\tau)} \tag{IV.27}$$

$$\hat{T}_- = \frac{2\kappa}{\pi}\sqrt{2\cosh\xi - 2\cos\eta}\int_{\xi}^{\infty}\frac{d\rho}{\sqrt{2\cosh\rho - 2\cosh\xi}}\int_{0}^{\rho}d\mu \int_{0}^{\infty}\frac{\cosh(\varphi-\pi)\tau\,\tau\cos\mu\tau\cosh\tau(\eta+\pi)d\tau}{\sinh\pi\tau\,(\kappa\cosh\varphi\tau\cosh\pi\tau + \sinh\varphi\tau\sinh\pi\tau)} \tag{IV.28}$$

The integrands of the τ-integrals are both even functions. If one completes the contours of integration in (IV.27) and (IV.28) by appending the semicircle of radius R ($R \to \infty$) to enclose the upper half of the complex τ-plane, and keeps in mind that the integrand for small κ has a large contribution near $\tau = 0$, one can invoke the residue theorem to conclude that the value of the integral is equal to the sum of residues at the poles in the interior of the contour. The poles are simply the roots β of the equation

$$\kappa = \tan\pi\beta\ \tan\varphi\beta \tag{IV.29}$$

where κ, and φ are system parameters.

For metallic solids, the solid thermal conductivity is much larger than that of most non-metallic liquids, and therefore we have $\kappa << 1$. With this in mind, one can expand the integrands in (IV.27) and (IV.28) to leading order in the small parameter κ and integrate these leading orders in closed form.

For small κ and $\varphi = O(1)$, the leading pole of equation (IV.29) makes the most significant contribution to the integration (IV.27) and (IV.28), and it is the closest to the origin. This pole is approximately $\beta = \sqrt{\kappa/\varphi\pi}$, (see Sadhal 1989). Thus, the integrals become

$$\hat{T}_+ = \sqrt{2\cosh\xi - 2\cos\eta}\int_0^{\rho}\beta e^{-\beta\mu}d\mu\int_{\xi}^{\infty}\frac{d\rho}{\sqrt{2\cosh\rho - 2\cosh\xi}} \qquad \text{(IV.30)}$$
$$\frac{2\cos((\pi-\varphi)\beta)\sin\beta(\varphi-\eta)\cos(\pi\beta)}{(\varphi\sin(\pi\beta)\cos(\pi\beta)+\pi\sin(\varphi\beta)\cos(\varphi\beta))}$$

$$\hat{T}_- = 2\kappa\sqrt{2\cosh\xi - 2\cos\eta}\int_0^{\rho}\beta e^{-\beta\mu}d\mu\int_{\xi}^{\infty}\frac{d\rho}{\sqrt{2\cosh\rho - 2\cosh\xi}} \qquad \text{(IV.31)}$$
$$\frac{\cos(\varphi-\pi)\beta\ \cos\beta(\eta+\pi)\cos\varphi\beta}{(\phi\sin\pi\beta\cos\pi\beta+\pi\cos\varphi\beta\sin\varphi\beta)}$$

Note that for $Q_\nu(\cosh\xi)$ the Legendre function, the integral

$$\int_{\xi}^{\infty}\frac{(1-e^{-\beta\rho})d\rho}{\sqrt{2\cosh\rho-2\cosh\xi}} = Q_{-\frac{1}{2}}(\cosh\xi) - Q_{-\frac{1}{2}+\beta}(\cosh\xi) \qquad \text{(IV.32)}$$
$$= \pi e^{-\xi/2}(1-e^{-\xi\beta})$$

With Equation (IV.32) the temperature distribution finally reduces to that given by Sadhal:

$$\hat{T}_+ = A(\kappa,\varphi)B(\xi,\eta,\beta)\sin\beta(\varphi-\eta)\ \cos\pi\beta \qquad \text{(IV.33)}$$

$$\hat{T}_- = A(\kappa,\varphi)B(\xi,\eta,\beta)\cos\beta(\eta+\pi)\ \sin\varphi\beta, \qquad \text{(IV.34)}$$

where $A(\kappa,\varphi) = 2\pi\cos((\pi-\varphi)\beta)/(\varphi\sin(\pi\beta)\cos(\pi\beta)+\pi\sin(\varphi\beta)\cos(\varphi\beta))$ is a function of κ and φ, the only two physical and geometrical parameters of the system other than a' which has set the length scales, and $B(\xi,\eta,\beta) = \sqrt{2\cosh\xi-2\cos\eta}e^{-\xi/2}(1-e^{-\xi\beta})$. Returning to our original definition of a dimensionless temperature $T_\pm = (T'_\pm - T'_v)/(T'_s - T'_v)$, one writes $T_\pm = (1-\hat{T}_\pm)(T'_\infty - T'_v)/(T'_s - T'_v)$, or,

$$T_+ = \frac{\left[1 - A(\kappa,\varphi)B(\xi,\eta,\beta)\sin\beta(\varphi-\eta)\cos\pi\beta\right]\left(T'_\infty - T'_v\right)}{\left(T'_s - T'_v\right)}, \qquad \text{(IV.35)}$$

$$T_- = \frac{\left[1 - A(\kappa,\varphi)B(\xi,\eta,\beta)\cos\beta(\pi+\eta)\sin\varphi\beta\right]\left(T'_\infty - T'_v\right)}{\left(T'_s - T'_v\right)}. \qquad \text{(IV.36)}$$

This work focuses on the heat transfer to a vapor bubble in a cylindrical region perpendicular to the solid-liquid interface with the bubble at its center, that has finite solid and liquid layer thicknesses and has an insulating boundary conditions on its cylindrical surface. As noted, we employ Sadhal's solution which, in contrast, applies to a situation where both the solid and liquid are infinite in extent parallel to their mutual interface and semi-infinite perpendicular to it, to prescribe the form of the temperature field in the contact line region. Our conviction is that when multiple bubbles, i.e., the bubble and the cell's edges, are a distance apart that is not small compared with their radii, then the form of the asymptotic temperature distribution close to the contact line should be independent of the far field. The way we implement this is to retain the forms of equations (IV.35) and (IV.36) but to allow the multiplication constant $A(\kappa,\varphi)\left(T'_\infty - T'_v\right)/\left(T'_s - T'_v\right)$, which determines the magnitude of the heat flux, to be an adjustable parameter $A_\pm$ in each region and to permit, by adding the parameters $B_\pm$, the absolute temperature at the edge of the contact line region to be adjustable. In this way, $A_\pm$ and $B_\pm$ can depend on the particulars of the far field conditions, which determine the temperature on the dry spot and the global parameters such as the overall heat flux,. Thus, one can write

$$T_+ = A_+\sqrt{2\cosh\xi - 2\cos\eta}\,e^{-\xi/2}(e^{-\xi\beta} - 1)\sin\beta(\varphi-\eta)\ \cos\pi\beta + B_+, \text{(IV.37)}$$

$$T_- = A_-\sqrt{2\cosh\xi - 2\cos\eta}\,e^{-\xi/2}(e^{-\xi\beta} - 1)\cos\beta(\eta+\pi)\ \sin\varphi\beta + B_-. \text{(IV.38)}$$

Since (IV.37) and (IV.38) must vanish on the contact line, where temperature is zero, one has:

$$\lim_{\xi\to\infty} T_+ = -A_+ \sin\beta(\varphi-\eta)\ \cos\pi\beta + B_+ = 0, \tag{IV.39}$$

$$\lim_{\xi\to\infty} T_- = -A_- \cos\beta(\eta+\pi)\ \sin\varphi\beta + B_- = 0, \tag{IV.40}$$

which gives $B_\pm$ as

$$\begin{cases} B_+ = A_+ \sin\beta(\varphi-\eta)\ \cos\pi\beta \\ B_- = A_- \cos\beta(\eta+\pi)\ \sin\varphi\beta \end{cases}, \tag{IV.41}$$

and simply reduces (IV.37) and (IV.38) to

$$T_+ = A_+\sqrt{2\cosh\xi - 2\cos\eta}\,e^{-\xi/2}e^{-\xi\beta}\sin\beta(\varphi-\eta)\ \cos\pi\beta \tag{IV.42}$$

$$T_- = A_-\sqrt{2\cosh\xi - 2\cos\eta}\,e^{-\xi/2}e^{-\xi\beta}\cos\beta(\eta+\pi)\ \sin\varphi\beta. \tag{IV.43}$$

To prescribe the heat flux on the boundary of the asymptotic region requires the various partial derivatives of the temperature $T_\pm$ (IV.42) and (IV.43); they are:

$$\frac{\partial T_+}{\partial\eta} = \nabla T_+ \cdot \vec{\eta} = A_+ e^{-\xi/2}e^{-\xi\beta}\cos\beta\pi/\sqrt{2\cosh\xi - 2\cos\eta} \left(\sin\beta(\varphi-\eta)\ \sin\eta - 2(\cosh\xi - \cos\eta)\beta\cos\beta(\varphi-\eta)\right) \tag{IV.44}$$

$$\frac{\partial T_+}{\partial\xi} = \nabla T_+ \cdot \vec{\xi} = A_+ e^{-\xi/2}e^{-\xi\beta}\cos\pi\beta\sin\beta(\varphi-\eta)/\sqrt{2\cosh\xi - 2\cos\eta} \left(\sinh\xi - \cosh\xi + \cos\eta - 2\beta(\cosh\xi - \cos\eta)\right) \tag{IV.45}$$

$$\frac{\partial T_-}{\partial\eta} = \nabla T_- \cdot \vec{\eta} = A_- e^{-\xi/2}e^{-\xi\beta}\sin(\beta\varphi)/\sqrt{2\cosh\xi - 2\cos\eta} \left(\cos\beta(\eta+\pi)\ \sin\eta - \beta(2\cosh\xi - 2\cos\eta)\sin\beta(\eta+\pi)\right) \tag{IV.46}$$

$$\frac{\partial T_-}{\partial\xi} = \nabla T_- \cdot \vec{\xi} = A_- e^{-\xi/2}e^{-\xi\beta}\cos\beta(\eta+\pi)\ \sin\beta\varphi/\sqrt{2\cosh\xi - 2\cos\eta} \left(\sinh\xi - \cosh\xi + \cos\eta - 2\beta(\cosh\xi - \cos\eta)\right) \tag{IV.47}$$

The fluxes in the liquid and solid regions then become

$$\frac{\partial T_{\pm}}{\partial n} = \nabla T_{\pm} \cdot \vec{n} = \left(\frac{1}{H_{\xi}} \frac{\partial T_{\pm}}{\partial \xi} \vec{e}_{\xi} + \frac{1}{H_{\eta}} \frac{\partial T_{\pm}}{\partial \eta} \vec{e}_{\eta}\right) \cdot \vec{n}, \qquad \text{(IV.48)}$$

where $\vec{n}$ is the vector normal to the surface of interest, ∇ is the gradient, and $H_{\eta} = H_{\xi} = c/(\cosh\xi - \cos\eta)$ are the metric coefficients. By using the transformation

$$\begin{pmatrix} \vec{e}_{\xi} \\ \vec{e}_{\eta} \end{pmatrix} = \begin{pmatrix} (\vec{e}_R \cdot \vec{e}_{\xi}) & (\vec{e}_R \cdot \vec{e}_{\eta}) \\ (\vec{e}_Z \cdot \vec{e}_{\xi}) & (\vec{e}_Z \cdot \vec{e}_{\eta}) \end{pmatrix} \begin{pmatrix} \vec{e}_R \\ \vec{e}_Z \end{pmatrix} = \begin{pmatrix} \frac{1}{H_{\xi}} \frac{\partial R}{\partial \xi} & \frac{1}{H_{\xi}} \frac{\partial Z}{\partial \xi} \\ \frac{1}{H_{\eta}} \frac{\partial R}{\partial \eta} & \frac{1}{H_{\eta}} \frac{\partial Z}{\partial \eta} \end{pmatrix} \begin{pmatrix} \vec{e}_R \\ \vec{e}_Z \end{pmatrix}, \qquad \text{(IV.49)}$$

one can see that the metric coefficients are related to terms like $(\vec{e}_Z \cdot \vec{e}_{\eta})$, which is the directional cosine of the angle between unit vectors $\vec{e}_Z$ and $\vec{e}_{\eta}$. The fluxes in terms of (R, Z, ψ) coordinates follow as

$$\frac{\partial T_{\pm}}{\partial n} = \frac{1}{H_{\eta}^2} \left\{ \left(\frac{\partial T_{\pm}}{\partial \xi} \frac{\partial R}{\partial \xi} + \frac{\partial T_{\pm}}{\partial \eta} \frac{\partial R}{\partial \eta} \right) \vec{e}_R + \left(\frac{\partial T_{\pm}}{\partial \xi} \frac{\partial Z}{\partial \xi} + \frac{\partial T_{\pm}}{\partial \eta} \frac{\partial Z}{\partial \eta} \right) \vec{e}_Z \right\} \cdot \vec{n}, \qquad \text{(IV.50)}$$

which prescribes the temperature gradients normal to the asymptotic ring. Note that these expressions now only involve $A_{\pm}$.

Let us examine how we determine these parameters. At each physical node point, we prescribe or calculate a total of three numbers: the temperature, a scalar, and the flux, a vector, with two components. When the border of the asymptotic region (see, Figure IV.14) intersects a phase boundary, this intersection forms a corner. The flux at this corner has two components, one normal and one parallel to the boundary of the asymptotic ring, and one can use the temperature gradients in each of the two phases that intersect there to calculate these fluxes. So, for each component of the flux at the corner there are

two independent ways of calculating that component and requiring them to give the same values will allow determination of some of the new parameters. To make this idea concrete, we assign four labels to the physical node at this corner (see Figure IV.13) and label them with a three letter code. The letter represent the flux calculated from the temperature profile in the phase designated by the first letter (s = solid, l = liquid, v = vapor) at the boundary with the phased designated by the second letter (s,l,v) in the direction pointing into the region denoted by the third letter (s,l,v,a = asymptotic ring). Thus, SLa is the node for the component of the flux in the direction perpendicular to the asymptotic ring at the solid-liquid interface, calculated from the temperature profile in the solid.

The border of the asymptotic region intersects all of the phase boundaries at right angles. The component of the flux normal to the asymptotic ring at each of these nodes is in the ξ-direction. On the other hand, the component of the flux tangent to the asymptotic ring at nodes LV_v, SL_l, LS_s, and SV_v, is in the η-direction; these satisfy the usual boundary conditions, (II.2-II.4) for boundary integral formulation and requires for the discussion. All the other nodes on the asymptotic ring only have one flux component normal to the asymptotic ring, and this direction is not, in general, in the ξ-direction. Eqn. IV.37 prescribes all of those flux components normal to the asymptotic ring. In the liquid region at node LV_a, on the liquid-vapor interface, the asymptotic flux reduces to

$$\left.\frac{\partial T_+}{\partial n}\right|_{\eta=\varphi} = \nabla T_+\big|_{\eta=\varphi}\cdot\bar{e}_\xi$$
$$= \left(\frac{1}{H_\xi}\frac{\partial T_+}{\partial \xi}\bar{e}_\xi + \frac{1}{H_\eta}\frac{\partial T_+}{\partial \eta}\bar{e}_\eta\right)\Bigg|_{\eta=\varphi}\cdot\bar{e}_\xi = \left.\frac{1}{H_\xi}\frac{\partial T_+}{\partial \xi}\right|_{\eta=\varphi} = 0, \qquad \text{(IV.51)}$$

which follows from Equation (IV.45) and the fact that liquid-vapor interface (the ξ-direction) is the T = 0 isotherm. Thus, the flux at the nodes LS_a, and SL_a on the

solid-liquid interface will determine $A_{\pm}$. The component of the flux that is normal to the asymptotic ring there is tangent to the solid-liquid interface, i.e.,

$$\left.\frac{\partial T_{\pm}}{\partial n}\right|_{\eta=0} = -\left.\frac{\partial T_{\pm}}{\partial R}\right|_{Z+d=0,R>c} =$$

$$= \frac{1}{H_\eta^2}\left[\left(\frac{\partial T_{\pm}}{\partial \xi}\frac{\partial R}{\partial \xi}+\frac{\partial T_{\pm}}{\partial \eta}\frac{\partial R}{\partial \eta}\right)\bar{e}_R+\left(\frac{\partial T_{\pm}}{\partial \xi}\frac{\partial Z}{\partial \xi}+\frac{\partial T_{\pm}}{\partial \eta}\frac{\partial Z}{\partial \eta}\right)\bar{e}_Z\right]_{\eta=0}\cdot\bar{e}_R \quad \text{(IV.52)}$$

$$= \frac{1}{H_\eta^2}\left(\frac{\partial T_{\pm}}{\partial \xi}\frac{\partial R}{\partial \xi}+\frac{\partial T_{\pm}}{\partial \eta}\frac{\partial R}{\partial \eta}\right)\Bigg|_{\eta=0} = \left.\frac{1}{H_\eta^2}\frac{\partial T_{\pm}}{\partial \xi}\frac{\partial R}{\partial \xi}\right|_{\eta=0}$$

Since the temperatures are continuous along solid-liquid interface, so are their tangential derivatives. Thus, on either side, $\left(\frac{\partial T_-}{\partial R}-\frac{\partial T_+}{\partial R}\right)\Big|_{Z+d=0,R>c} = 0$ and $A_- = A_+ = A^*$.

Now, since we prescribe the flux on the asymptotic ring in terms of A^*, we need an additional relation to establish its value. This relation must be some sort of self-consistency statement since A^* controls the magnitude of the heat flux to the contact line, and this quantity must satisfy the overall heat balance implied by the boundary integral. The idea is that just as the asymptotic solution prescribes the heat flux on the asymptotic ring, it should also give numerically accurate values for the temperatures along the solid-vapor interface, say, very close to the asymptotic ring. That is, $T_-(\xi,\eta) \to A^* g_-(\xi,\eta)$, where $g_-(\xi,\eta) = e^{-\xi\beta}\cos\beta(\eta+\pi)\sin\varphi\beta$, as $\xi\to\infty$ (see Equation (IV.56) below). Thus, for each of the solid-vapor interfacial node whose distances to the contact line are less than 5% of the radius of the dry spot, write

$$T_{\ell,v}(\xi_i,\eta_i) \approx A^* g_-(\xi_i,\eta_i). \quad \text{(IV.53)}$$

Employing method of the least square, i.e.,

$$\begin{cases} \dfrac{\partial}{\partial A^*}\left(\sum\left(T_{v,s}(i) - A^* g_-(\xi_i,\eta_i)\right)^2\right) = 0 \\ \text{for all i such that } \eta_i = -\pi, \text{ and } \left|\left(\dfrac{\sinh\xi_i - \cosh\xi_i - 1}{\cosh\xi_i + 1}\right)\right| \le 0.05, \end{cases} \tag{IV.54}$$

one finds

$$A^* = \frac{\sum T_{\ell,s}(i) g(\xi_i,-\pi)}{\sum g^2(\xi_i,-\pi)}. \tag{IV.55}$$

Finally, if the radius of the asymptotic ring is very small, i.e., $\xi >> 1$, it becomes inconvenient to evaluate (IV.37)-(IV.38) directly, and large ξ asymptotic forms of these relations are useful. So,

$$\xi \underset{\xi\to\infty}{\to} \ln\sqrt{\frac{(c+R)^2+(Z+d)^2}{(c-R)^2+(Z+d)^2}} \text{ and } \sqrt{2\cosh\xi - 2\cos\eta}\, e^{-\xi/2} \underset{\xi\to\infty}{\to} 1. \tag{IV.56}$$

This leads to

$$T_+ = A^*\left(\sqrt{\frac{(c-R)^2+(Z+d)^2}{(c+R)^2+(Z+d)^2}}\right)^{\beta} \sin\beta(\varphi-\eta)\,\cos\pi\beta \tag{IV.57}$$

$$T_- = A^*\left(\sqrt{\frac{(c-R)^2+(Z+d)^2}{(c+R)^2+(Z+d)^2}}\right)^{\beta} \cos((\eta+\pi)\beta)\sin\varphi\beta, \tag{IV.58}$$

where (IV.11) defines η, both as $\xi\to\infty$.

Node placement: let us now discuss how we choose the size of the asymptotic region and how we choose the node points for the boundary integral calculation. Due to the geometrical and physical singularities, the mesh generating technique in the region of the contact line is critical. On one hand, one must put enough nodes near the contact line to ensure accuracy; on the other hand, one

would like to minimize the number of nodes to avoid prohibitive computational work. We use roughly 30 (20 in the solid region, a minimum of 10 and maximum of 20 in the liquid region, depending on the contact angle) equally spaced points on the liquid and solid portion of the boundary between the asymptotic region and the boundary integral domain. We have determined this number to be large enough so that an increase in the number of points on the asymptotic ring does not change the numerical results. On the rest of the boundary integral domain's boundary, the distance between adjacent nodes is exponentially larger: The intersection of the asymptotic ring with each phase boundaries contains three nodes. The distances between this three node cluster and the nearest phase boundary nodes not on the asymptotic ring is the same as that between nodes on the asymptotic ring. The distance to each subsequent node is 1.5 that to the previous node (see Figure IV.14c) until the distance between the two nodes reaches a maximum length determined by the global size of the cell.

Size of the asymptotic region: It would seem reasonable to choose the radius of the ring proportional to the radius of the dry spot. It is also reasonable to anticipate that, the numerical results this scheme produces converge to Sadhal's solution when the cell radius and the solid and liquid layer thicknesses are large enough. For $H = h = R_c = 40$, one should find that as the number of nodes on the asymptotic ring increases and as the ring's radius decreases, the results converges steadily towards Sadhal's solution for all contact angles and conductivity ratios. Table IV.1 presents the Nusselt number results for three values $\kappa = 0.001$, 0.01 and 0.1 of the conductivity ratio, five values contact angles $\varphi = 30°,60°,90°,120°$ and 150°and decreasing ring radius. For all the cases, the results converge to Sadhal's when the ratio $\delta_{in} = R_{asymp}/R_c$ of the radii of the asymptotic ring and the dry spot is smaller than 0.001. For δ_{in} smaller than 0.001, the numerical computation become prohibitively long, the improvement in accuracy is rather slow, and the technique is not always viable. In actual calculations, we find that a

ratio of radii of about 0.001 gives accurate results, yet does not require a very large number of nodes.

Appendix.B

HEAT FLUX NEAR THE CONTACT LINE WHEN BUBBLE-BUBBLE DISTANCES ARE MUCH SMALLER THAN THE DRY SPOT RADIUS

From the discussion of the heat flux near the contact line, we know that the contact line acts as major heat sink around which most of the evaporation takes place. When the radius of the periodic cell approaches the radius of the bubble, the contact lines of the neighboring cells approach each other. If the contact angle of the bubble is smaller than 90°, then neighboring bubbles will merge before the contact lines meet, i.e., before $R_c' = c'$. However, when the contact angle is larger than 90°, the contact lines meet as R_c' approaches a'. In either case, the use of an asymptotic expansion of Sadhal's solution for infinite domains to describe the contact line region is likely not valid here. The reasoning behind that assumption was that the large temperature gradients near the contact line are probable very insensitive to the conditions far away from the contact line, where "far" denotes distances large compared with the bubble radius. The situation in question clearly violates this assumption.

Note that when the two contact lines approach each other, as in the small cell cases, the distance between the contact lines becomes much smaller than a'; thus the problem becomes two dimensional. (Note that the artificial geometry assumed in taking axisymmetric cells with periodic boundary conditions is particularly apt for this two-dimensional approximation.) Furthermore, assume as before that the boundary conditions far from the contact lines are not important to the form of the solution; so we have a two-dimensional problem with two interfaces, each say with contact angle φ, that are a distance $2\alpha_c = 2(R_c - c)$ apart, have liquid between them and vapor on their outer sides. Our interest is to come up with an asymptotic solution that is valid *close to the contact lines*, i.e., for

distances r from the contact line that are much smaller that α_c; thus the exact shape of the liquid-vapor boundary far from the contact line, i.e., for $r << \alpha_c$, is unimportant. We use this insensitivity to analyze a problem (Figure IV.15) that resembles the true situation close to the contact line but differs from it far from the contact line and admits an analytical solution. The picture sets up a two dimensional complex plane $\alpha = \alpha_1 + i\alpha_2$, with real axis α_1 along the solid-liquid interface, the origin at the edge $R = R_c$ of the cell, and $\pm\alpha_c$ as the points of intersection of the two contact lines with the solid. In contrast to the "true" geometry where the vapor regions are bounded and the liquid region is unbounded, we use the fact that most of the vapor-liquid boundary is far from the contact line to choose a bounded liquid and an unbounded vapor region. This configuration allows solution via conformal mapping. As such, the liquid is a spherical cap of contact angle φ, measured in the liquid, and of radius $\alpha_c/\sin(\varphi)$, with its center at $-i\alpha_c/\tan(\varphi)$. The temperature boundary conditions are: On the spherical arc, where the liquid-vapor interface is, the temperature is zero; at the solid-liquid interface, the temperature and the heat flux are continuous, and the vapor-solid interface is insulating, i.e.,

$$T_+(\alpha_1,\alpha_2) = 0 \quad \begin{cases} \text{when} \quad \alpha_2 \geq 0 \quad \text{and} \\ \alpha_1^2 + \left(\alpha_2 + \alpha_c/\tan(\varphi)\right)^2 = \left(\alpha_c/\sin(\varphi)\right)^2 \end{cases} \tag{IV.59}$$

$$\begin{cases} T_+(\alpha_1,\alpha_2) - T_-(\alpha_1,\alpha_2) = 0 \\ \dfrac{\partial\left(\kappa T_+(\alpha_1,\alpha_2) - T_-(\alpha_1,\alpha_2)\right)}{\partial\alpha_2} = 0, \quad \text{for} \quad |\alpha_1| \leq \alpha_C, \ \alpha_2 = 0, \end{cases} \tag{IV.60}$$

$$\frac{\partial T_-(\alpha_1,\alpha_2)}{\partial\alpha_2} = 0, \quad |\alpha_1| \geq \alpha_C, \ \alpha_2 = 0. \tag{IV.61}$$

One can conformally map the solid, vapor and liquid regions in the α-plane on to three infinite strips in the ω-plane using the transformation

$$\omega := u + iv = \mathrm{Ln}\frac{\alpha - \alpha_C}{\alpha + \alpha_C} = \ln\frac{r_C}{r_A} + i(\theta_C - \theta_A) \qquad \text{(IV.62)}$$

where $\alpha - \alpha_C = r_c e^{i\theta_C} = R + iZ - (R_c - c - id)$ and $\alpha + \alpha_C = r_A e^{i\theta_A} = R + iZ - (-R_c + c - id)$. This mapping converts points A, B, C and O into A', B', C' and O', the solid-vapor interface into $v = 0$ or 2π, the liquid-vapor interface into $v = \pi - \varphi$, and the solid-liquid interface into $v = \pi$. The governing equation and all of the boundary conditions remain unchanged. That is,

$$\nabla^2 \tilde{T}_{\pm} = 0$$

$$\tilde{T}_+(u,v) = 0 \quad \text{at} \quad v = \pi - \varphi; \qquad \text{(IV.63)}$$

$$\begin{cases} \tilde{T}_+(u,v) - \tilde{T}_-(u,v) = 0 \\ \dfrac{\partial\left(\kappa\tilde{T}_+(u,v) - \tilde{T}_-(u,v)\right)}{\partial v} = 0 \end{cases} \quad \text{at} \quad v = \pi \qquad \text{(IV.64)}$$

$$\frac{\partial \tilde{T}_-(u,v)}{\partial v} = 0, \qquad v = 0,\ 2\pi \qquad \text{(IV.65)}$$

In terms of Z, R_c and c, this mapping is:

$$u = \ln\frac{\sqrt{\left(R - (2R_c - c)\right)^2 + (Z+d)^2}}{\sqrt{(R-c)^2 + (Z+d)^2}} \qquad \text{(IV.66)}$$

$$v = \sin^{-1}\left(\frac{2(Z+d)(R_c - c)}{\sqrt{(R-c)^2 + (Z+d)^2}\sqrt{\left(R - (2R_c - c)\right)^2 + (Z+d)^2}}\right). \qquad \text{(IV.67)}$$

The solutions for $\tilde{T}_{\pm}$ are

$$\tilde{T}_+(\omega) = \tilde{A}\exp(-\lambda|u|)\sin(\lambda(v - \pi + \varphi)), \qquad \text{(IV.68)}$$

$$\tilde{T}_-(\omega) = \tilde{B}\exp(-\lambda|u|)\cos(\lambda v), \qquad \text{(IV.69)}$$

where λ, $\tilde{A}$ and $\tilde{B}$ are undetermined constant. Equation (IV.68) and (IV.69) clearly satisfy (IV.63) and (IV.65). Boundary conditions (IV.64) further give

$$\tilde{B}\cos(\lambda\pi) - \tilde{A}\sin(\lambda\varphi) = 0, \tag{IV.70}$$

and the subsequent eigenvalue equation

$$\kappa = \tan(\lambda\varphi)\tan(\lambda\pi), \tag{IV.71}$$

which is identical to (IV.29). Finally, the transform back to the R-Z plane gives the temperature distributions,

$$T_+(R,Z) = \tilde{A}\cos(\lambda\pi)\left(\frac{\sqrt{(R-c)^2+(Z+d)^2}}{\sqrt{(R-2R_c+c)^2+(Z+d)^2}}\right)^{\lambda} \sin\lambda\left(\sin^{-1}\left(\frac{2(Z+d)(R_c-c)}{\sqrt{(R-c)^2+(Z+d)^2}\sqrt{(R-2R_c+c)^2+(Z+d)^2}}\right)-\pi+\varphi\right) \tag{IV.72}$$

$$T_-(R,Z) = \tilde{A}\sin(\lambda\varphi)\left(\frac{\sqrt{(R-c)^2+(Z+d)^2}}{\sqrt{(R-(2R_c-c))^2+(Z+d)^2}}\right)^{\lambda} \cos\lambda\left(\sin^{-1}\left(\frac{2(Z+d)(R_c-c)}{\sqrt{(R-c)^2+(Z+d)^2}\sqrt{(R-(2R_c-c))^2+(Z+d)^2}}\right)\right) \tag{IV.73}$$

which resembles the expressions (IV.57) and (IV.58). To obtain the asymptotic profiles and the value of the constant $\tilde{A}$, we proceed in a manner exactly analogous to that presented in the previous appendix.

Table IV.1A Comparison of exact (Sadhal, 1989) and Boundary Integral Nusselt Numbers of attached bubbles for different φ, and δ_{in}, when $\kappa = 0.1$

	β	Exact Nu	Numerical Nu	Error in %
$\delta_{in} = .1$				
$\varphi = 30°$	0.247	2.397	2.644	*0.10*
60°	0.174	2.718	2.955	*0.09*
90°	0.142	2.930	3.108	*0.06*
120°	0.123	3.017	3.129	*0.04*
150°	0.110	2.972	3.029	*0.02*
$\delta_{in} = .01$				
$\varphi = 30°$	0.247	2.397	2.508	*0.05*
60°	0.174	2.718	2.902	*0.07*
90°	0.142	2.930	3.139	*0.07*
120°	0.123	3.017	3.220	*0.07*
150°	0.110	2.972	3.150	*0.06*
$\delta_{in} = .001$				
$\varphi = 30°$	0.247	2.397	2.441	*0.02*
60°	0.174	2.718	2.821	*0.04*
90°	0.142	2.930	3.072	*0.05*
120°	0.123	3.017	3.174	*0.05*
150°	0.110	2.972	3.125	*0.05*
$\delta_{in} = .0001$				
$\varphi = 30°$	0.247	2.397	2.415	*0.01*
60°	0.174	2.718	2.768	*0.02*
90°	0.142	2.930	3.010	*0.03*
120°	0.123	3.017	3.112	*0.03*
150°	0.110	2.972	3.071	*0.03*
$\delta_{in} = .00001$				
$\varphi = 30°$	0.247	2.397	2.406	*0.00*
60°	0.174	2.718	2.744	*0.01*
90°	0.142	2.930	2.974	*0.01*
120°	0.123	3.017	3.073	*0.02*
150°	0.110	2.972	3.033	*0.02*

Table IV.1B Comparison of exact (Sadhal, 1989) and Boundary Integral Nusselt numbers of attached bubbles for different φ, and δ_{in}, when $\kappa = 0.01$

	β	Exact Nu	Numerical Nu	Error in %
$\delta_{in} = .1$				
$\varphi = 30°$	0.078	6.811	6.874	*0.01*
60°	0.055	8.565	8.367	*0.02*
90°	0.045	9.623	9.229	*0.04*
120°	0.039	10.091	9.563	*0.05*
150°	0.035	10.021	9.419	*0.06*
$\delta_{in} = .01$				
$\varphi = 30°$	0.078	6.811	7.170	*0.05*
60°	0.055	8.565	8.900	*0.04*
90°	0.045	9.623	9.895	*0.03*
120°	0.039	10.091	10.287	*0.02*
150°	0.035	10.021	10.139	*0.01*
$\delta_{in} = .001$				
$\varphi = 30°$	0.078	6.811	7.182	*0.05*
60°	0.055	8.565	9.018	*0.05*
90°	0.045	9.623	10.080	*0.05*
120°	0.039	10.091	10.512	*0.04*
150°	0.035	10.021	10.378	*0.04*
$\delta_{in} = .0001$				
$\varphi = 30°$	0.078	6.811	7.100	*0.04*
60°	0.055	8.565	8.965	*0.05*
90°	0.045	9.623	10.051	*0.04*
120°	0.039	10.091	10.502	*0.04*
150°	0.035	10.021	10.382	*0.04*
$\delta_{in} = .00001$				
$\varphi = 30°$	0.078	6.811	7.023	*0.03*
60°	0.055	8.565	8.894	*0.04*
90°	0.045	9.623	9.993	*0.04*
120°	0.039	10.091	10.456	*0.04*
150°	0.035	10.021	10.347	*0.03*

Table IV.1C: Comparison of exact (Sadhal, 1989) and Boundary Integral Nusselt Numbers of attached bubbles for different φ, and δ_{in}, when $\kappa = 0.001$

	β	Exact Nu	Numerical Nu	Error in %
$\delta_{in} = .1$				
$\varphi = 30°$	0.025	20.560	19.231	*0.06*
60°	0.017	27.270	25.140	*0.08*
90°	0.014	31.196	28.560	*0.08*
120°	0.012	32.962	30.049	*0.09*
150°	0.011	32.833	29.846	*0.09*
$\delta_{in} = .01$				
$\varphi = 30°$	0.025	20.560	20.613	*0.00*
60°	0.017	27.270	27.071	*0.01*
90°	0.014	31.196	30.805	*0.01*
120°	0.012	32.962	32.428	*0.02*
150°	0.011	32.833	32.203	*0.02*
$\delta_{in} = .001$				
$\varphi = 30°$	0.025	20.560	21.111	*0.03*
60°	0.017	27.270	27.801	*0.02*
90°	0.014	31.196	31.671	*0.02*
120°	0.012	32.962	33.358	*0.01*
150°	0.011	32.833	33.135	*0.01*
$\delta_{in} = .0001$				
$\varphi = 30°$	0.025	20.560	21.158	*0.03*
60°	0.017	27.270	27.900	*0.02*
90°	0.014	31.196	31.800	*0.02*
120°	0.012	32.962	33.503	*0.02*
150°	0.011	32.833	33.285	*0.01*
$\delta_{in} = .00001$				
$\varphi = 30°$	0.025	20.560	21.128	*0.03*
60°	0.017	27.270	27.888	*0.02*
90°	0.014	31.196	31.798	*0.02*
120°	0.012	32.962	33.508	*0.02*
150°	0.011	32.833	33.294	*0.01*

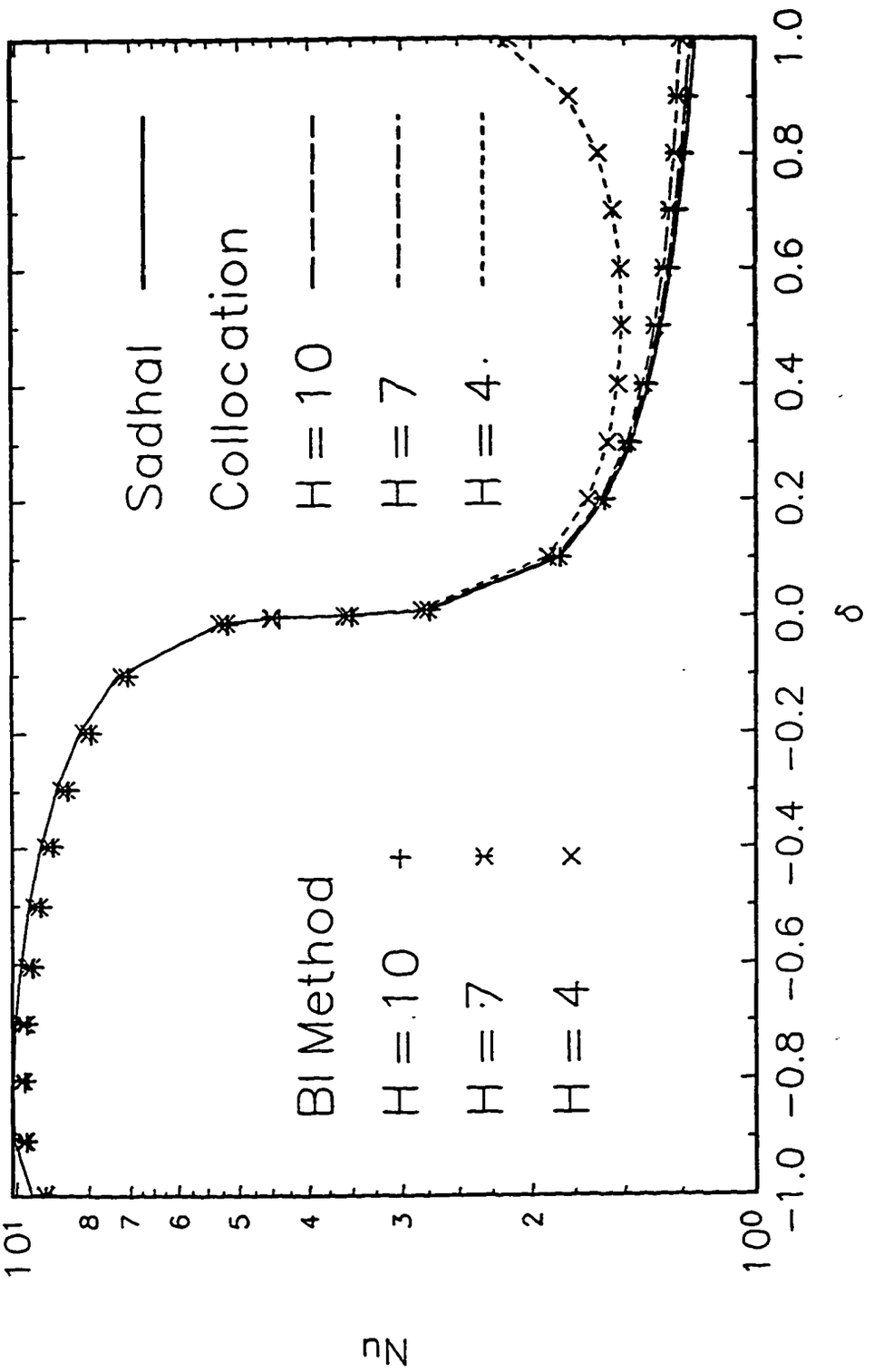

Figure IV.1
R_c=10 T_f=1 κ=0.01

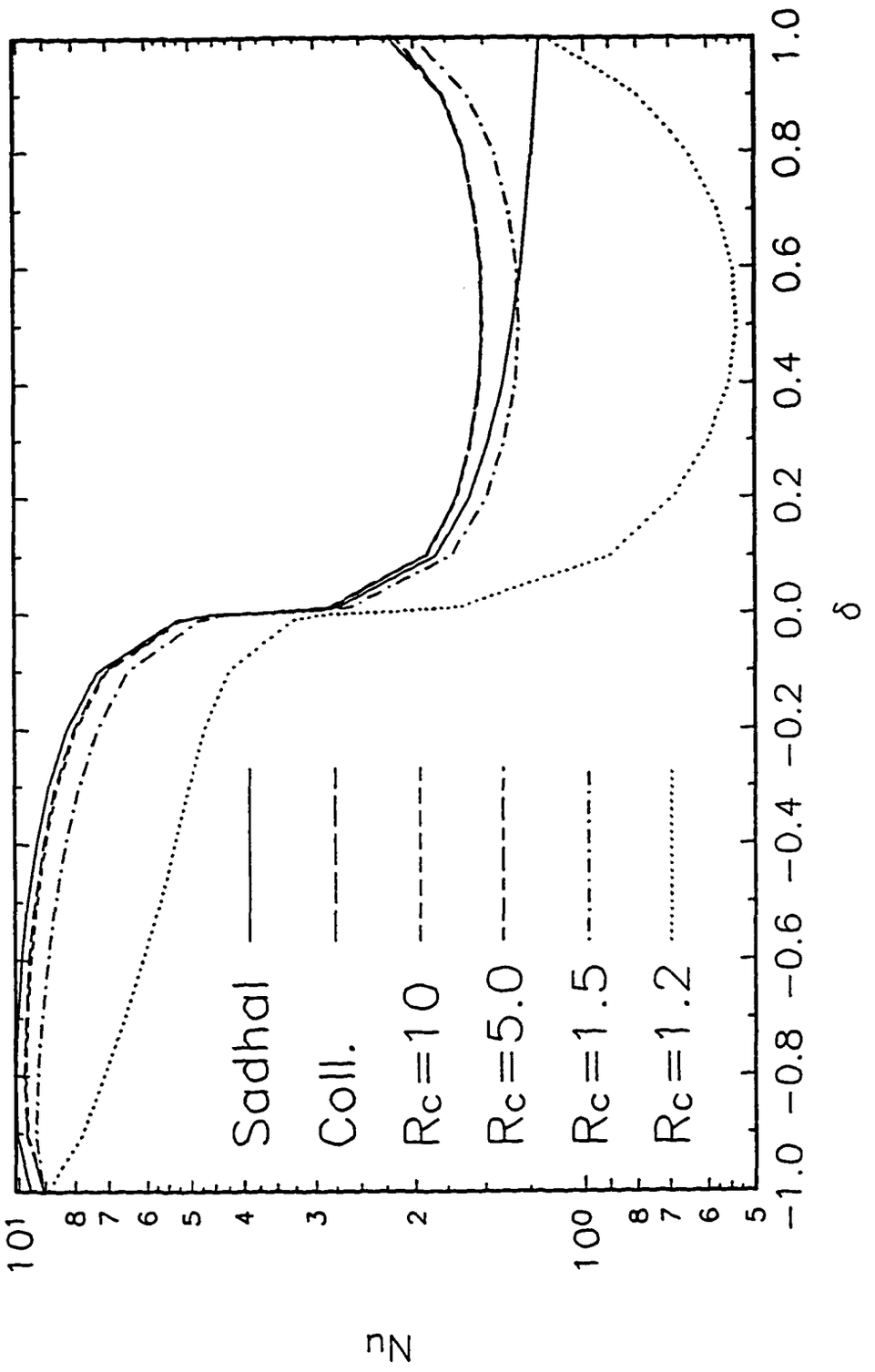

Figure IV.2
H=h=4 Tf=1, κ=0.01

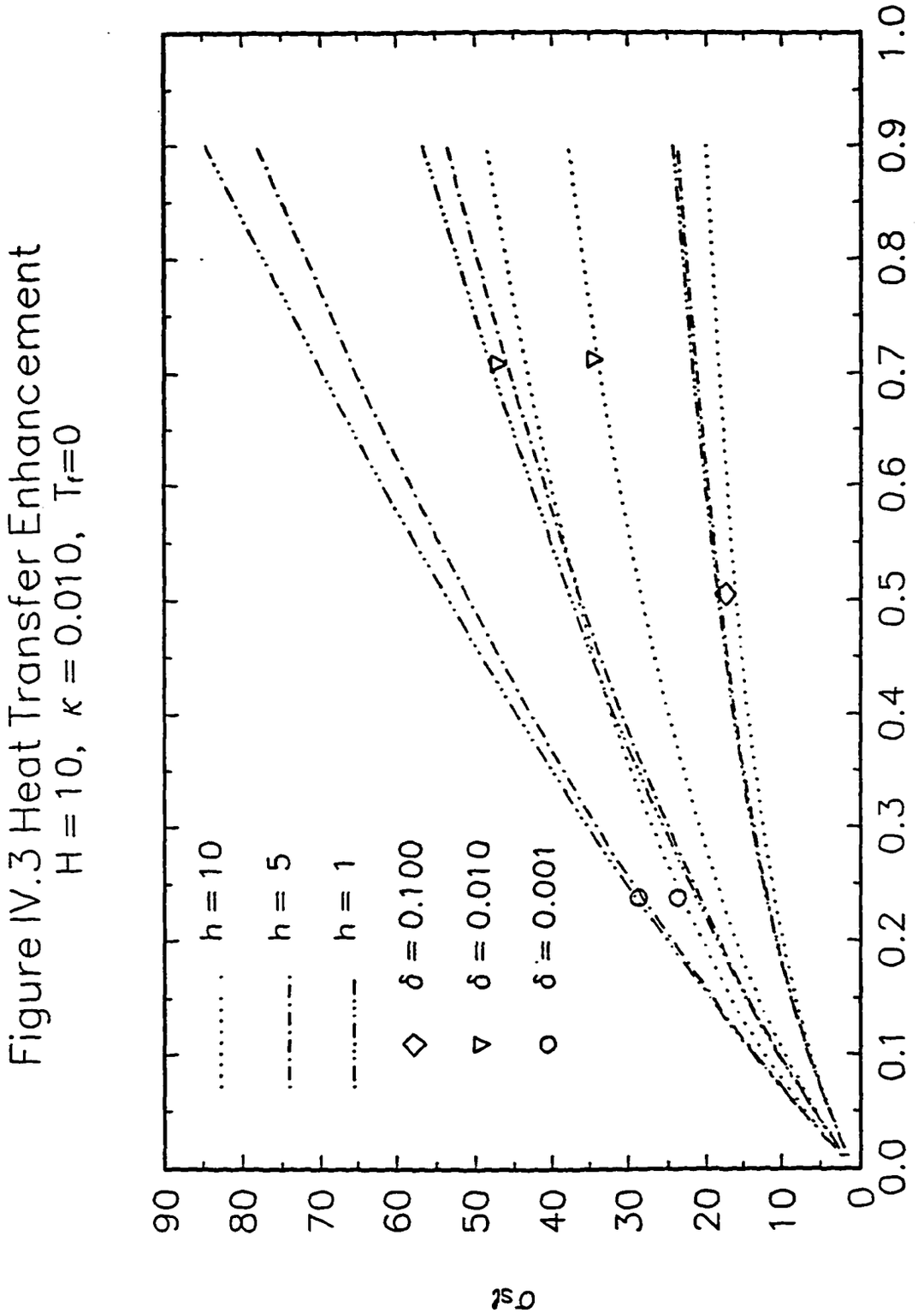

Figure IV.3 Heat Transfer Enhancement
H = 10, κ = 0.010, T_r=0

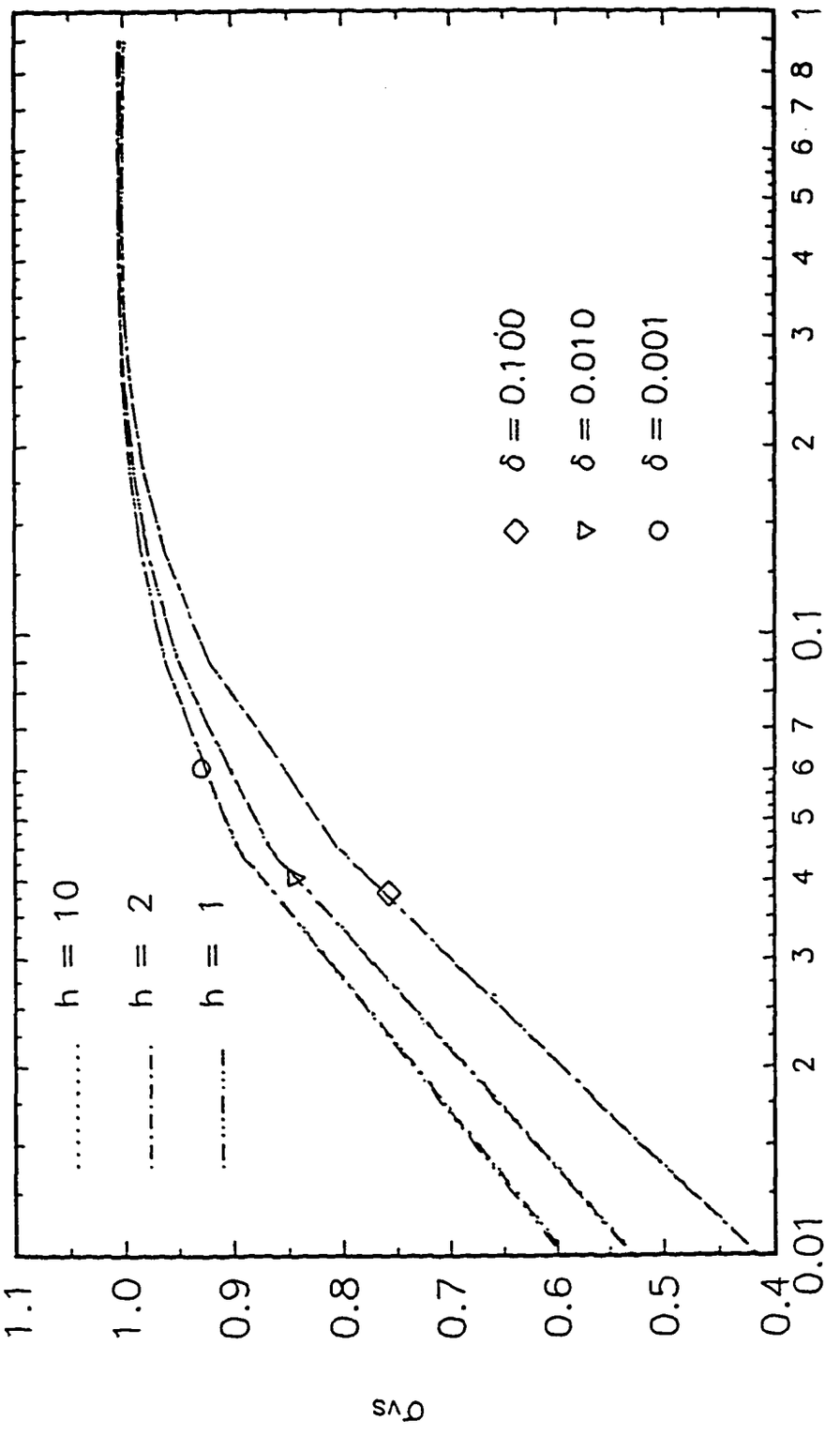

Figure IV.4 σ_{vs} vs. ω
$H = 10$, $\kappa = 0.010$, $T_f = 0$

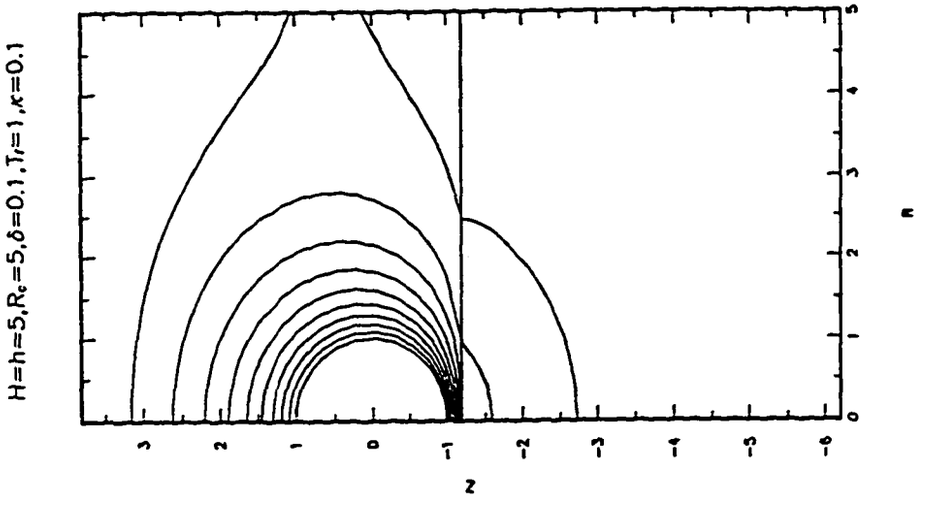

Figure IV.5.1 (a)

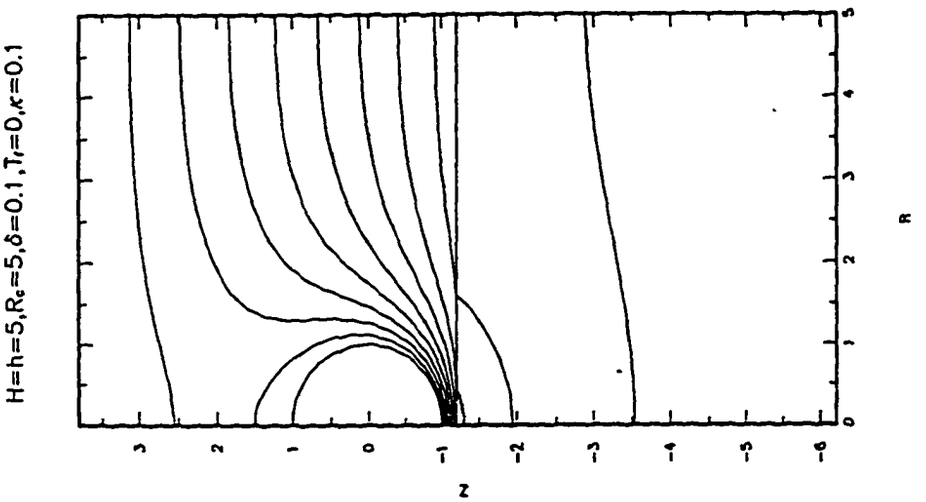

Figure IV.5.1 (b)

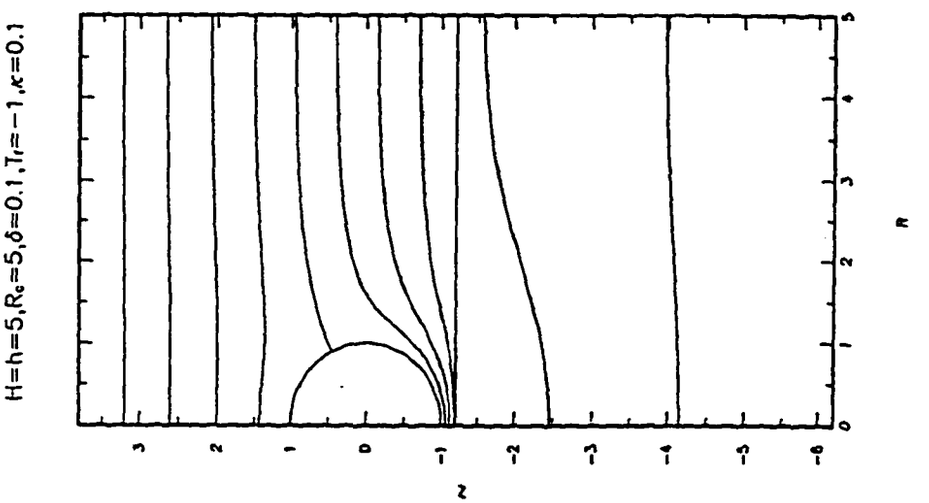

Figure IV.5.1(c)

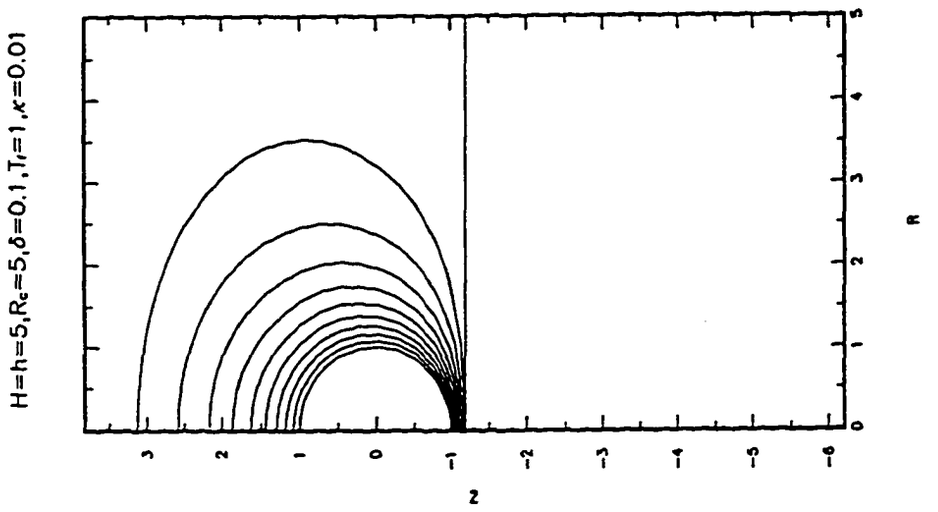

Figure IV.5.2(a)

H=h=5,R_e=5,δ=0.1,T_i=1,κ=0.01

Figure IV.5.2(b)

H=h=5,R_e=5,δ=0.1,T_i=0,κ=0.01

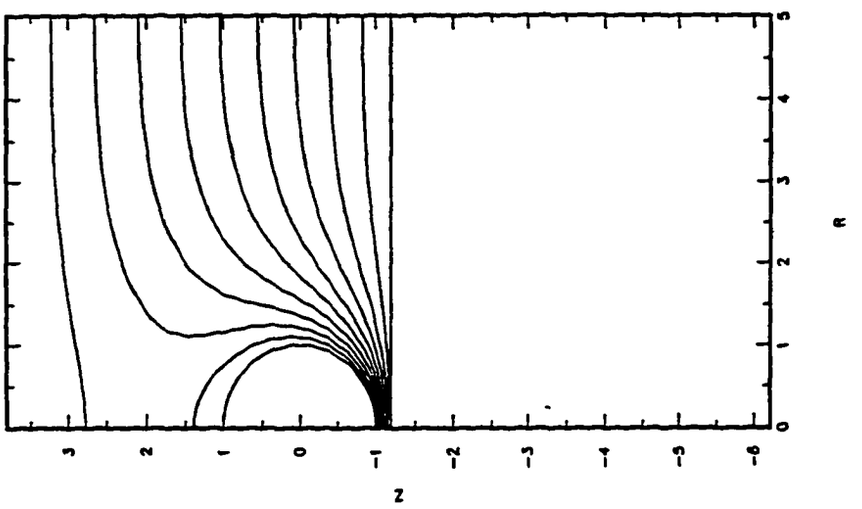

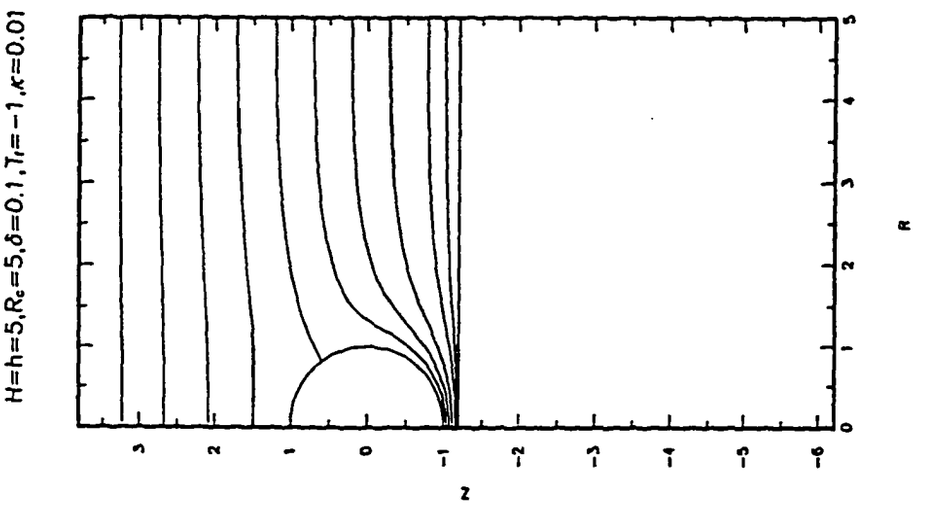

Figure IV.5.2(c)

Figure IV.6.1(a)

H=h=5,R_c=2.5,δ=0.1,T_f=1,κ=0.1

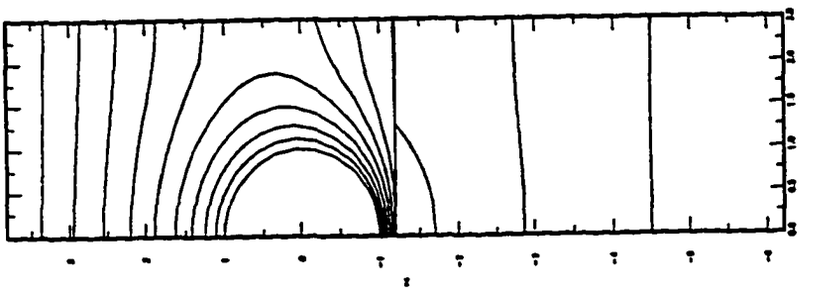

Figure IV.6.1 (b)

H=h=5,R_c=2.5,δ=0.1,T_f=0,κ=0.1

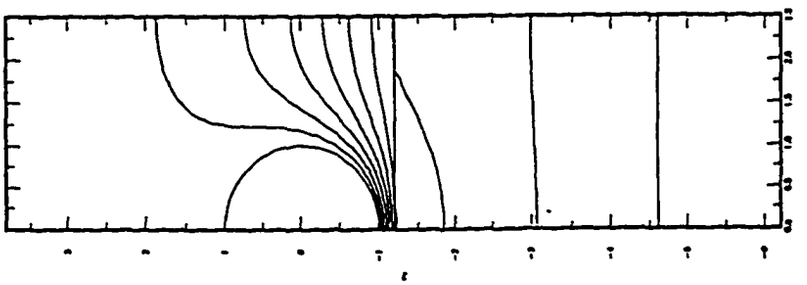

Figure IV.6.1(c)

H=h=5,R_e=2.5,δ=0.1,T_i=−1,κ=0.1

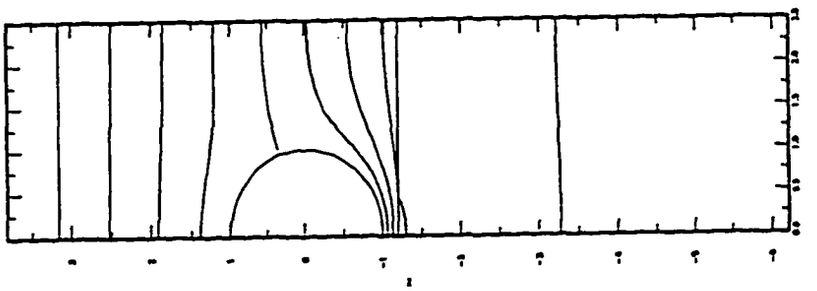

Figure IV.6.2(a)

H=h=5,R_c=2.5,δ=0.1,T_1=1,κ=0.01

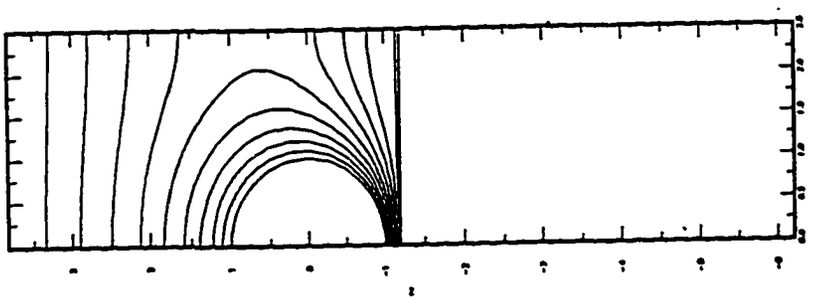

Figure IV.6.2(b)

H=h=5,R_e=2.5,δ=0.1,T_f=0,κ=0.01

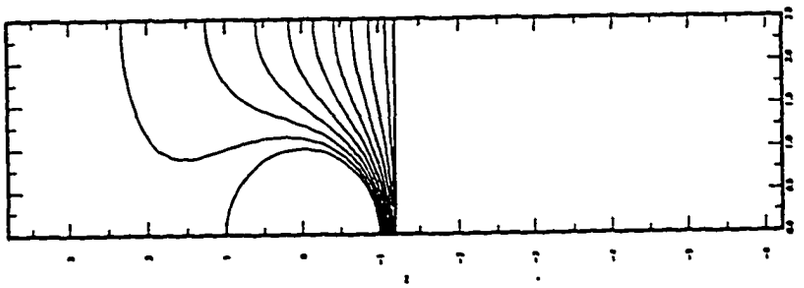

Figure IV.6.2(c)

$H=h=5, R_c=2.5, \delta=0.1, T_i=-1, \kappa=0.01$

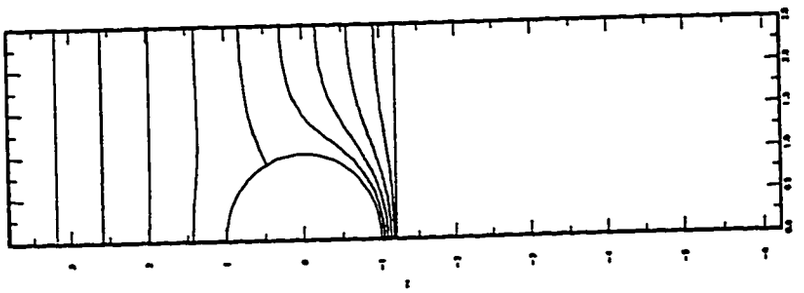

Figure IV.7a

$T_f=1$

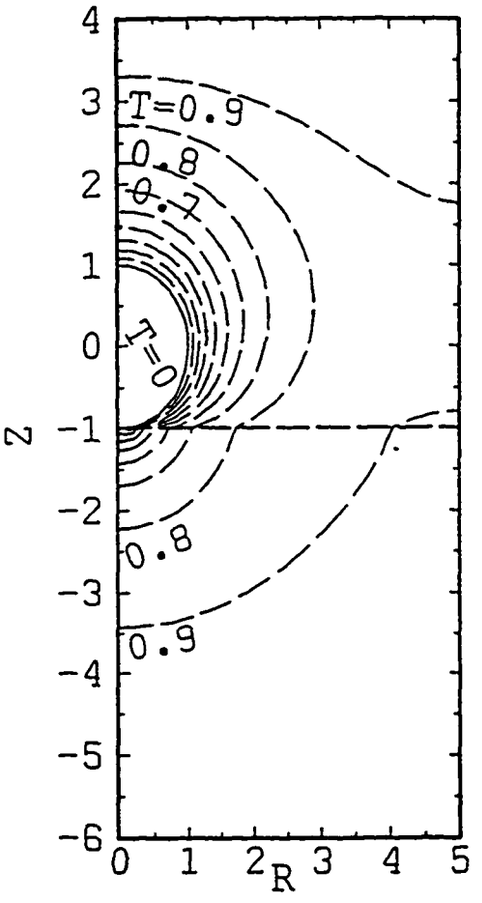

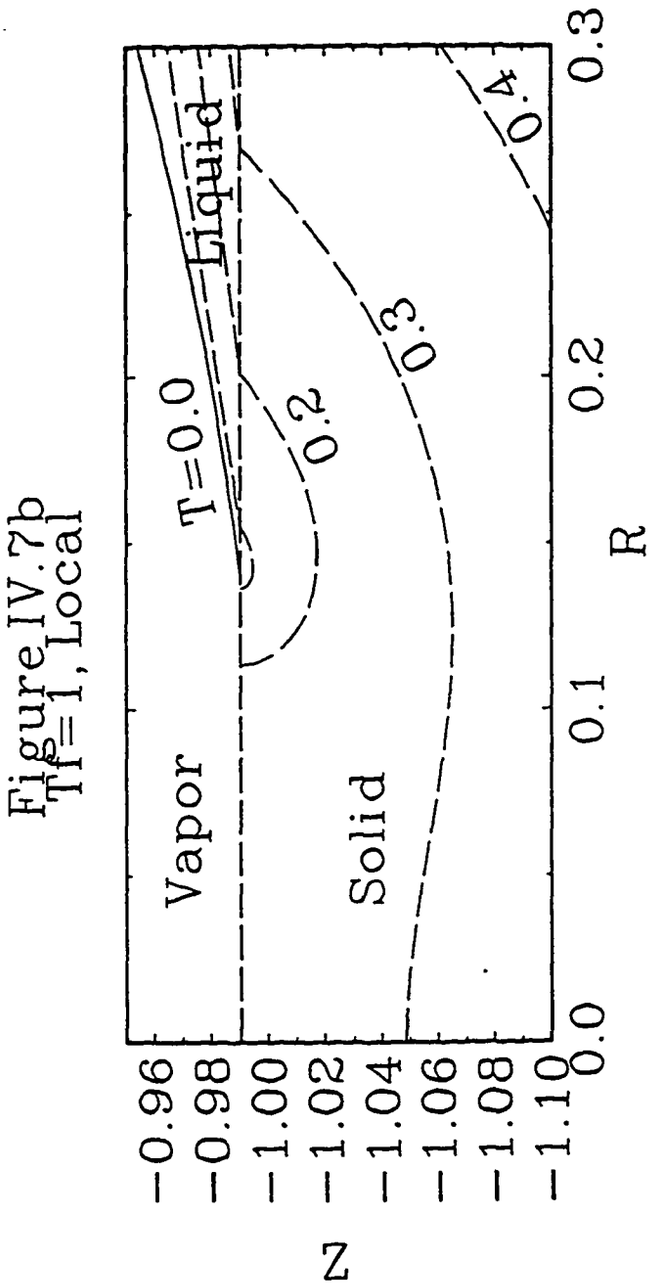

Figure IV.7b
T_f=1, Local

Figure IV.8a

$T_\varepsilon=0$

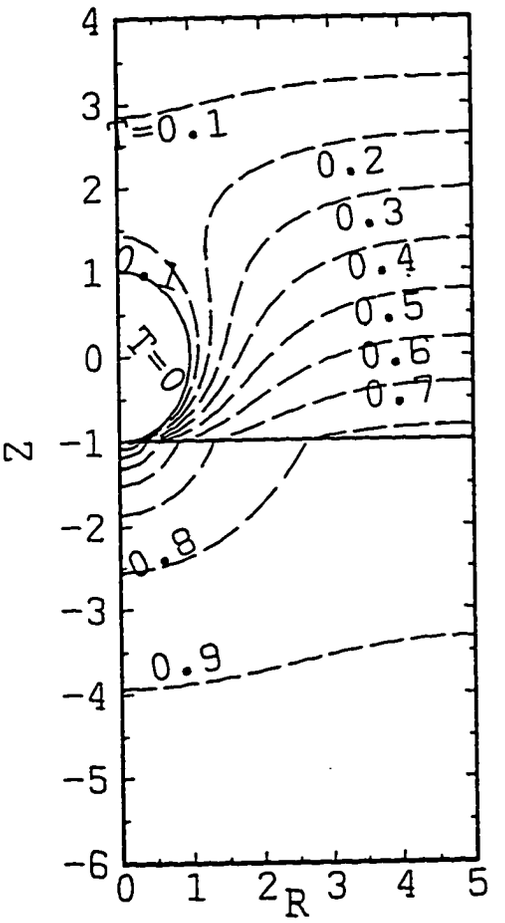

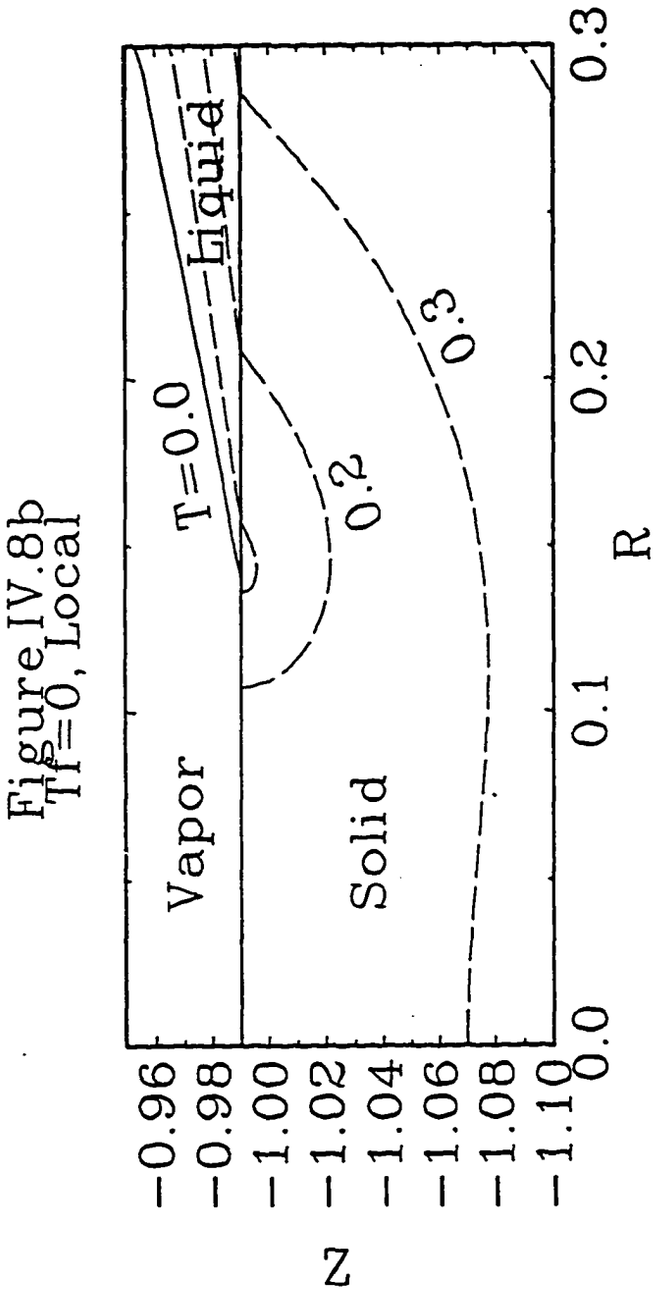

Figure IV.8b
T_f=0, Local

Figure IV.9a

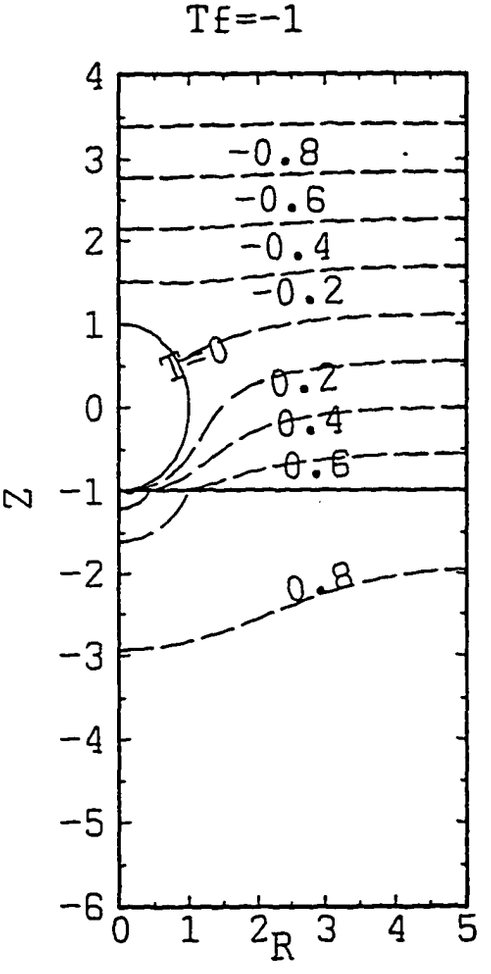

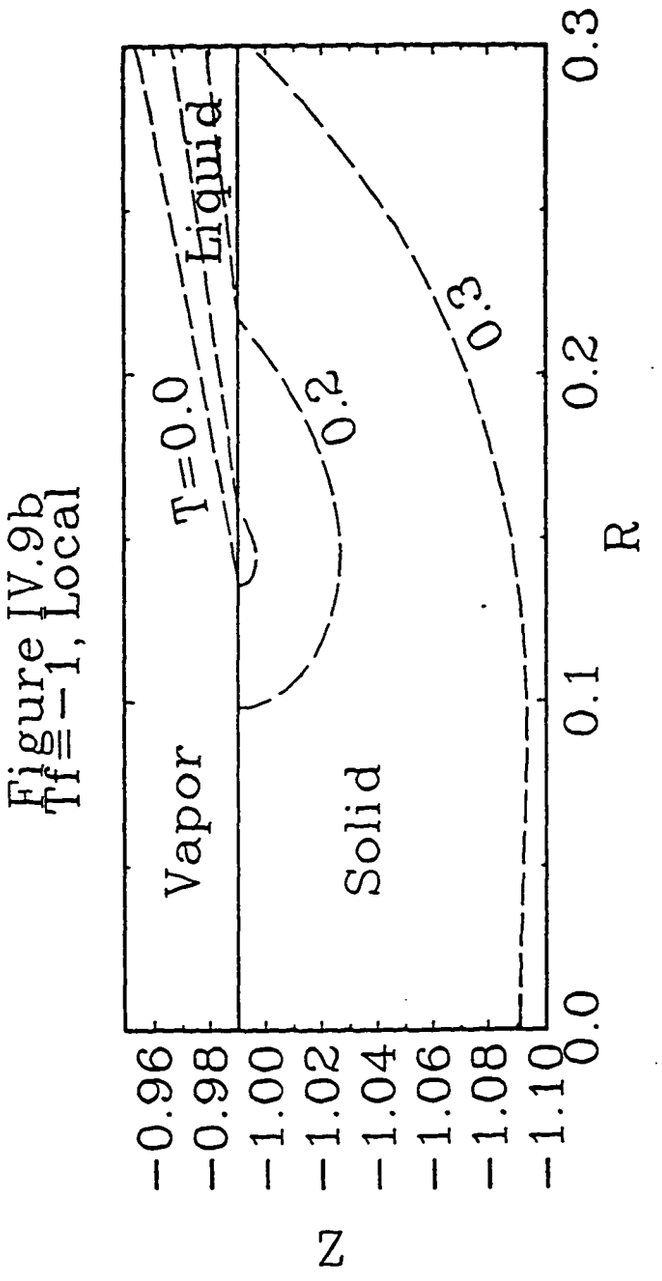

Figure IV.9b
$T_f = -1$, Local

Figure IV.10
Heat Transfer Enhancement, $T_f=0$

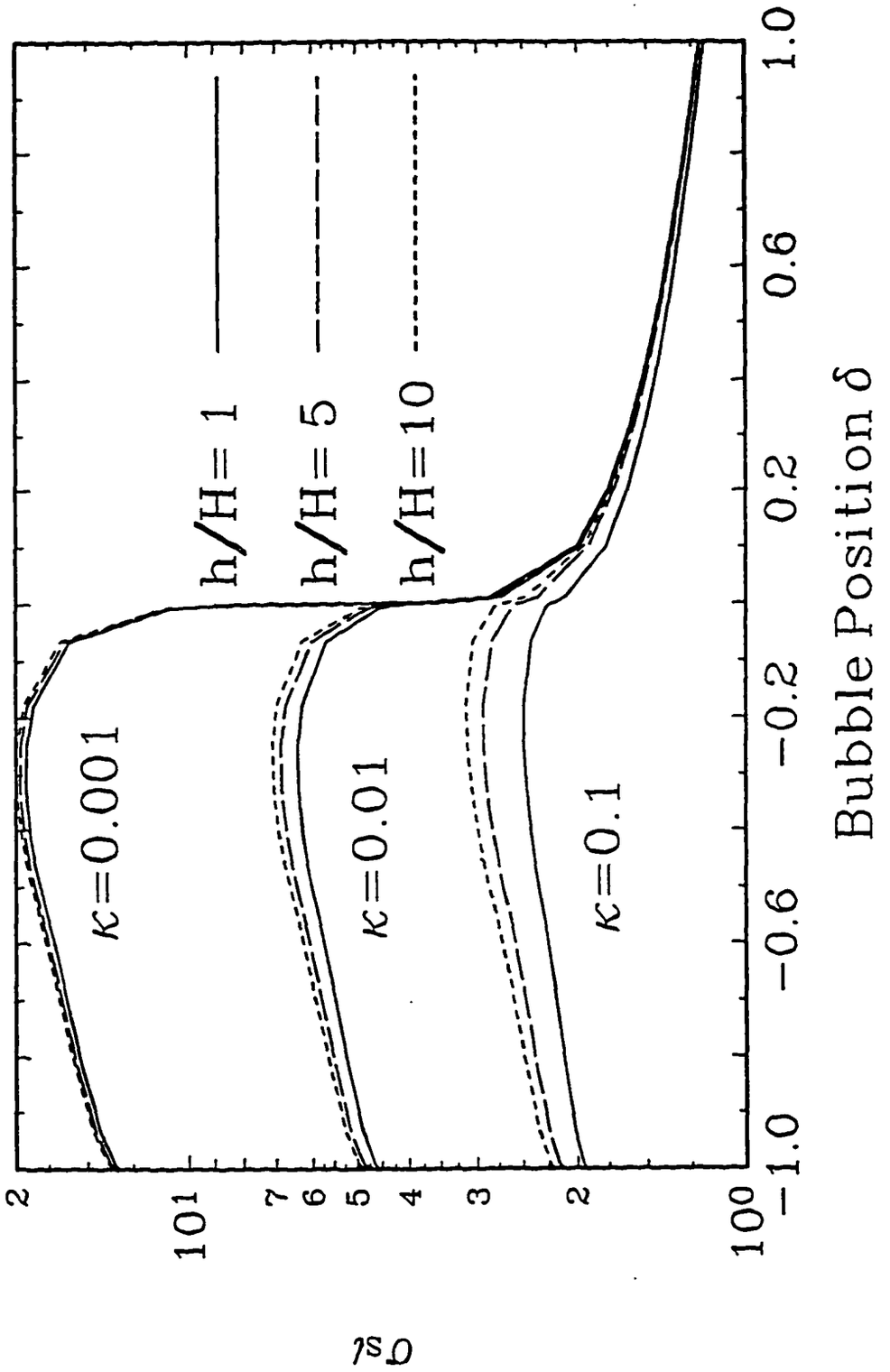

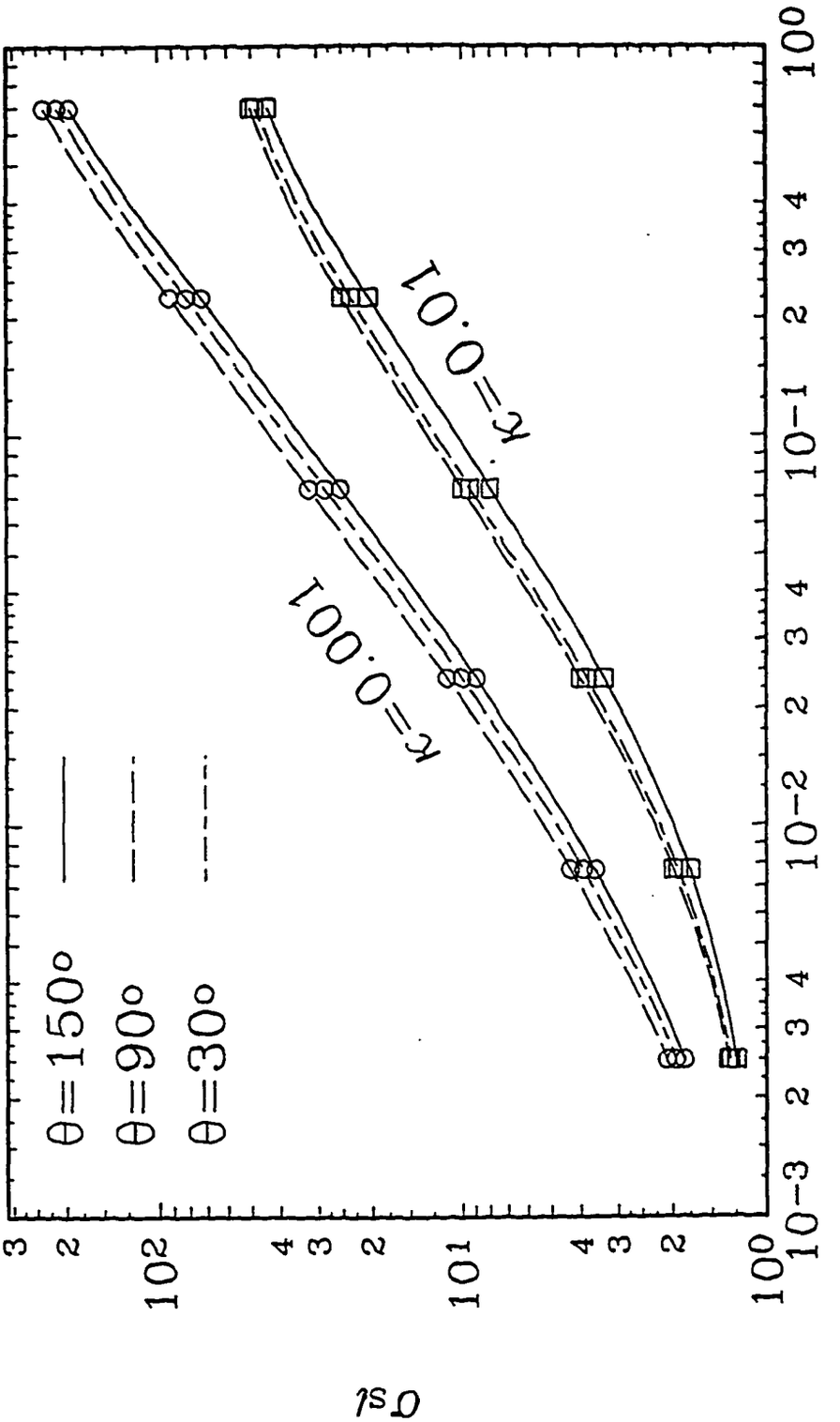

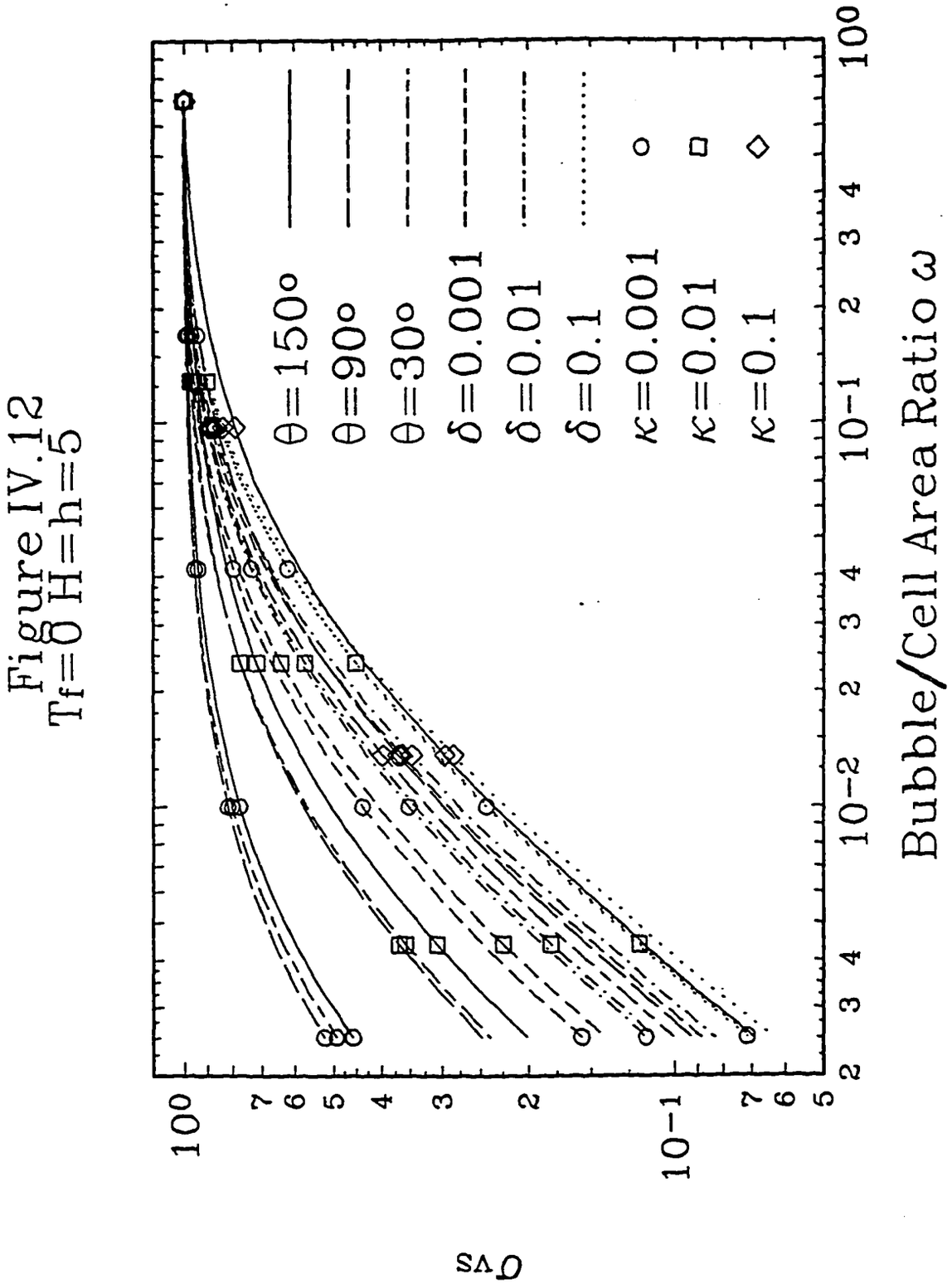

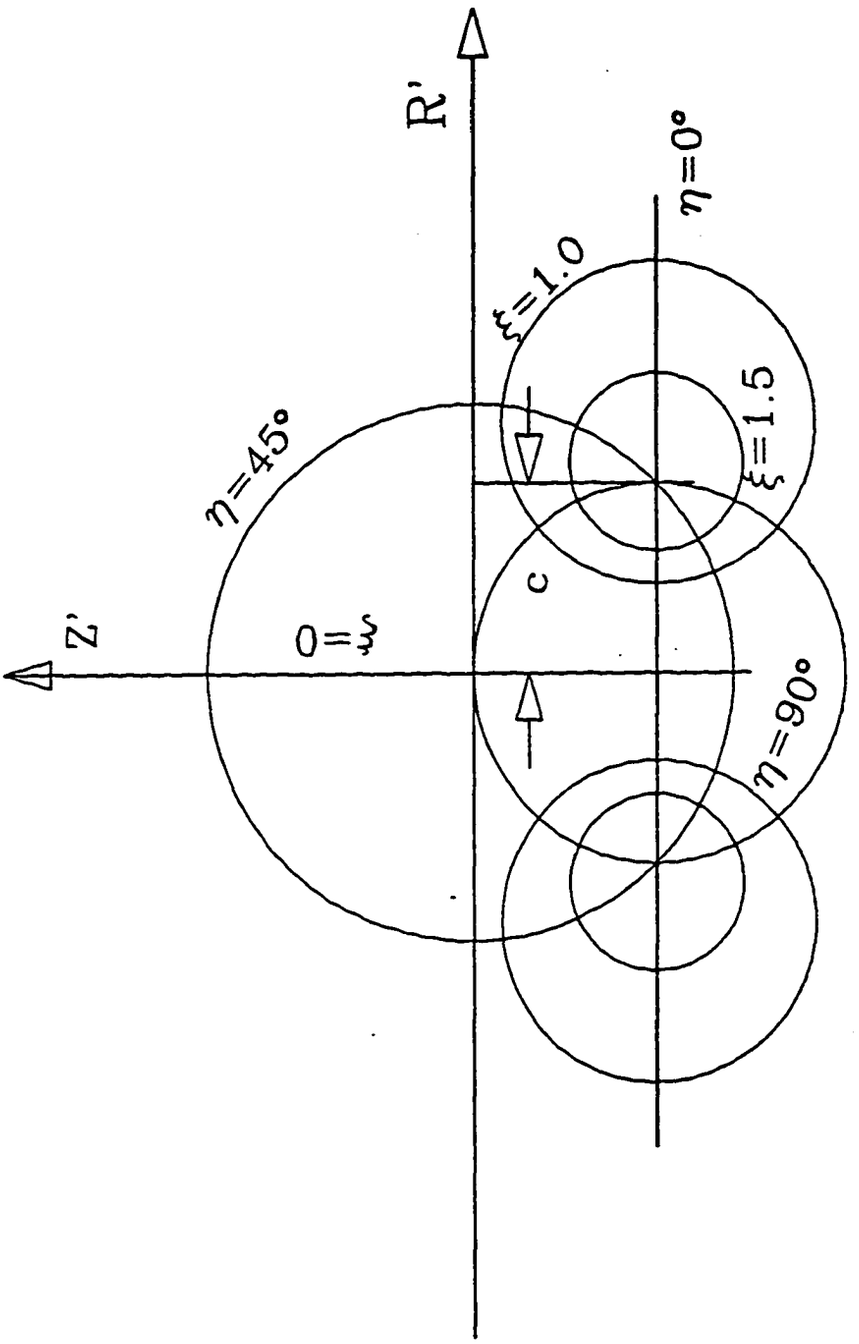

Figure IV.13 Toroidal Coordinates

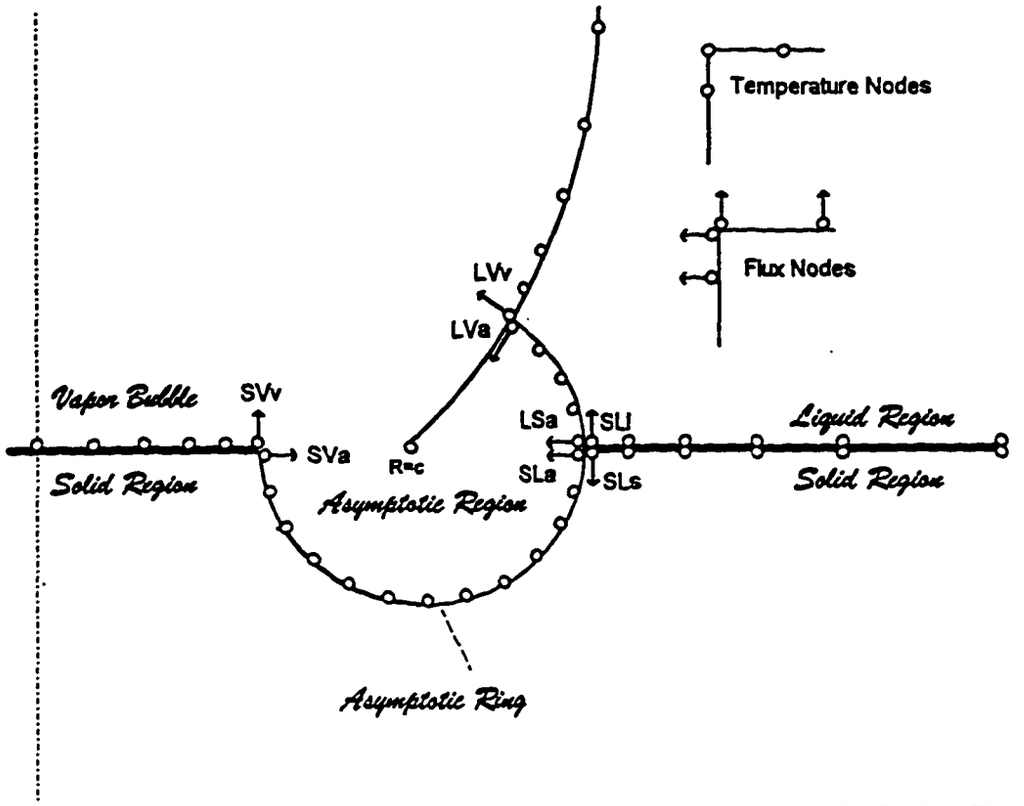

Figure IV.14a Mesh Generating Technique and Extra-Node for Flux

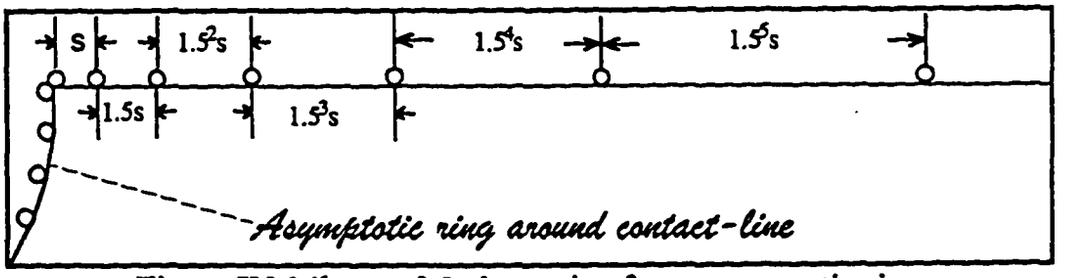

Figure IV.14b Mesh spacing from asymptotic ring

Figure IV.15 Conformal Mapping

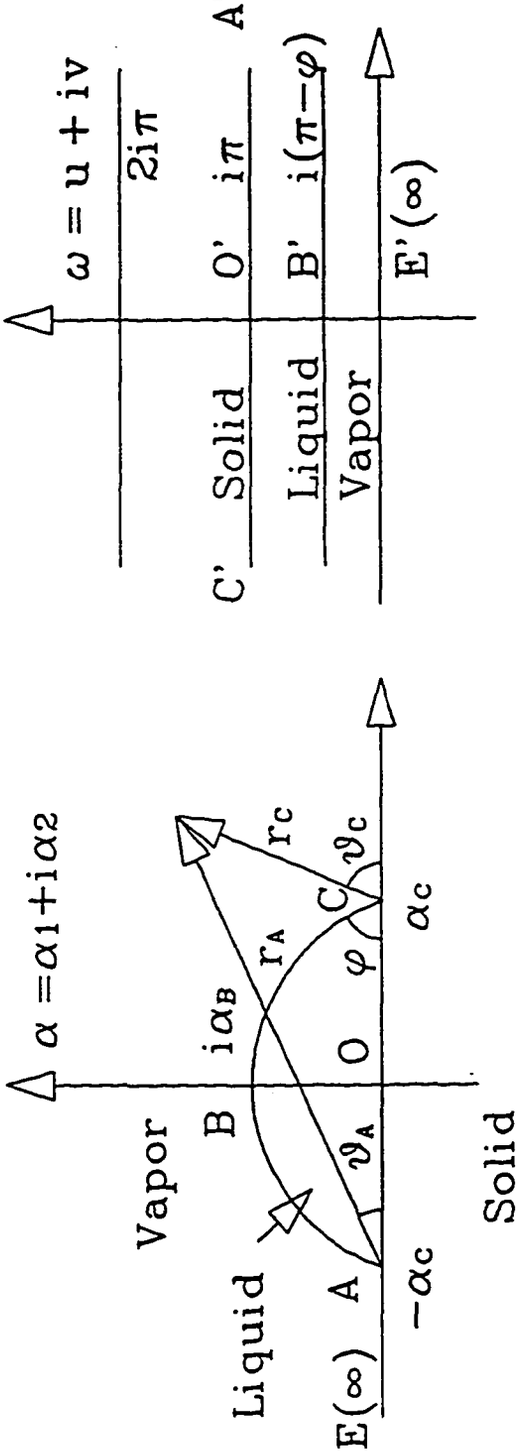

Chapter V

HEAT TRANSFER TO VAPOR BUBBLE GROWING SLOWLY INSIDE A COMPOSITE SOLID-LIQUID CELL

V.1 Introduction

In previous chapters, we have examined the static heat transfer to a spherical bubble in dimensionless form as a function of the system parameters. In this chapter, we will depart from that static point of view and use quasi-static method to follow a slowly growing embryonic vapor bubble from its incipience to millimeter size in dimensional form. The heat transfer problem associated with this growing bubble will reveal how the system variables regulate, how the bubble's growth scales with time and how the overall heat transfer scales with the system variables in the context of conduction-only transfer.

V.1.1 Saturation Temperature

Typically, vapor bubbles only form as pockets in small pits and scratches of the order of microns on an otherwise smooth solid-liquid interface (Clark, Strenge, and Westwater 1959). The pressures in these gaseous pockets are higher than the surrounding liquid pressure due to the tension of the vapor-liquid bubble surface. The Young-Laplace equation determines the pressure difference:

$$p_b' - p_\ell' = \begin{cases} \sigma\left(\dfrac{1}{r_b''} + \dfrac{1}{r_b'''}\right) & \text{nonspherical bubble} \\ \dfrac{2\sigma}{r_b'} & \text{spherical bubble} \end{cases}, \qquad (V.1)$$

where r_b'' and r_b''' are the two principal radii of curvature of a non spherical bubble, r_b' is the radius of a spherical bubble, and σ is the bubble's surface tension. Due to this elevated pressure, the saturation (equilibrium) temperature T_v' inside

the pocket is higher than the saturation temperature T'_{sat} of the surrounding liquid. Clausius-Clapeyron equation provides this dependence:

$$T'_v - T'_{sat} = \frac{T'_{sat}}{h_{fg}} \frac{p'_b - p'_\ell}{\rho_v}, \qquad (V.2)$$

where h_{fg} is the latent heat, ρ_v is the vapor density, and T'_{sat} is the saturation temperature of the liquid at pressure p_ℓ. Combining (V.1) and (V.2), the superheat required for the formation of bubbles should be

$$T'_v = T'_{sat} \begin{cases} \left(1 + \dfrac{\sigma}{\rho_v h_{fg}} \left(\dfrac{1}{r''_b} + \dfrac{1}{r'''_b}\right)\right) & \text{nonspherical bubble} \\ \left(1 + \dfrac{2\sigma}{\rho_v h_{fg} r'_b}\right) & \text{spherical bubble} \end{cases} . \qquad (V.3)$$

When the bubbles are on the order of microns in size and the surrounding temperature field is uniform, this superheat can be as high as several degrees, as verified by Griffith and Wallis (1960). If a solid plate is used as a heating surface, this superheat can be even higher. Generally speaking, for each bubble embryo, T'_v is a local criterion determined only by the bubble's local condition and its initial radius of curvature, assuming all other parameters are uniform throughout the domain. If the interior temperature of an embryo bubble is lower than its saturation temperature T'_v and there are no residual gases due to the impurity of the liquid, the bubble will collapse/condense even if its actual temperature is higher than the saturation temperature of the surrounding liquid T'_{sat}. The bubble will not grow until its saturation temperature T'_v is reached and there is a net evaporation into the bubble. As the bubble grows, its radius of curvature increases, the pressure inside the bubble drops (see V.1) and the corresponding saturation temperature T'_v decreases (see V.3). If the surrounding temperature is constant, the lowering of T'_v

increases driving force ($T-T_v'$) for heat transfer to the bubble and thus speeds up bubble growth. From then on, nucleation becomes a spontaneous process. As we will see, the assumptions discussed in the previous chapters are most well justified for this early stage of growth, when one can choose the temperature difference $\Delta T'$

$$\Delta T' := T_{sl}' - T_v' = \frac{(T_{sat}' - T_v')\kappa h' + (T_s' - T_v')H'}{\kappa h' + H'}, \qquad (V.4)$$

and therefore Re, Pe, Bo and Ca to be arbitrarily small. As such, the bubbles certainly remain spherical shape and the conduction dominates. However, as the bubble grows, the temperature of the bubble begins to fall, and the driving force for heat transfer increases. This makes one wonder if the previous assumptions remain valid for bubble growth. Since the smallness of these parameters determines the nature of the bubble's growth, it is important to use our results to calculate then a *postiori*, to see how they change with bubble growth and at which point the assumptions are no long valid.

V.1.2 Bubble Incipience

In homogenous bubble incipience, since the bubble is situated in a uniformly superheated liquid domain, evaporation occurs simultaneously over entire vapor-liquid interface. In the heterogeneous case, bubble incipience begins in irregularities on an otherwise smooth heating solid surface (Clark, Strenge, and Westwater 1959). Since the contents of the bubble are merely residual gases and hot vapor at this point, the temperature distribution on the embryonic bubble interface is not uniform initially. When the solid wall temperature T_s' increases, there is a point when the contact region of the bubble first reaches the saturation temperature T_v'. The liquid in this region then begins to evaporate, carrying latent heat away with it into the bubble. The vapor then condenses on cooler part of the bubble interfaces away from the solid, releasing heat to those regions. In other

words, the vapor from hotter contact region transports heat to the cooler part of the bubble by the evaporating from the contact region and then condensing to the regions away from the solid. This process eventually makes the bubble's interfacial temperature uniform. Obviously, the bubble grows only when there is a net evaporation, which requires that the overall temperature difference $\Delta T'$ (V.4) is greater than zero. As we have discussed in the previous section, once the bubble begins to grow, so does this temperature difference. One can always impose overall temperature gradients small enough so that growth starts arbitrarily slowly with arbitrarily small $\Delta T'$. With this small $\Delta T'$ at the earliest stage of the bubble growth, one can be sure that Re, Pe and Ca numbers are very small; so, one can always omit the convective terms. Since the Bond number only concerns the buoyancy and the surface tension, it remains small as long as the bubble is in the micron to sub millimeter range; thus the bubbles are all spherical or sections of sphere in this range. The analysis in Section II.2 still applies. In the following sections, we apply the same governing equations and boundary conditions and check a postiori at what point these small dimensionless group assumptions break down.

V.2 Formulation of the Bubble Growth Calculation

In this section, we formulate a method to calculate the quasi-static growth of a vapor bubble. In order to carry out the specific calculations we make a few specific, particular choices of conditions which we detail below. Other choices are possible, and our selection was for convenience.

Due to the fact that in the initial stage, the temperature difference $\Delta T'$ in (V.4) is arbitrarily small, the governing equations adopted in the previous chapters are valid. The governing equations for both the liquid and solid regions are:

$$\nabla^2 T'_{\pm} = 0 . \qquad (V.5)$$

The boundary conditions are: on the liquid free surface we choose the temperature to be the saturation temperature of the liquid at one atmospheric pressure. On the solid wall, the temperature is the prescribed:

$$\begin{cases} T'_{+} = T'_{sat} & \text{at} \quad Z' = H' - d' \\ T'_{-} = T'_{s} & \text{at} \quad Z' = -h' - d' \end{cases} \qquad \text{(V.6)}$$

On the liquid-solid interface, the temperature and heat flux are continuous,

$$\kappa_\ell \nabla T_{+} \cdot \vec{n} = \kappa_s \nabla T_{-} \cdot \vec{n} \quad \text{and} \quad T_{+} = T_{-} \quad \text{at} \quad Z' = -d', \qquad \text{(V.7)}$$

where $\vec{n}$ is a unit normal vector perpendicular to the solid-liquid interface, and the liquid-vapor interface of the bubble is at the uniform saturation temperature T'_v, i.e.,

$$T'_{+} = T'_{v} = T'_{sat}\left(1 + \frac{2\sigma}{\rho_v h_{fg} r'_b}\right) \quad \text{at liquid-vapor interface and } Z' \geq -d'. \qquad \text{(V.8)}$$

If the bubble is attached to the solid interface with a contact angle φ, there will be a solid-vapor interface as well. In this case, the temperatures and heat fluxes should also be continuous. However, since we assume that $\rho_v << \rho_\ell$, $\kappa_v << \kappa_\ell$, these conditions simply reduce to a single, insulating boundary condition, i.e.,

$$\frac{\partial T_{+}}{\partial Z'} = 0 \quad \text{at} \quad Z' = -d', \quad \text{for} \quad 0 \leq R' \leq \sin\varphi \qquad \text{(V.9)}$$

For finite cell configurations, periodicity requires the radial flux on the lateral cell boundary to be zero, or

$$\frac{\partial T_{\pm}}{\partial R'} = 0 \quad \text{at} \quad R' = R'_c. \qquad \text{(V.10)}$$

To follow a growing bubble, we need a kinematic-evaporative boundary condition to calculate the moving vapor-liquid interface. For phase-change problems such as evaporation and condensation, the location and the possible motion of the interface must be determined together with the velocity and the temperature field in the two phases. A formulation of the interfacial condition is given by Vedat S. Arpaci (1984) as $\rho_1\left(v_1 - \frac{dN}{dt}\right)h_{12} = -\kappa_1\left(\frac{\partial T_1}{\partial n}\right)_s + \kappa_2\left(\frac{\partial T_2}{\partial n}\right)_s$, where N is the position of the interface, n is the direction normal to the interface pointing to phase 2, v is the velocity normal to the interface, T is the temperature, the subscripts 1 and 2 denote two different phases and h is the latent heat. In our case, 1 is the vapor and 2 is the liquid, and the normal vector points into the vapor instead of the liquid. Since we further assume that the vapor is isothermal due to its negligible conductivity and heat capacity, we finally obtain

$$\rho_v h_{fg}\frac{dn}{dt} = \kappa_\ell \frac{dT'}{dn}, \qquad \text{(V.11)}$$

where n is the vector normal to the interface pointing into the vapor. Equation (V.11) is a prescription for advancing the bubble interface locally. However, surface tension and, in general, the normal viscous stresses in the liquid also contribute to determine the interface's shape. As such, this evaporation-driven motion would set up a distribution of normal stresses in the liquid at the interface, which would be a boundary condition on the fluid mechanics. However, since our case is one of large capillary forces (Ca, Bo << 1), surface tension alone determines the interfacial shape to be sphere or a section thereof (if Bo >> 1, then the shape would be the balance between surface tension and gravity given by the Young-Laplace Equation). Thus given a prescription for the motion of the contact line and the new volume, surface tension, rather than Equation (V.11) determines

the new shape. Thus, in our case, Equation (V.11) enters only in an integral sense in order to determine the volume change per unit time, i.e.,

$$\frac{1}{\rho_v h_{fg}} \int_{\Omega_{bubble}} \kappa_\ell \frac{dT'}{dn} dA = \frac{dV'}{dt} \qquad \text{(V.12)}$$

where V' is the volume of the bubble. One must still model the motion of the contact line. One choice is to use Equation (V.11) locally where the major heat transfer occurs. For numerical convenience, however, in the contact line region, the present calculation makes the simpler choice of requiring geometric similarity of the bubble throughout its growth. That is, we assume that as the bubble grows, it not only remains spherical (see above), but it also maintains its scaled position relative to the solid. If the bubble is detached, then we keep the dimensionless gap $\delta = (d' - r_b')/2r_b'$ fixed as it grows. If it is attached, then we fix the contact angle φ throughout the growth of the bubble under investigation.

The situation under consideration is an embryonic water bubble initially of several microns (the size of surface irregularities) in radius that grows to 1 mm in a composite cell of a 5 mm thick layer of liquid over a 5 mm thick solid ($H' = h' = 5$mm). The pressure is atmospheric. Thus, the liquid free surface temperature is $T'_{sat} = 373°K$, the gravitational acceleration is $g = 9.807$ m/s^2. The properties of the water are: vapor density $\rho_v = 0.60$ kg/m^3; liquid density $\rho_\ell = 958$ kg/m^3; latent heat $h_{fg} = 2257$ kJ/kg; liquid heat capacity $c_\ell = 4.184$ J/kg/°K; liquid kinematic viscosity $\nu_\ell = 0.2818\times10^{-6}$ m^2/sec; water-steam surface tension $\sigma = 0.0589$ kg/s^2; liquid diffusivity $\alpha_\ell = 0.168 \times 10^{-6}$ m^2/s and conductivity $\kappa_\ell = 0.680$ J/m/°K/s. With the above parameters are fixed, we shall vary the cell radius R'_c, solid conductivity κ_s, and bubble positions d' or φ.

V.3 Numerical Procedures

Below we describe the technique used in the calculations of bubble growth. In order to minimize CPU time consumption and maintain adequate accuracy, we first divide the whole calculation regime into two distinct regimes, one with small bubbles and the other with big bubbles.

Small Bubbles - The bubble is very small comparing with the cell, i.e., $r'_b \leq R'/20$. From the results of the previous chapters, we have noticed that when the ratio $R'_c/a' = 20$, the calculated results are very close to those of the collocation cases. As long as the liquid layer is not too thin, the maximum error is less than one percent (refer to Figures III.2(a), IV.1 and IV.2, where the results approach those of the collocation calculations rapidly even as R_c, $H \rightarrow 10$ only). So, instead of doing a separate calculation for each growth step when the bubble is small compared to the distance to the neighboring bubble, we construct a geometrically similar, i.e., φ or δ, standard cell of radius $20r'_b$, where both thickness of liquid and solid layers are $20r'_b H'/R'_c$ scaled in a manner outlined below, and use its results, for all of the early stage growth.

When the bubble is small, it occupies a negligible fraction of the solid-liquid interface. Thus far from the bubble, i.e., for $20\, r'_b \leq R' \leq R'_c$, $-H' - d' \leq Z' \leq -20\, r'_b - d'$, and $20\, r'_b - d' \leq Z' \leq H' - d'$, the system does not notice its presence. Thus, the temperature distribution there is linear, just as it would be in the bubble-free situation. Consequently, along the upper and lower boundaries of the standard cell, we use this profile to prescribe the temperatures as

$$\begin{cases} T'_{+} = \left(-\dfrac{(T'_s - T'_{sat})}{1+\kappa} + T'_v \right) \dfrac{20r'_b}{R'_c} + \dfrac{kT'_{sat} + T'_s}{1+\kappa}, & \text{at } Z' = 20r_b\text{'- d'} \\ T'_{-} = \left(\dfrac{(T'_s - T'_{sat})\kappa}{1+\kappa} + T'_v \right) \dfrac{20r'_b}{R'_c} + \dfrac{kT'_{sat} + T'_s}{1+\kappa}, & \text{at } Z' = -20r_b\text{'- d'} \end{cases}, \qquad \text{(V.13)}$$

where as at radial distances beyond $20\,r'_b$, the temperature profile is one dimensional, i.e., a function only of Z:

$$\frac{\partial T'_{+}}{\partial R'} = 0, \qquad \text{at } R' = 20\,r'_b. \qquad \text{(V.14)}$$

Finally, from the actual bubble radius, we can determine the bubble saturation temperature T'_v by using Equation (V.3).

By utilizing the superposition principle described in Equation (III.13), we need only solve the dimensionless standard cell problem twice and simply appropriately redimensionalize at each step, in order to find all of the solutions for the actual cell during its growth from bubble incipiency until $r'_b = R'/20$. The solutions are,

$$T'_{\pm} = \left[T^1_{\pm}(R'/r'_b, Z'/r'_b)(T'_{sat} - T'_v) + T^0_{\pm}(R'/r'_b, Z'/r'_b)(T'_s - T'_{sat}) \right] + T'_v; \quad \text{(V.15)}$$

for the standard cell where $R' \le 20\,r'_b$, $-20r'_b\text{-}d' \le Z' \le 20r'_b\text{-}d'$, and

$$\begin{cases} T'_{+} = (T'_{sat} - T'_{s\ell})(Z'+d')/H' + T'_{s\ell} \\ T'_{-} = (T'_{s\ell} - T'_s)(Z'+d')/H' + T'_{s\ell} \end{cases}, \qquad \text{(V.16)}$$

for the region beyond the standard cell. The solutions $T^1_{\pm}(R'/r'_b, Z'/r'_b)$ and $T^0_{\pm}(R'/r'_b, Z'/r'_b)$ are non-dimensional solutions of (II.0) through (II.5), with $H = h = 20H'/R'_c$, $R = 20$, $T_s = 1$, and $T_f = 1$ or 0, respectively. The advantage of this method is, for the entire growth period when the bubble is small, we need only calculate two basic non-dimensional solutions $T^1_{\pm}(R'/r'_b, Z'/r'_b)$, $T^0_{\pm}(R'/r'_b, Z'/r'_b)$

and construct the solution at each time using $T_{\pm}^{1}(R'/r_b', Z'/r_b')$, $T_{\pm}^{0}(R'/r_b', Z'/r_b')$ via (V.15) and (V.16).

Large Bubbles - In the second section, the bubble is comparable in size to the cell, e.g., $r'_b \geq R'/20$. In this case, we have to solve equation (V.5) - (V.10) with r'_b that changes at each time step. Instead of calculating all possible r'_b's when the bubble is growing, we choose 50 different r'_b's evenly distributed between $R'/20 \leq r'_b \leq 1$ mm, and solve for the solutions accordingly. In the later calculations, we simply use these 50 different solutions and linear interpolation to approximate solutions for any given r'_b.

Time Steps - Since the number and size of the time steps necessary for a given accuracy depends on the system parameters, they are difficult to predict a priori. Instead, we choose the size of each time step by fixing the maximum run allowable fractional change in bubble size in a single step. We set this value arbitrarily at $\Delta r_b/r_b = 0.28\%$. This leads to 1983 total steps. For several typical cases, we decreased this fractional change by half to redo the calculations. The comparison showed an overall error less than one percent for the bubbles growing from 4 microns to 1 mm.

V.4 Results

V.4.1 Dimensionless Groups

Capillary Number is Small - We have carefully followed the behavior of Capillary number. Figure V.1 shows the Ca number of a growing bubble under various conditions with an initial radius of 50μm. The results have shown that Ca is always small in the cases under investigation due to the small viscosity of water. Since Ca and Bond numbers are small, the bubble is simply spherical when it is sub-millimeter in size. However, the Ca number may become significantly larger

when the initial radius of the bubble is very small, The higher ΔT associated with a sufficiently small initial bubble radius has the potential to induce explosive evaporation and extremely fast expansion and thus to render the surface tension forces no longer dominant. When that happens, the shape of the bubble is a dynamic one determined by the interaction with the liquid flow, even if the equilibrium assumption for the interface is still valid at every instant. However, as we shall discuss in the context of Re and Pe, local considerations bear out the relevance of our calculations even in these cases.

Global Reynolds Number is Big - As detailed in the previous chapters, our calculations are based on the Reynolds and Peclet numbers being small. These assumptions are obviously valid if we choose the temperature difference (V.4) arbitrarily small:

$$Re = \frac{a'\dot{a}'}{\nu_\ell} \cong \frac{\kappa_\ell \Delta T'}{\nu_\ell \rho_v h_{fg}} \cong \frac{0.68 \times \Delta T'}{0.2818 \times 10^{-6} \times 0.60 \times 2.257 \times 10^6} = 1.8 \times \Delta T' \text{ ,(V.17)}$$

$$Pe = \frac{a'\dot{a}'}{\alpha_\ell} = Re\frac{\nu_\ell}{\alpha_\ell} = RePr_\ell \cong \frac{Re \times 0.2818 \times 10^{-6}}{0.1684 \times 10^{-6}} = 3.03 \times \Delta T' . \qquad \text{(V.18)}$$

As we can see from the definitions, the Peclet number *Pe* is nothing more than the Reynolds number *Re* multiplied by a Prandtl number, *Pr*, a constant of order one. Thus we focus only on *Re*.

As we have discussed in Section V.2, once the bubble starts to grow at fixed wall temperature, the temperature difference (V.4) tends to increase, and this may increase Re and Pe beyond values for which our calculations are valid. This is a particular danger when the bubble starts with a very small radius and is attached to a highly conducting solid. Figures V.2 and V.3 show the calculated $R_e := \dot{r}_b r_b / \nu_\ell$, in various cases. The conductivity ratios are $\kappa = 0.1$, and $\kappa = 0.001$;

the bubble positions are $\delta = 0.1$, $\delta = 0.01$, $\delta = 0.001$, or contact angles $\varphi = 30°$, $\varphi = 90°$, $\varphi = 120°$ (Table V.1 collectively lists all of the legends for these two figures and any subsequent figures). The bubble's initial radii are, $R_0 = 50\mu m$, $R_0 = 100\mu m$, and $R_0 = 150\mu m$, respectively. The initial condition is set up so that at the halfway between the bubble apex and the try spot, the linear temperature distribution is exactly T_v, so the equation (V.4) is very close to zero. Obviously, all of the cases begin with a very small Reynolds number. However, after the onset of evaporation, the Reynolds numbers increase very rapidly as predicted, especially for the attached bubbles with highly conducting solid and small initial radii. Generally speaking, the Reynolds number, once the evaporation starts, varies from very small, e.g., $Re = O(0.01)$, to very large, e.g., $Re = O(1000)$, indicating the bubble growth is a very complex phenomenon encompassing the whole range of liquid flow regimes. At the first glance it seems, that the small Reynolds number (and small Peclet) assumptions are violated in the boiling heat transfer when the bubble is attached or when a detached bubble begins with a radius that is too small, the only exception for attached bubble during the extremely short period when bubbles just begin to grow and where *Re* and *Pe* are truly small. Upon closer examination, though, one sees a different picture.

Local Reynolds Number is Small for Attached Bubbles - Consider the heat absorbed by a bubble as the function of circumferencial position s (Figures V.4 and V.5) measured from the contact line (attached) / central line (detached). Strikingly, when the bubble is attached, almost all of the heat transfer occurs within the contact region, i.e., within the order of $s = O(10^{-3})$ to $s = O(10^{-1})$. And, this trend becomes more extreme as the solid becomes relatively higher conducting, precisely the situation that calls the small Re, Pe assumptions in question. In Figure V.4 (κ=0.1), 40% to 90% of the total heat transfer to the attached bubble takes place by $s = 0.1$; in Figure V.5 (κ=0.001), 80%-90% of the total heat transfer occurs by

s = 0.001! This trend is even more apparent when we plot Figures V.6 and V.7 in semilog coordinates (see Figures V.6. and V.7). Obviously, the bubble radius $\dot{r}_b$ is not the characteristic length scale for heat transfer to an attached bubble. The more appropriate Peclet and Reynolds numbers for contact region heat transfer are $R_e = \dot{r}_b r_b s^2/\nu_\ell$ and $Pe = \dot{r}_b r_b s^2/\alpha_\ell$ where $r_b s$ is the distance measured from the contact line (attached). Figure V.8 shows the adjusted, local Reynolds number as the function of bubble radius. Table V.2 lists all of the data, i.e., s and the fractional heat transfer up to s, used in this local calculation. Generally, more than 90% of the total heat transfer towards the bubble takes place within a region of equivalent to at most only 5 percent of the bubble radius when the solid is very conducting. Thus, the prevailing mechanism of heat transfer enhancement for attached bubbles and for sufficiently large detached bubbles, as vividly demonstrated in Table V.2, is conduction. This result contradicts the universal dogma that characterizes boiling heat transfer theories.

Spherical Bubble Growth and Multitude Fluid Flow Regions - From what we have discussed so far, we may have concluded that multiple fluid flow zones and a spherical shape characterize the sub-millimeter vapor bubble growth problem. Globally the bubble growth is a potential flow problem, where the viscous and diffusive time is much longer than the growth time. So, the fluid is effectively inviscid and non-conducting. However, when the bubble is attached to a conducting solid, the dramatic heat transfer associated with the onset of nucleate boiling occurs within the contact region where the local Re number is extremely small. Thus heat transfer incipient boiling is predominantly a conduction problem.

V.4.2 Growing Bubbles:

Growth Time as a Function of Superheat - Let the initial radius of the bubbles be determined by requiring Equation (V.4) to be zero, that is,

$$r_0 = \frac{2T_{sat}\sigma(1+\kappa)}{\rho_v h_{fg}(T_w - T_{sat})}. \qquad (V.19)$$

Define the growth time as the time needed for the bubble to grow from incipience to one millimeter in radius. Since the conduction problem is linear, the initial volume for the embryonic bubble is negligibly small, and Equation (V.12) defines the total heat consumed by the bubble and its resulting volume. One expects the growth time to go as the reciprocal of the superheat, e.g., $t_{growth} \propto (T_w - T_{sat})^{-1}$, with the coefficient depending on the bubble density, conductivity and contact angle. Figures V.9 shows this growth time in seconds as the function of wall superheat, T_w - T_{sat}, in degrees of Kelvin. The growth time decreases linearly with slope -1 on a log-log plot as the wall superheat increases for all values of the other parameters. Changes in these other parameters can shorten the growth time by an order of magnitude if the bubble is attached, the contact angle is larger, and the solid is more conducting. Similar trends hold for detached bubbles, although the heat transfer enhancement deriving from solid properties diminishes quickly.

From the differences between Figure V.9(a), a very low bubble density of about 3,200 per square meter, and Figure V.9(b), 203,000 bubbles over the same area, bubble density also impacts bubble growth strongly. When there are many competing bubbles nearby, the heat transfer rates to an individual bubble declines (it's growth time increases), while the overall heat transfer is greatly enhanced. We shall examine the dependence of the enhancement on bubble density below.

The Dependence of the Global Reynolds and Capillary Numbers on Wall Superheat: - Figures V.10 and V.11 show how the global Reynolds and Capillary numbers increase with increasing wall superheat, at large contact angle and high solid conductivities. Fortunately, as discussed above, precisely the conditions that

cause these numbers to be the highest, large contact angles and high solid conductivities, are the ones that concentrate the heat flux in an even smaller contact region where the characteristic length is much smaller. The appropriate local Reynolds and Capillary numbers are thus truly small. It is interesting to notice that, there is no significant difference in these dimensionless number effects between the two extreme cases of bubble densities, especially with highly conducting solids and large contact angles, as Figures V.10(a) and V.10(a) or Figures V.11(a) and V.11(a) show. Figures V.12 and V.13 show the two worst cases of these numbers, with larger contact angle and a highly conducting solid when the wall superheat is 10°C. It is interesting to see that the Reynolds number grows as the bubble grows, while the Capillary number vanishes all the way down to 0.01 when it approaches to millimeter size. Not surprisingly, all of the bubbles in this range are nearly spherical to a naked eye.

Heat Transfer Enhancement - Figures V.14 plots the heat flux with the bubbles divided by that in the bubble-free case under otherwise identical circumstances. In particular, we keep the bubble density fixed and explicitly exclude the dependence of bubble density on ΔT. Since both numerator and denominator are linear in ΔT, it is no surprise that the curves are flat. The familiar enhancement factors, such as conducting solid and large contact angles are at play here. Thus the enhancement is nearly independent of wall superheat at fixed bubble frequency. However, the bubble density dependence is dramatic. Figures V.14(a) and V.14(b) illustrate an enhancement of as much as a factor of 250 at high densities but only of 5 at low bubble density. The effects of bubble density under different wall superheats are illustrated in Figure V.15.

Evaporation Rate: Bubble Size vs. Time - Figure V.16 depicts one of the evaporation curves. From this log-log curve, one can see two clear growth regimes, each of which exhibits power law growth. The early regime concerns only

the infancy period where T_v varies with r at when the bubbles are too small to interact with each other. The second regime begins as T_v becomes independent of r, and continues into the regime when the bubbles interact with each other. Needless to say, the major heat transfer is in this second regime. One can correlate this second regime with great accuracy by

$$\sqrt[3]{V} \propto \sqrt{t} \times t^{-1.3\times10^{-7}N} \begin{cases} 1 & \text{attached} \\ t^{-(4.28\times10^{-5}N+0.07)\delta} & \text{detached} \end{cases}, \qquad \text{(V.20)}$$

where N is the bubble density - the number of bubbles per square meter and δ is the dimensionless gap $\delta = (d' - r_b')/2r_b'$. Clearly, except for a very small bubble-density dependent correction, the bubble radius scales as $R \propto \sqrt{t}$, which is what one would expect for a diffusion process. The correction factor follows the general trend that the more the bubble in a given area, the slower an individual bubble will grow due to the competing bubbles near by.

V.4.3 Reconstruction of the Typical Boiling Curve

Although since the 1930's, there have been numerous studies, both experimental and theoretical of pool boiling. The typical boiling curve, as illustrated in Figure I.1 taken from Lienhard (1989), appears to be, qualitatively, universal. As such, it is incumbent upon us to see how our theory compares with the universal features of this boiling curve. Are our results reasonable enough to shed some lights on this phenomenon, which is so profound that it still defies a satisfactory explanation.

First, our theory deals with single bubbles and interacting amongst individual bubbles. Thus, it is only reasonable to compare it with the region to the left of jets and columns. Our model also does not account for solid surface finishing, fluid flow and many others. Thus we need to input an empirical

relationship between N and ΔT. We begin by examining the first and most used correlation for nucleate boiling which is due to Rohsenow (1952):

$$\frac{c_p(T_w - T_{sat})}{h_{fg}P_r^s} = C_{sf}\sqrt{\frac{q}{\mu h_{fg}}\sqrt{\frac{\sigma}{g(\rho_\ell - \rho_v)}}} \qquad (V.21)$$

Here C_{sf} and s are the surface correction factors, c_p is the specific heat of water, μ is liquid viscosity and q is the flux per unit area. In our model, since the governing equations and the boundary conditions are all linear, the heat flux is proportional to the wall superheat, and the flux is per cell, e.g.,

$$q = q\big|_{\text{whole surface}} = NQ' \propto N\kappa_s \frac{(T_w - T_{sat})}{2H}, \qquad (V.22)$$

which leads to

$$q \propto N(T_w - T_{sat}). \qquad (V.23)$$

Plugging Equation V.23 into Equation V.21, one has,

$$\frac{c_p(T_w - T_{sat})}{h_{fg}P_r^s} \propto C_{sf}\sqrt{\frac{N(T_w - T_{sat})}{\mu h_{fg}}\sqrt{\frac{\sigma}{g(\rho_\ell - \rho_v)}}} \qquad (V.24)$$

Collection of all of the constants leads to

$$(T_w - T_{sat})^2 \propto N. \qquad (V.25)$$

There is still an unknown constant in Equation (V.25). Thus, we match our calculated heat flux with the experimental value from Lienhard's at a wall superheat corresponding to the rightmost edge of the single-bubble regime. In this manner, Figure V.17 compares our calculation with the typical boiling curve of Figure I.1, with all of the same scalings. In this Figure V.17, two curves with

contact angle φ = 120°C and 30°C, κ = 0.001 are the most interesting ones. It is gratifying to note that these calculated results, at two fairly extreme values of φ, bracket the experimental results.

Comparison With Experimental Correlations: - The final test of our theory in the context of comparison with experiments is to see how it fairs relative to the multifarious experimental correlations available in the literature. These correlations tend to take the form $q \propto (T_w - T_{sat})^{\alpha} N^{\beta}$ (see Table V.3). It is worth noting the great variability in the published correlations despite the fact that they purport to account for the same phenomena in overlapping or identical regimes. Clearly the scatter in the data upon which these correlations are based is striking. Nevertheless, they represent the practice in this area. Table V.3 demonstrates that our theory yield exponents that are well within the range of phenomenologically determined values. Thus, our theory is consistent with the design correlations that have been the basis of boiling heat transfer predictions in practice for over a half a century.

Table V.1 Universal Legend System Adopted in Chapter V								
φ=120°	φ=90°	φ=30°	δ=0.001	δ=0.01	δ=0.1	δ=1	κ=0.001	κ=0.1
o	+	Δ	×	□	◆	◊	———	- - - -

Table V.2 Chart for Calculating Local Reynolds Number						
Conductivity	κ = 0.1			κ = 0.001		
Contact Angle	30°	90°	120°	30°	90°	120°
Radius	s = 0.3	s = 0.1	s = 0.05	s = 0.05	s = 0.03	s = 0.01
Heat Transfer	55%	75%	85%	90%	95%	95%

Table V.3 Comparison of Literature and This Work For Coefficients of $q \propto \sim (T_w - T_{sat})^{\alpha} N^{\beta}$			
Author	α	β	Comments
Jakob	1		
Westwater	0.73		
Gaetner	2/3		
Kirtby and Westwater	1/2		
Orell	1/2	1	Normal
Gaetner and Westwater	0.47		
Danilova	4/9		Freon 113
Danilova	1/3		Water
Rohsenow	1/3	1~4/3	$N \sim (T_w - T_{sat})^2$
Yamagata	1/3	1,2	
This Work: Huang *et al*	0.894	1	Attached, κ=0.001
This Work: Huang *et al*	0.443	1	Attached, κ=0.1

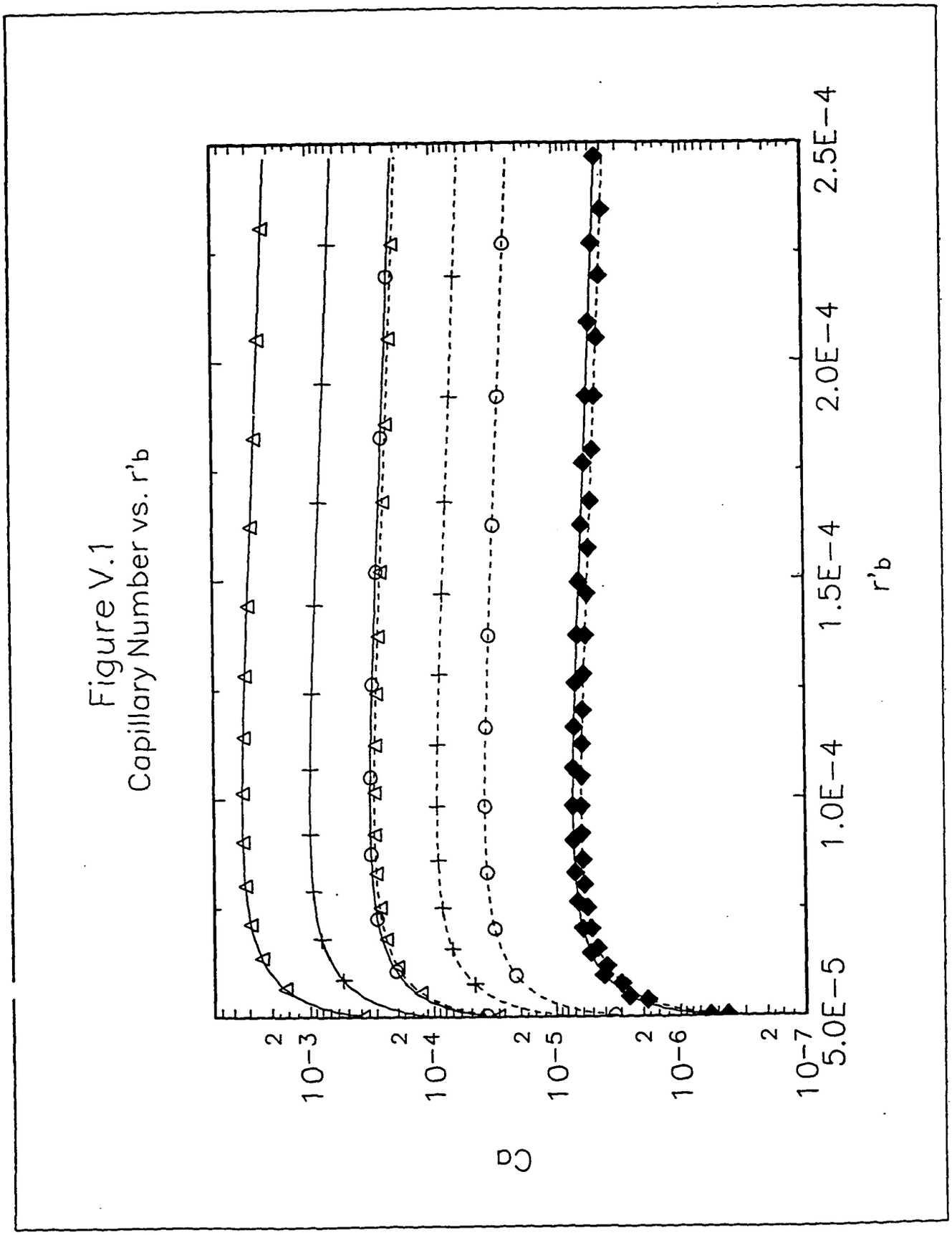

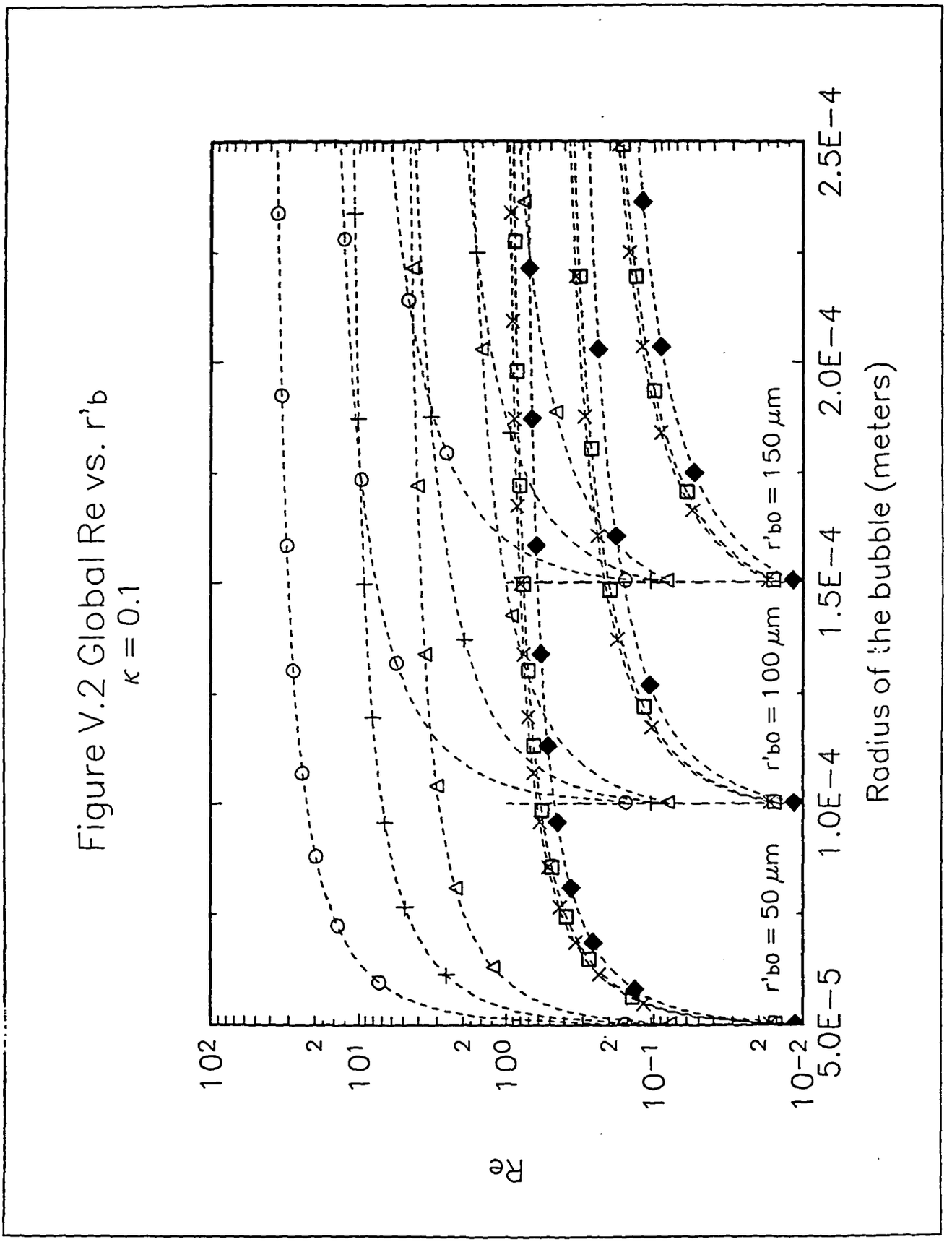

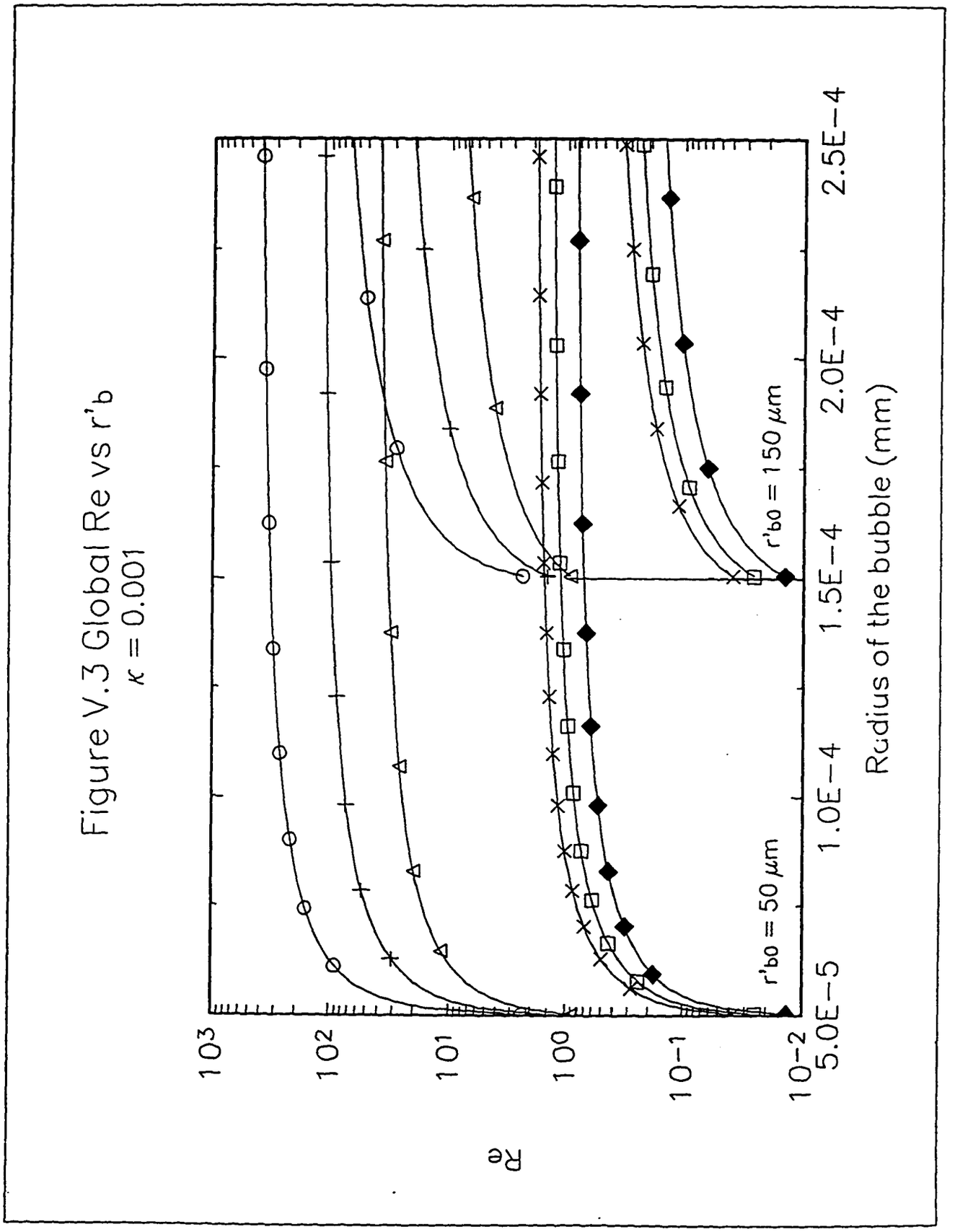

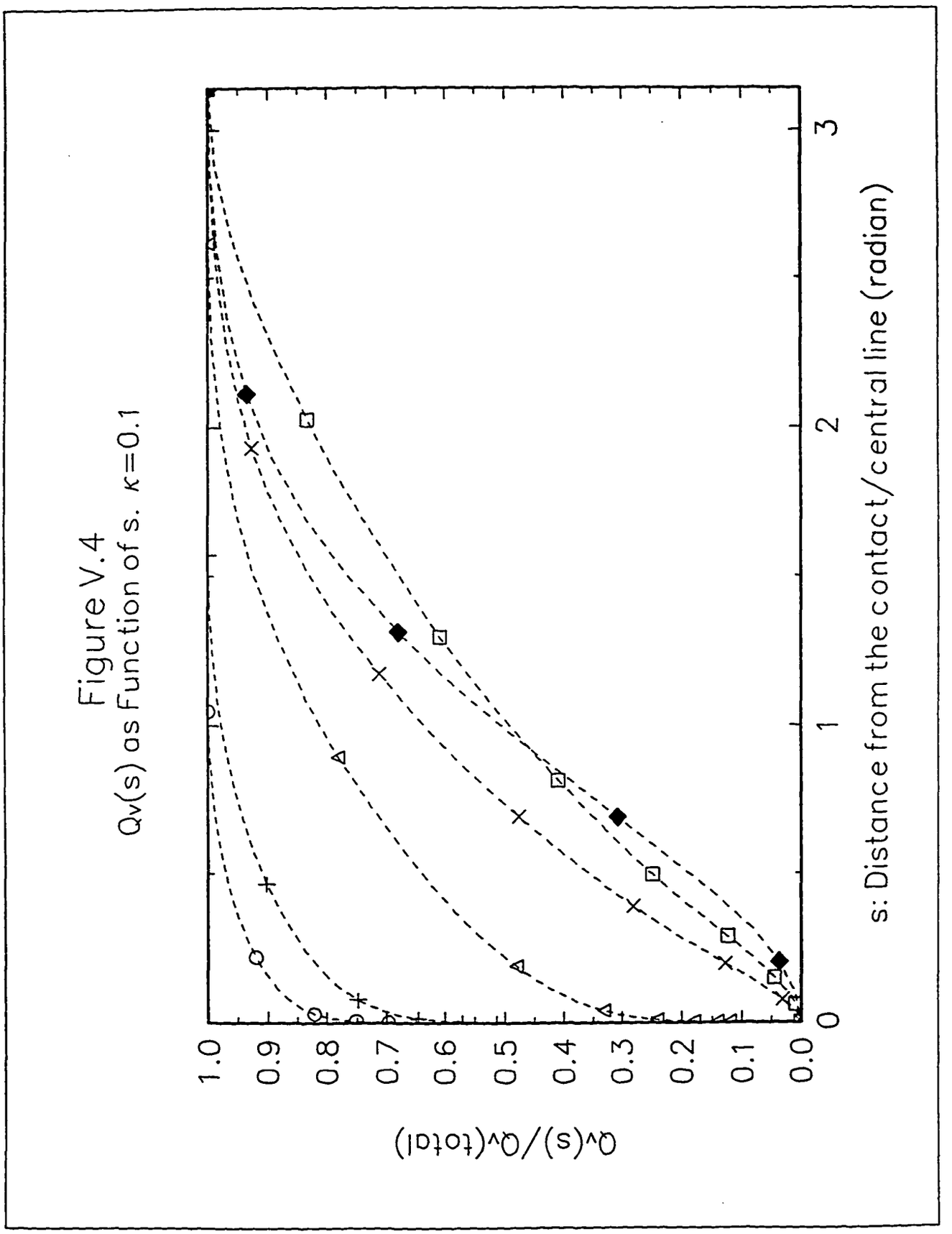

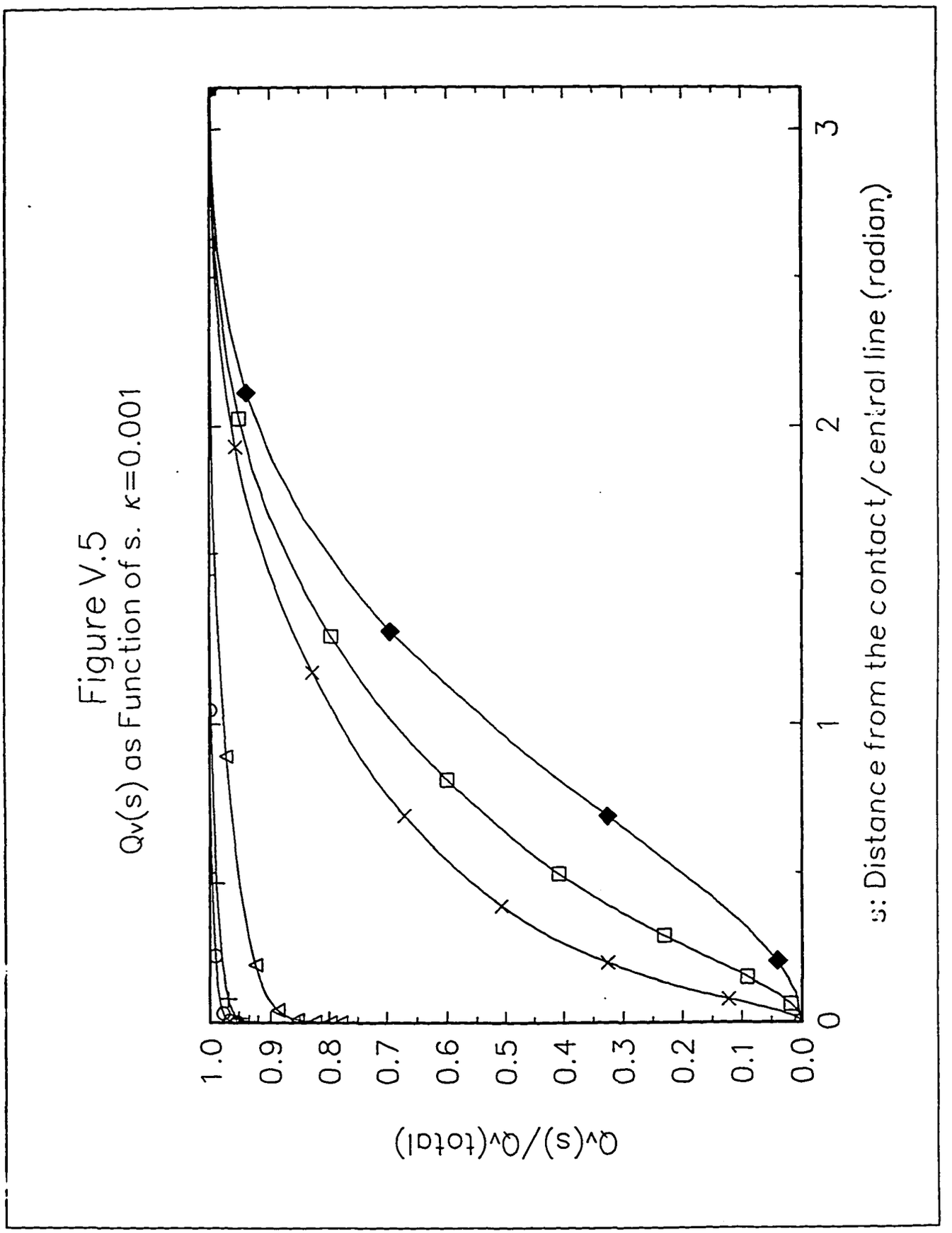

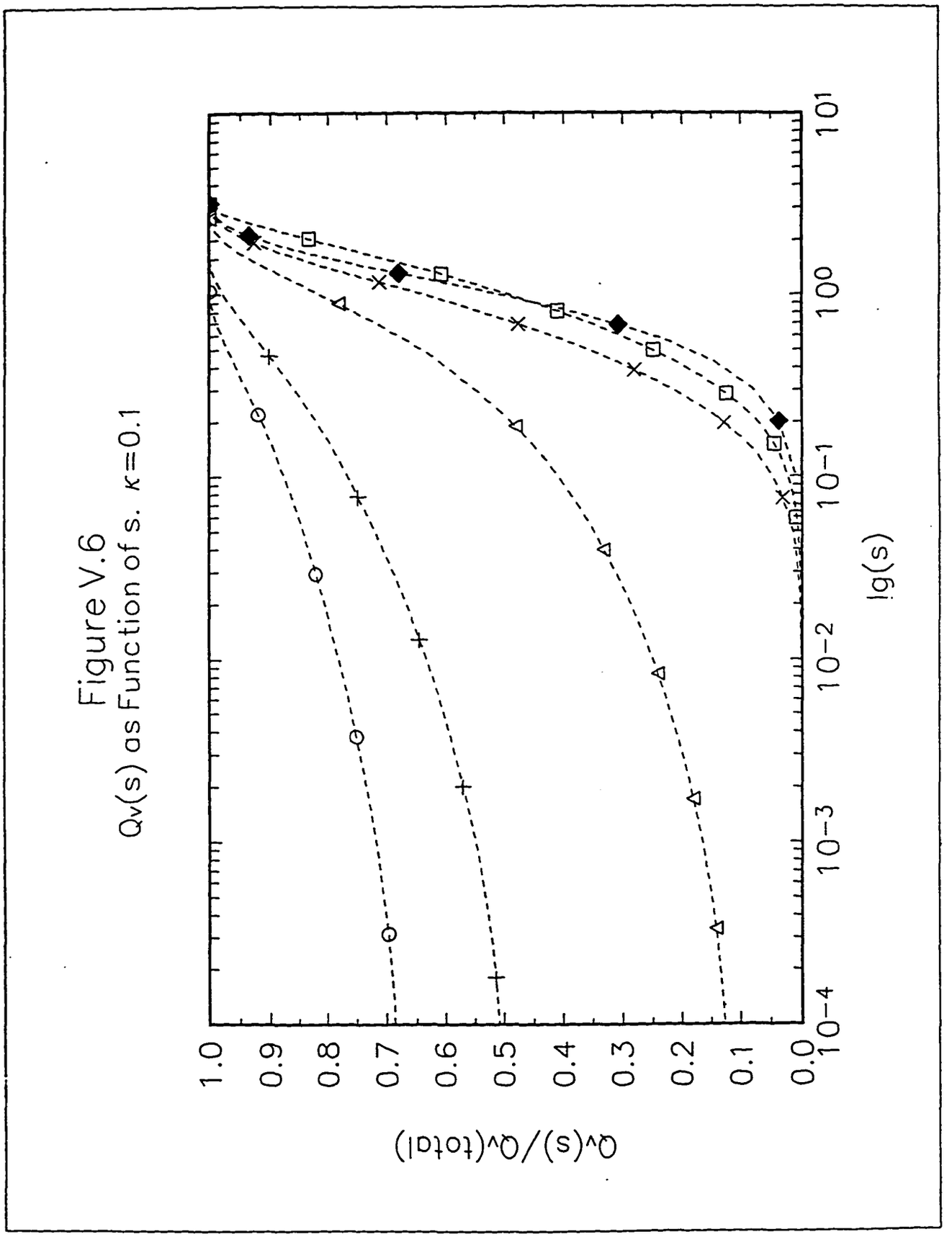

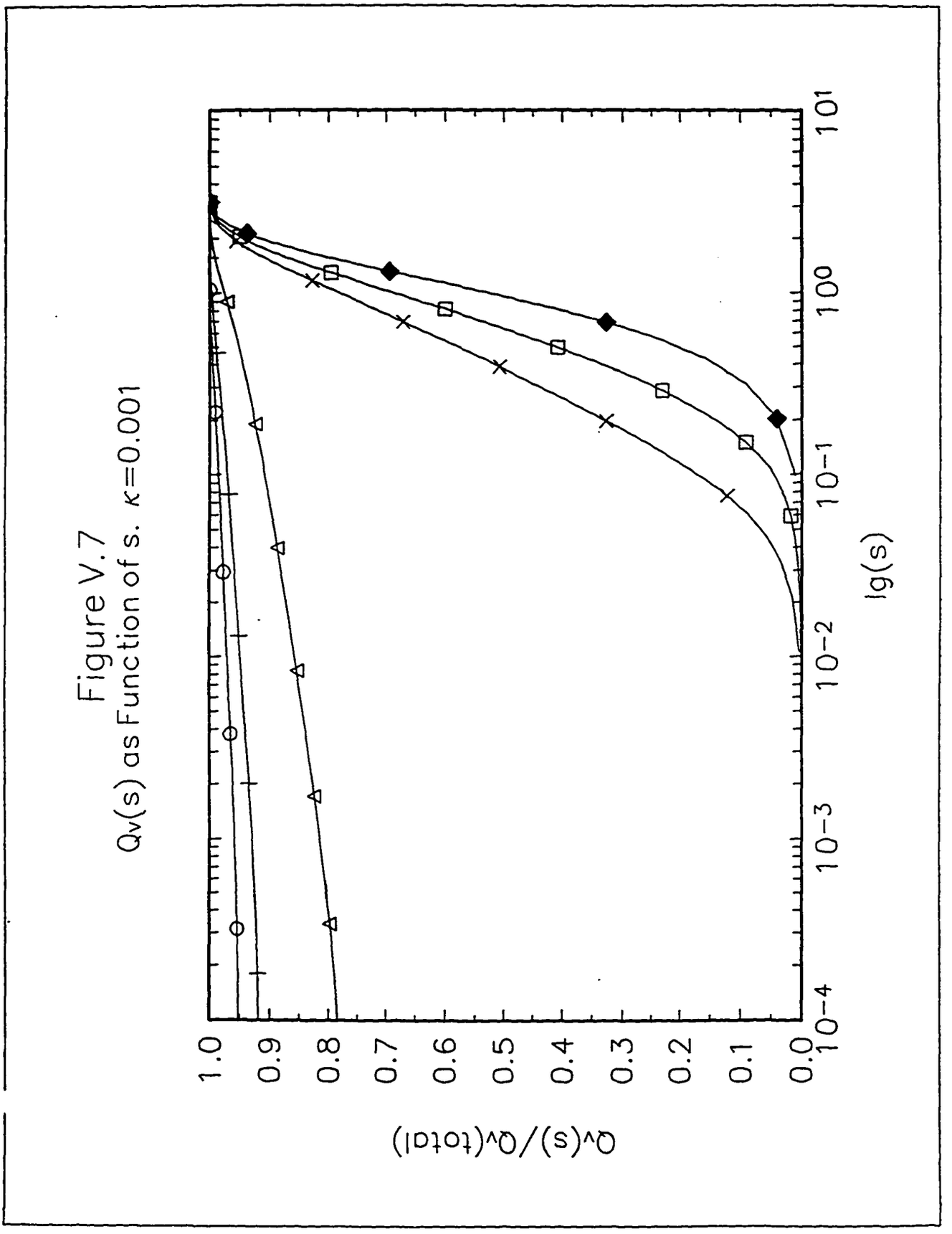

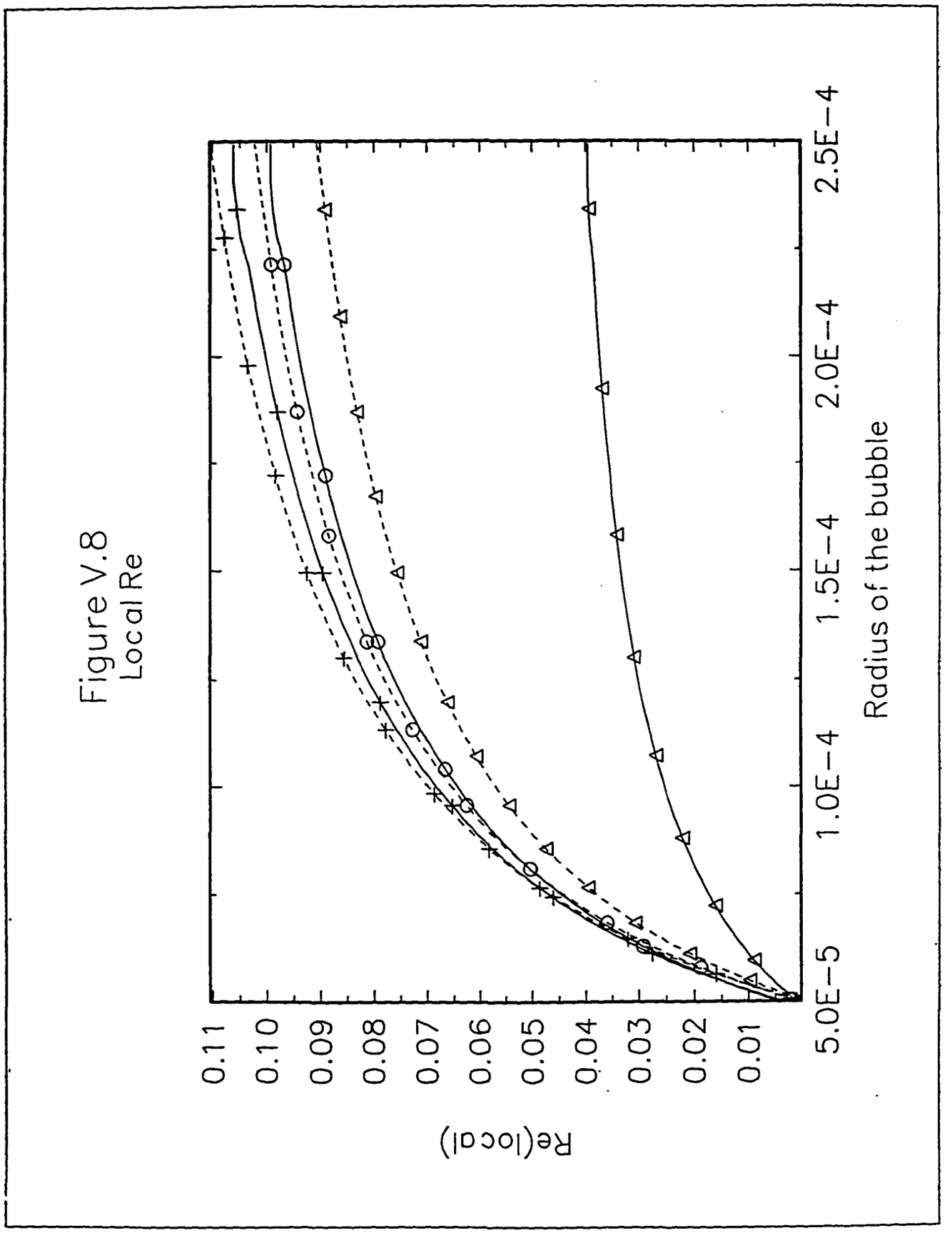

Figure V.8
Local Re

Figure V.9(a)
Growth Time vs. Superheat (Low Density)

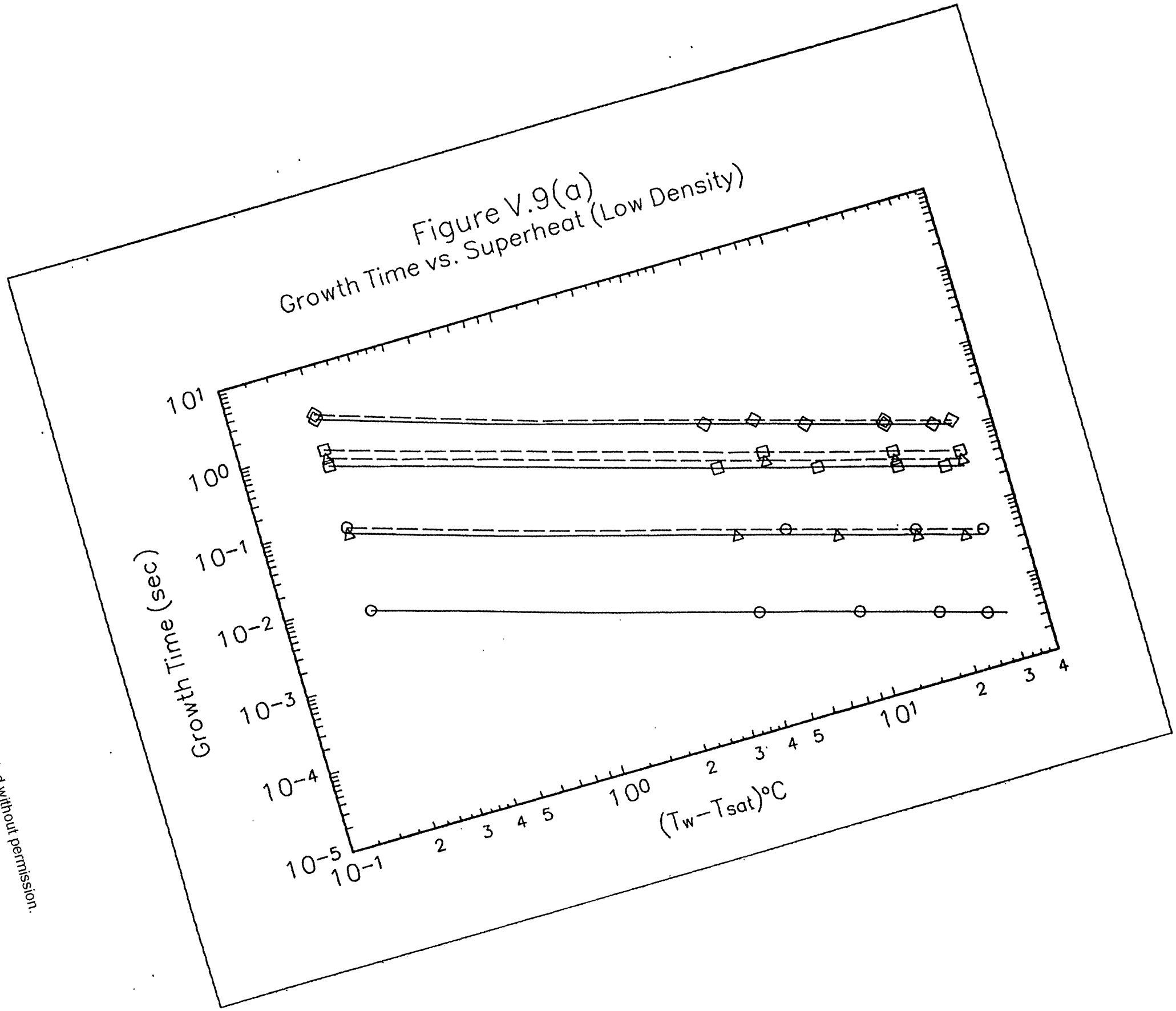

Figure V.9(b)
Growth Time vs. Superheat (High Density)

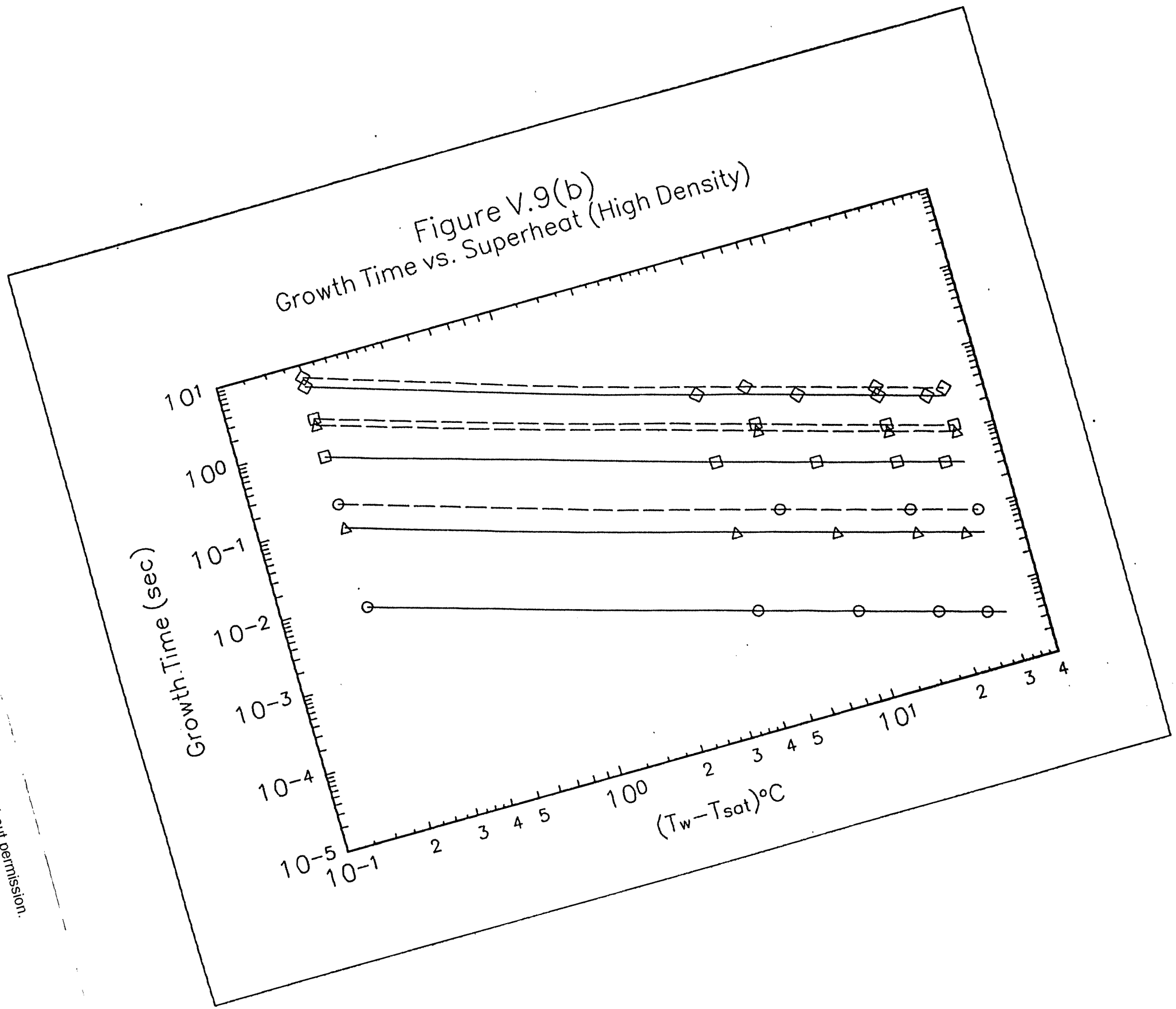

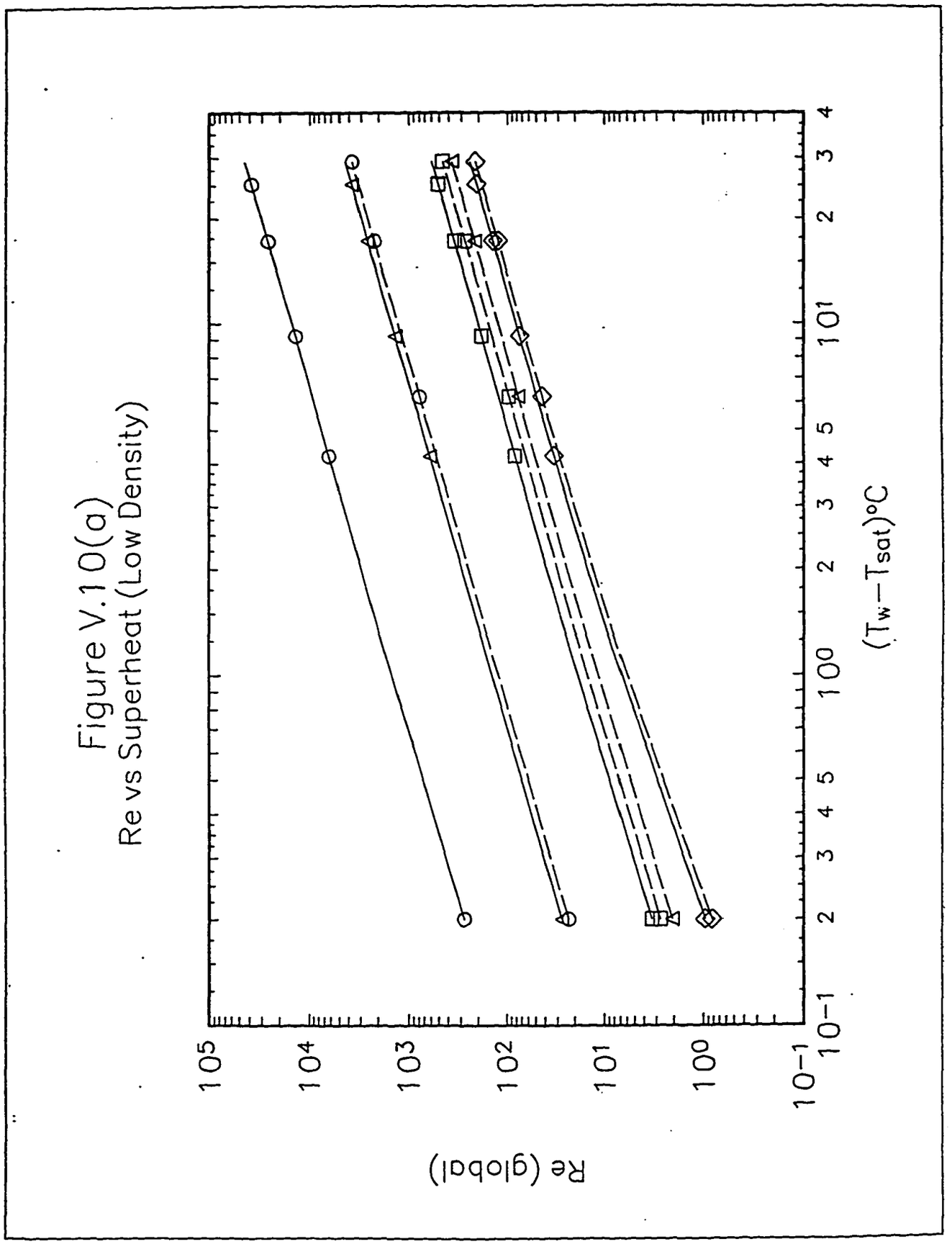

Figure V.10(b)
Re vs Superheat (High Density)

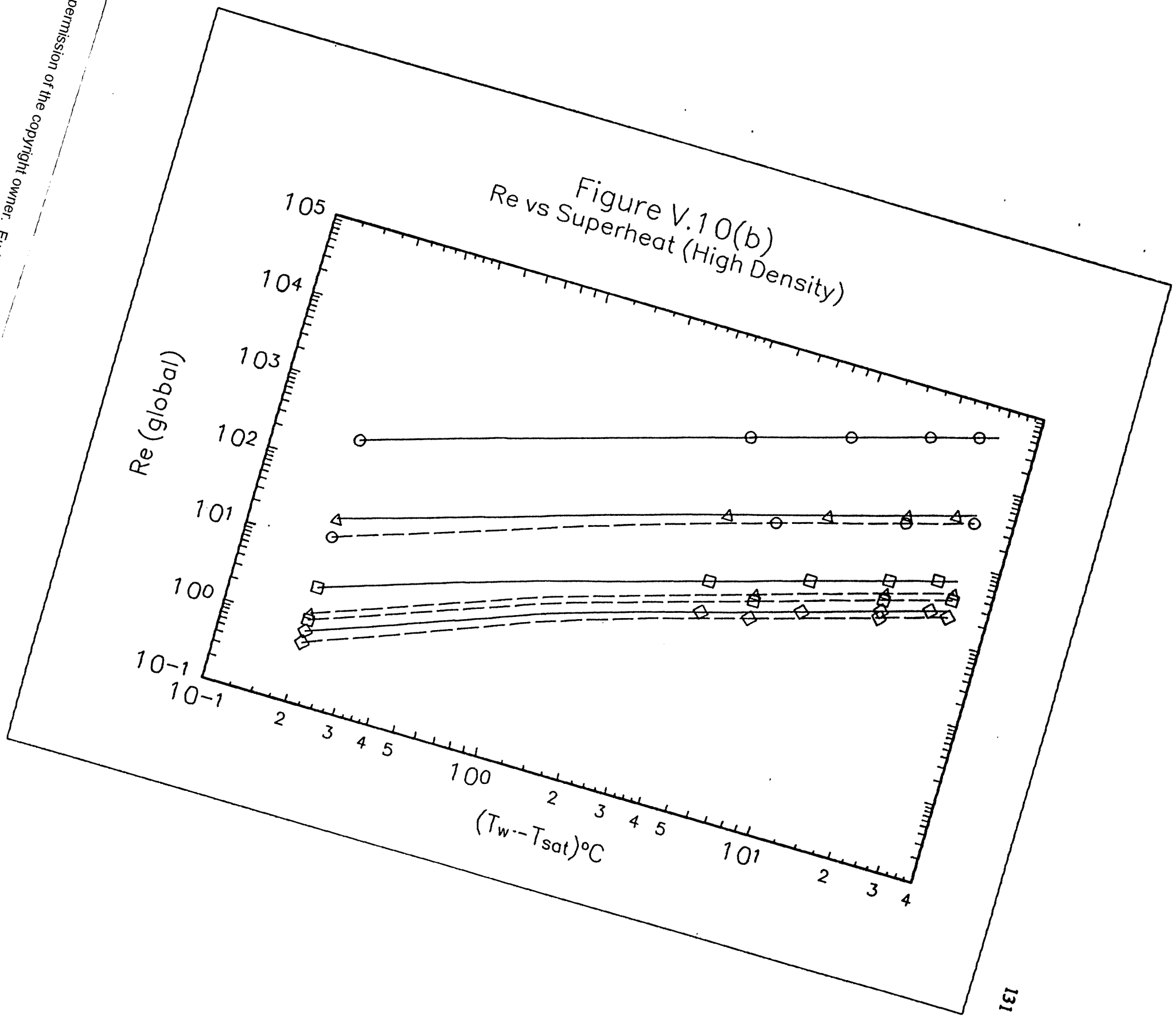

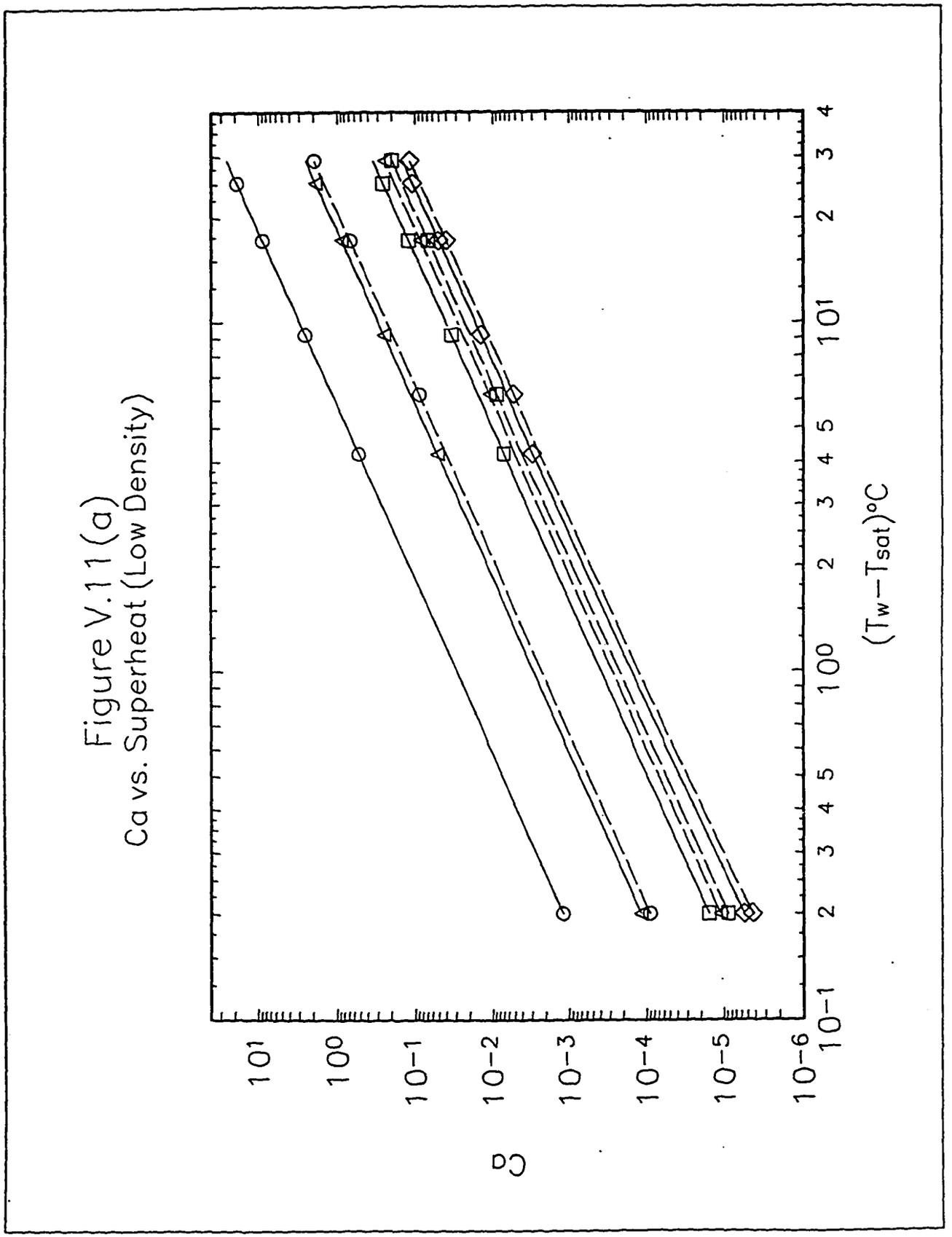

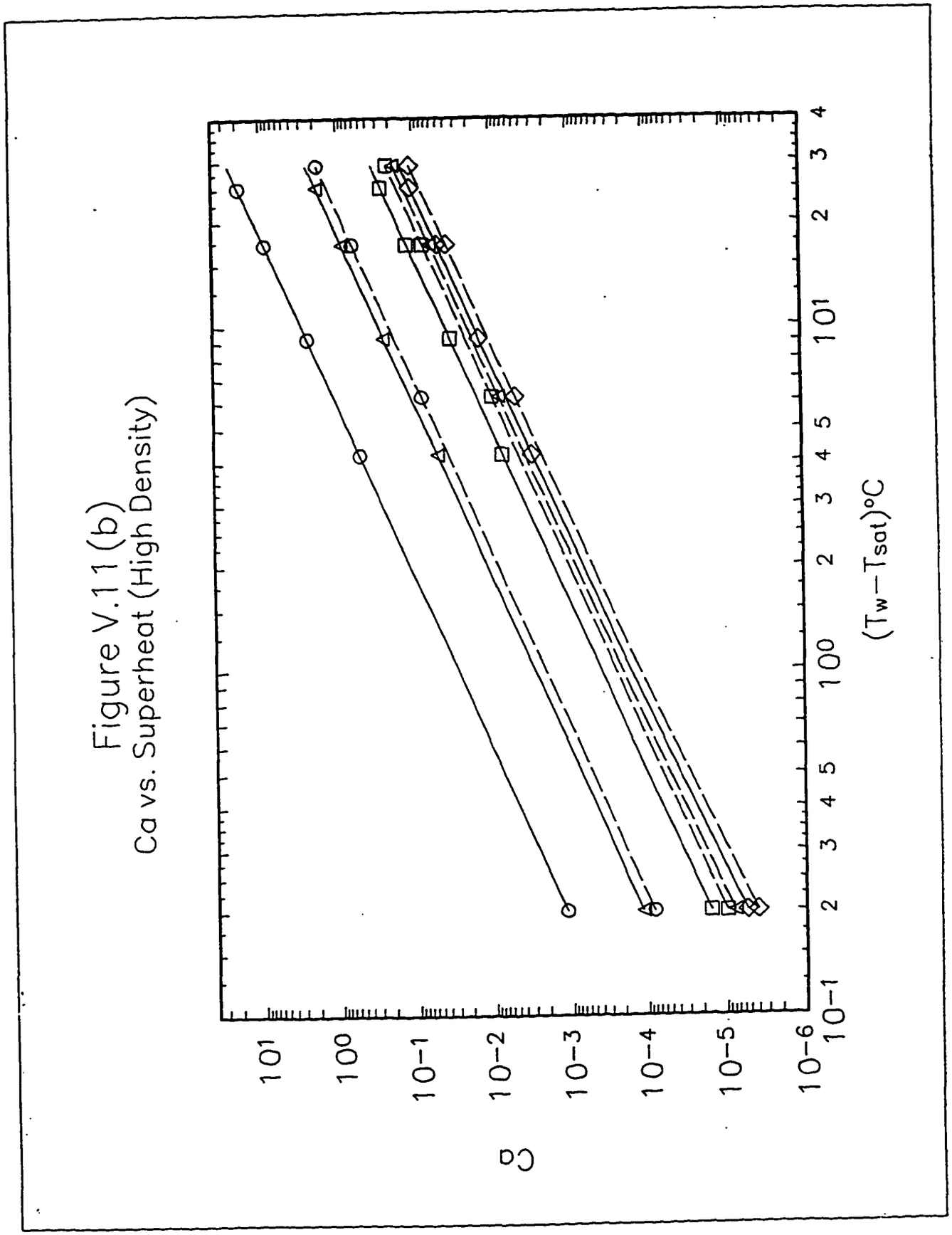

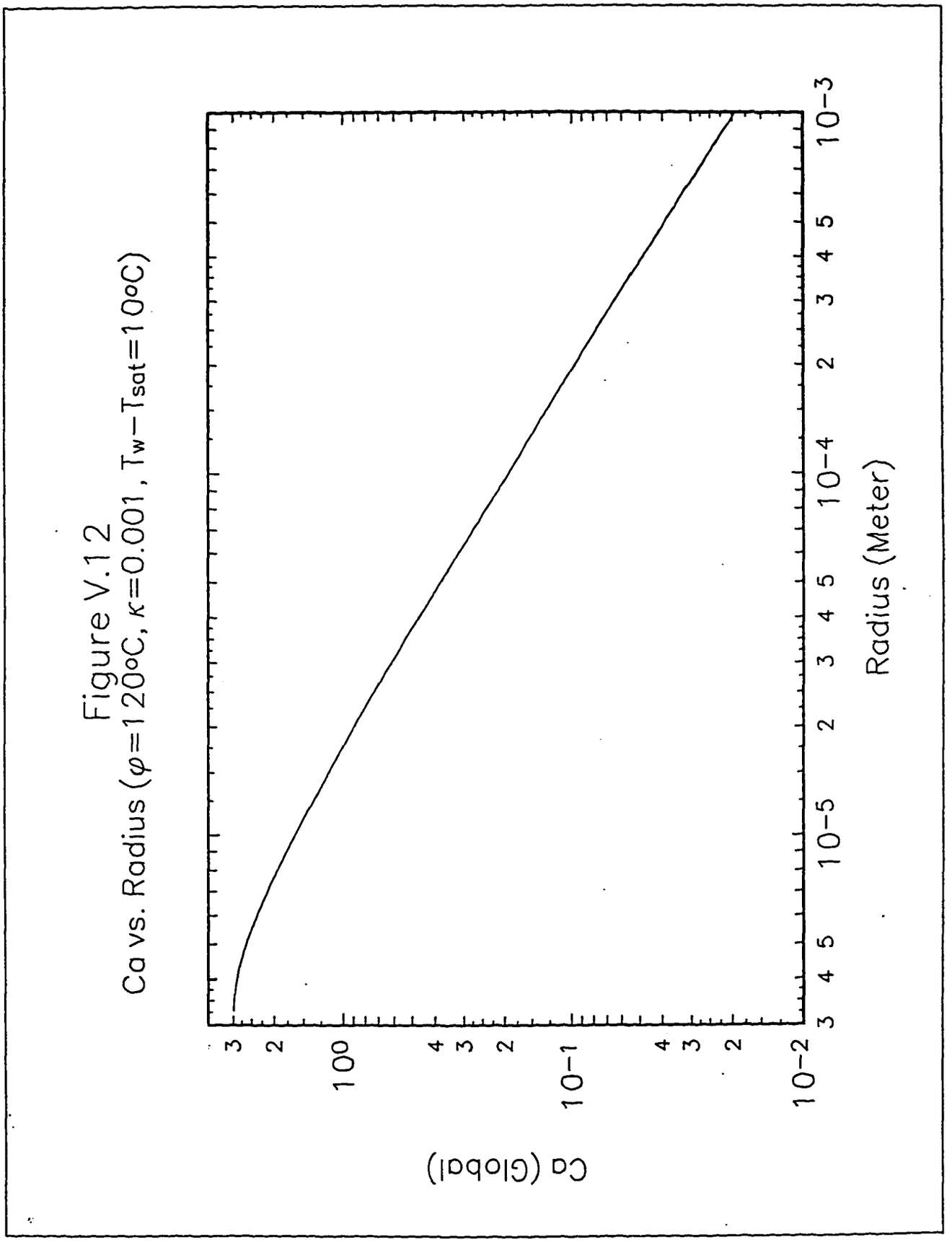

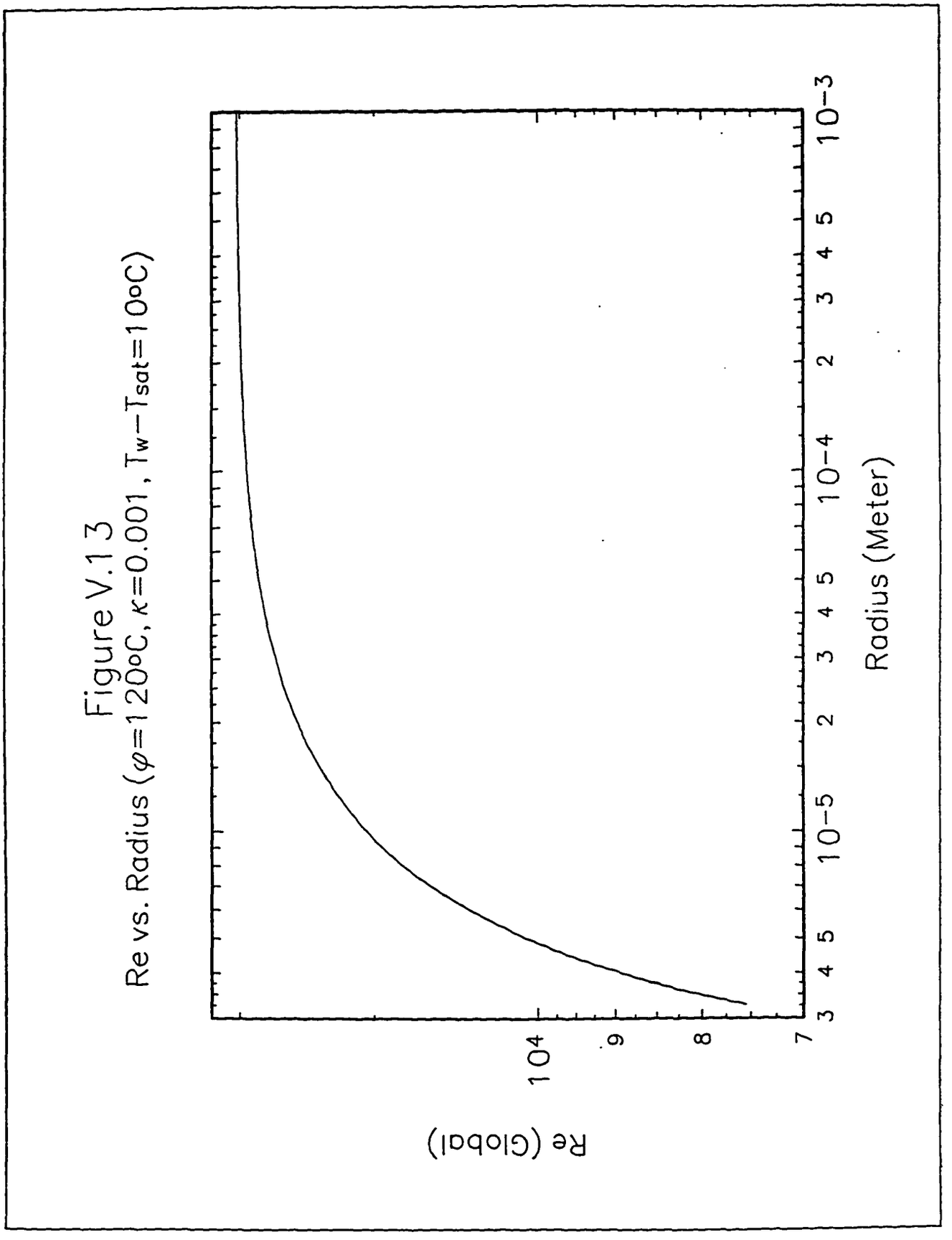

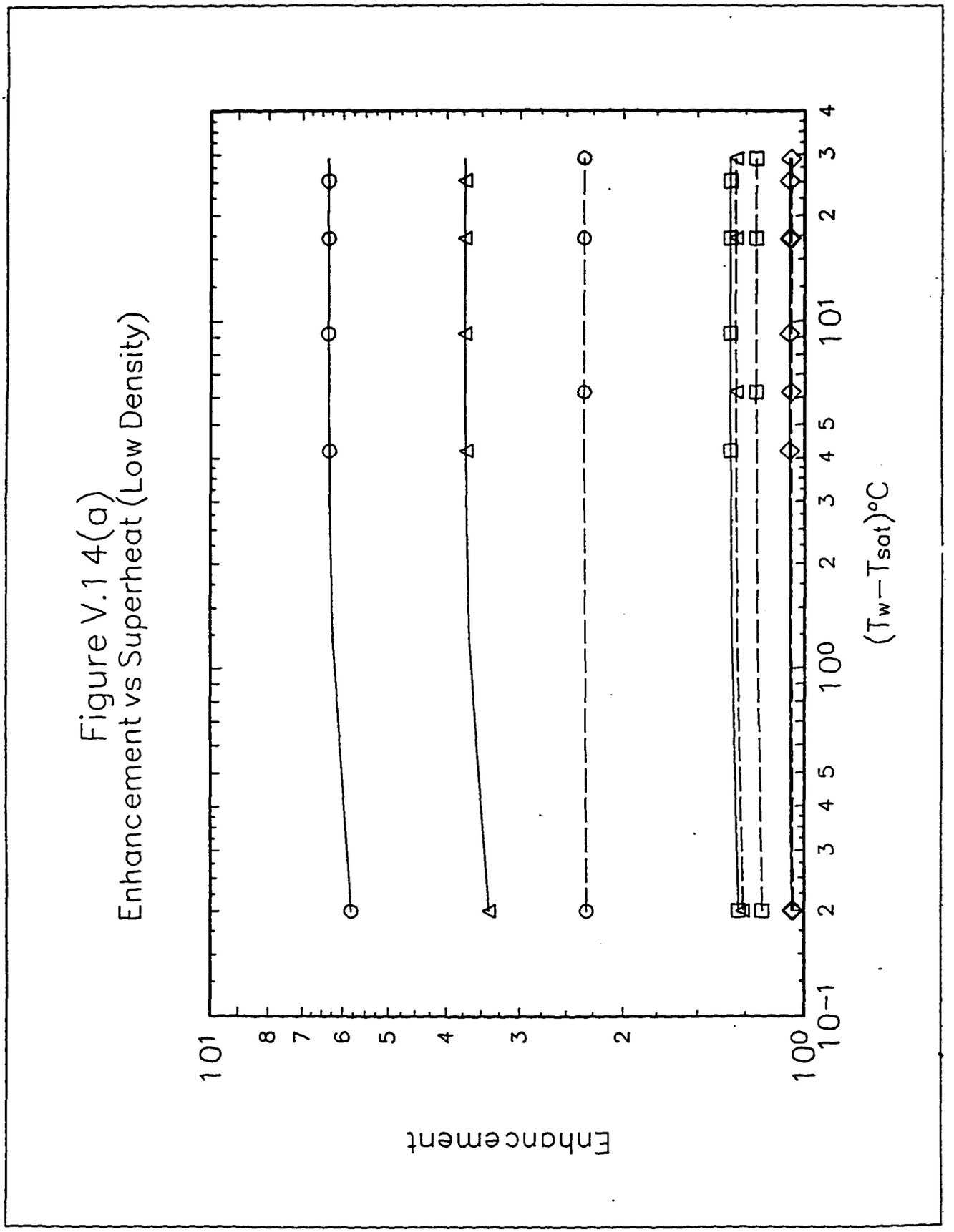

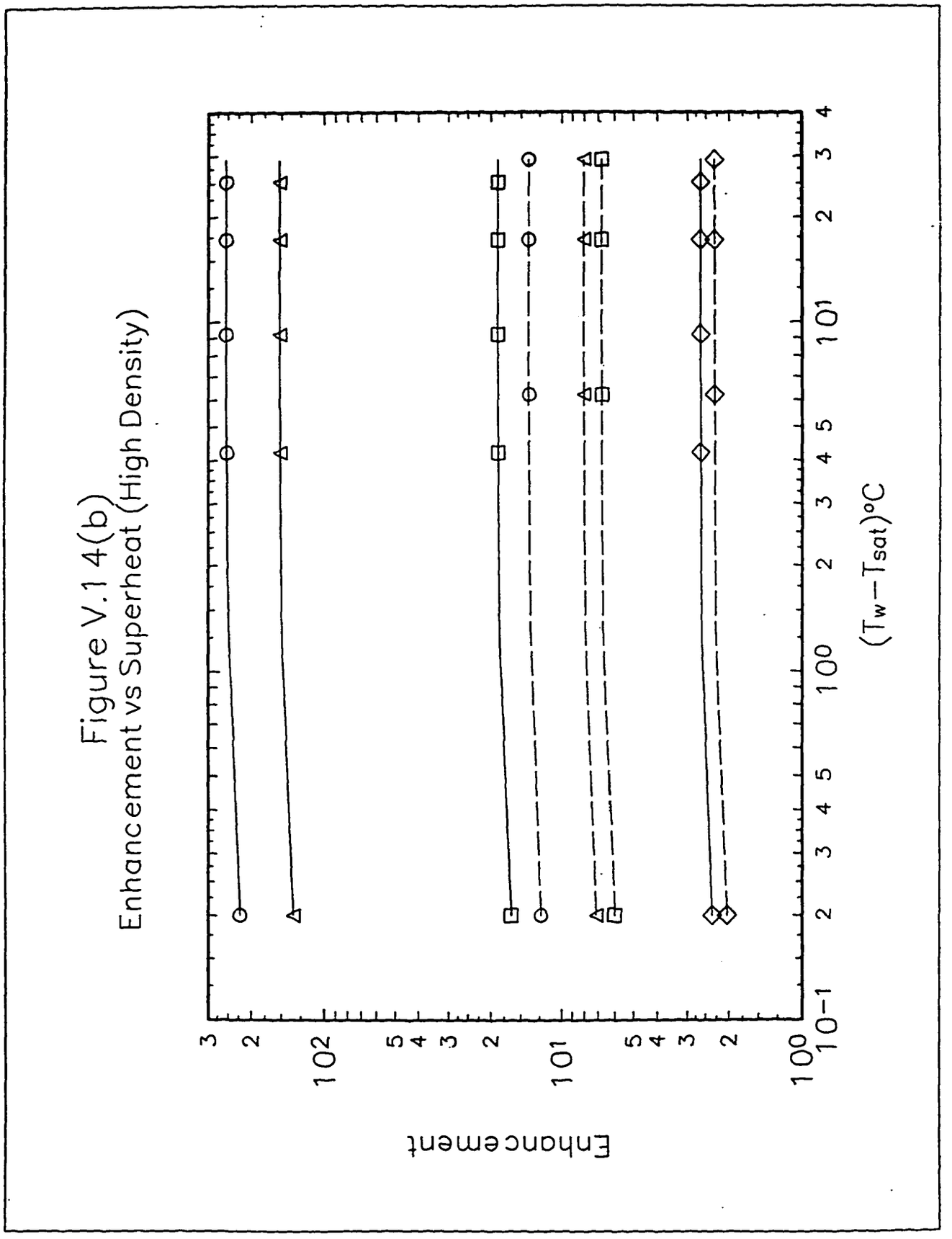

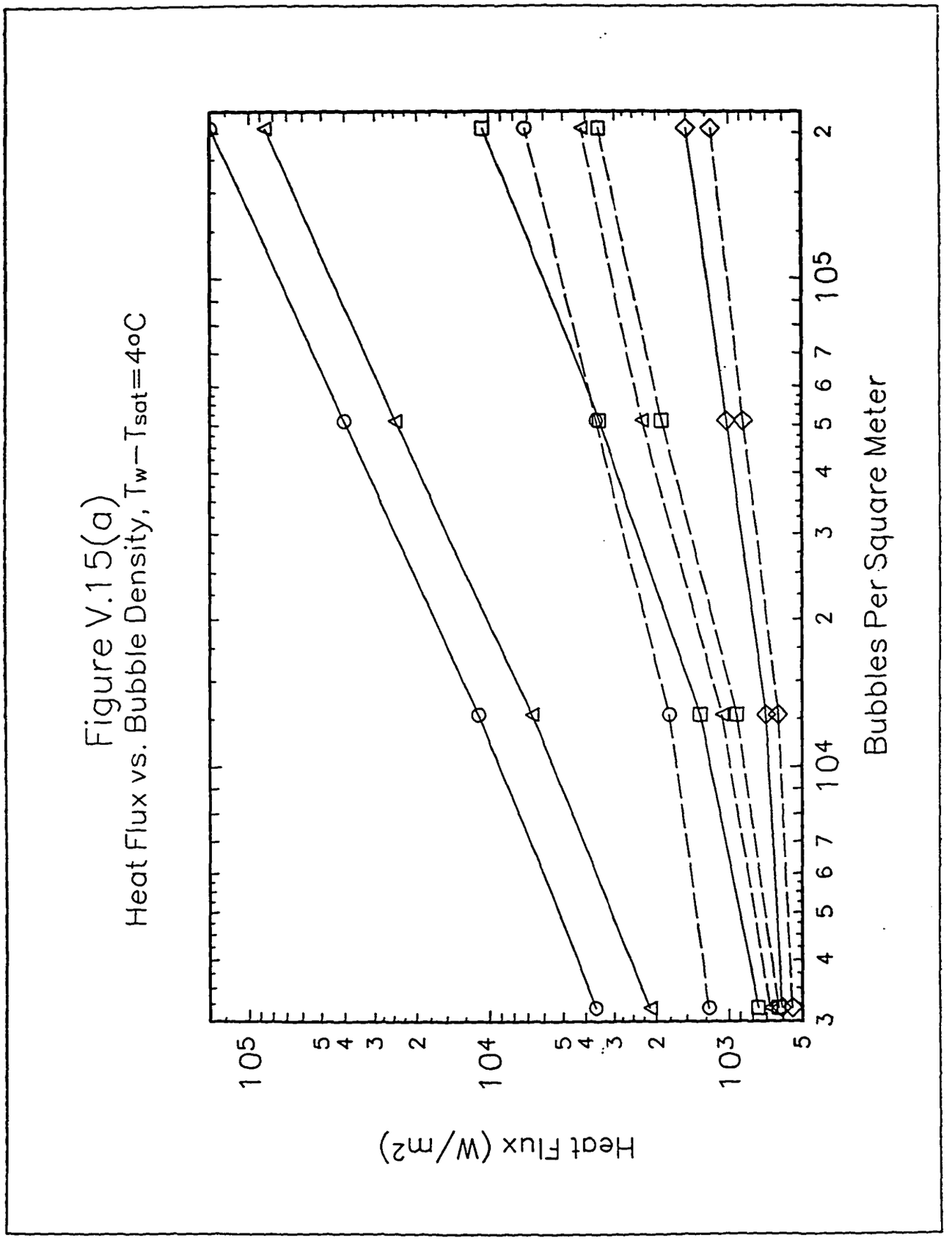

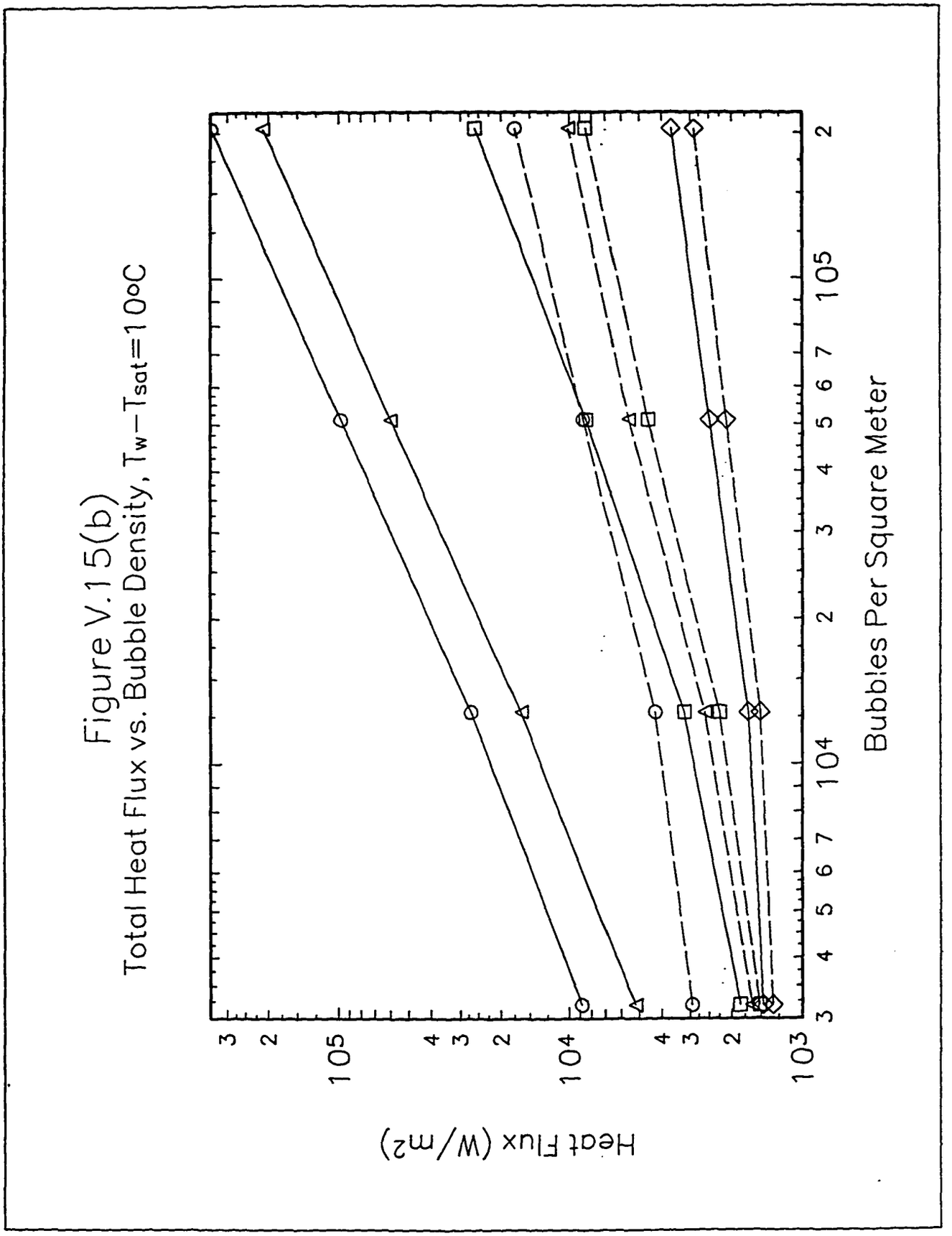

Figure V.15(b)
Total Heat Flux vs. Bubble Density, $T_w - T_{sat} = 10°C$

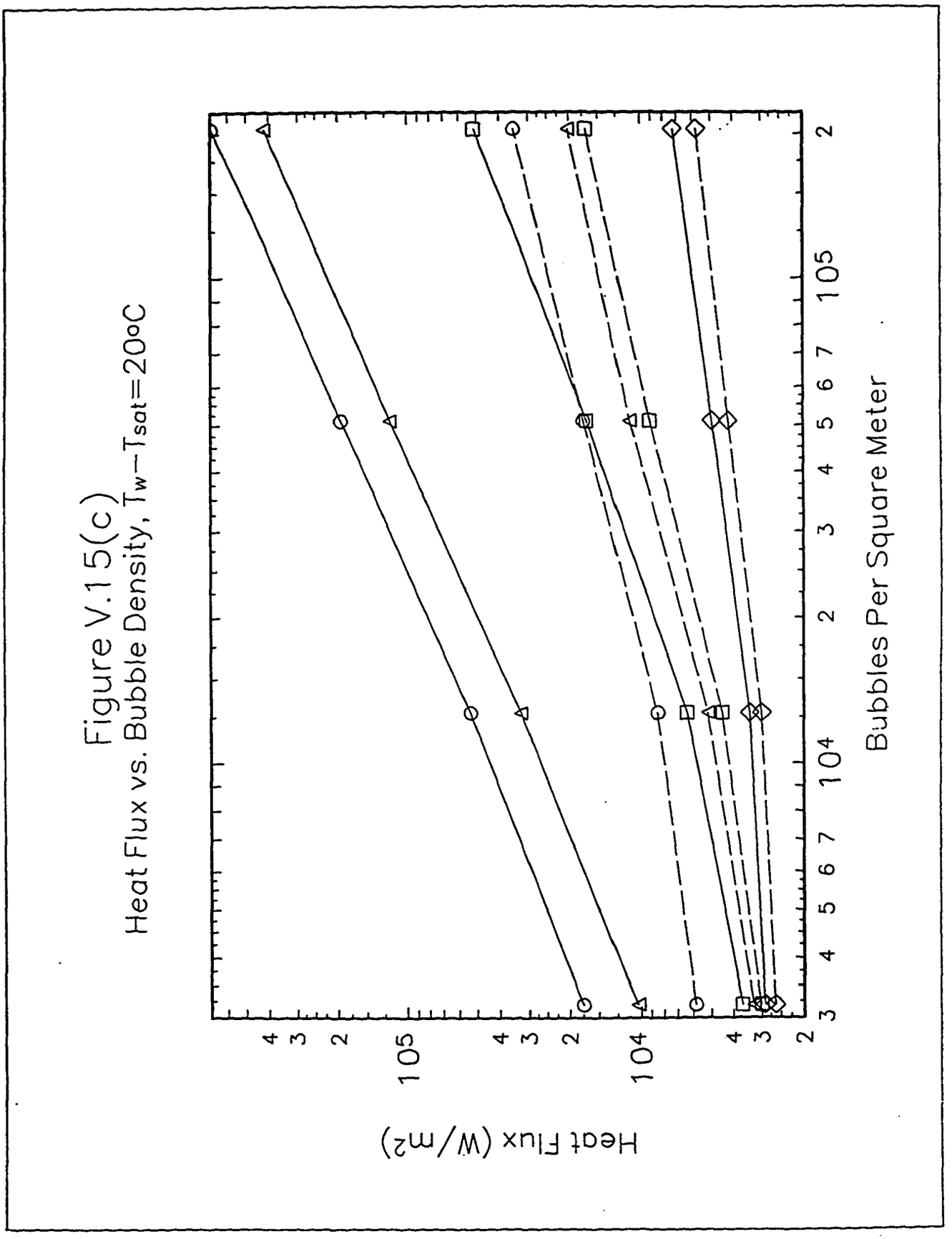

Figure V.15(c)
Heat Flux vs. Bubble Density, $T_w - T_{sat} = 20^oC$

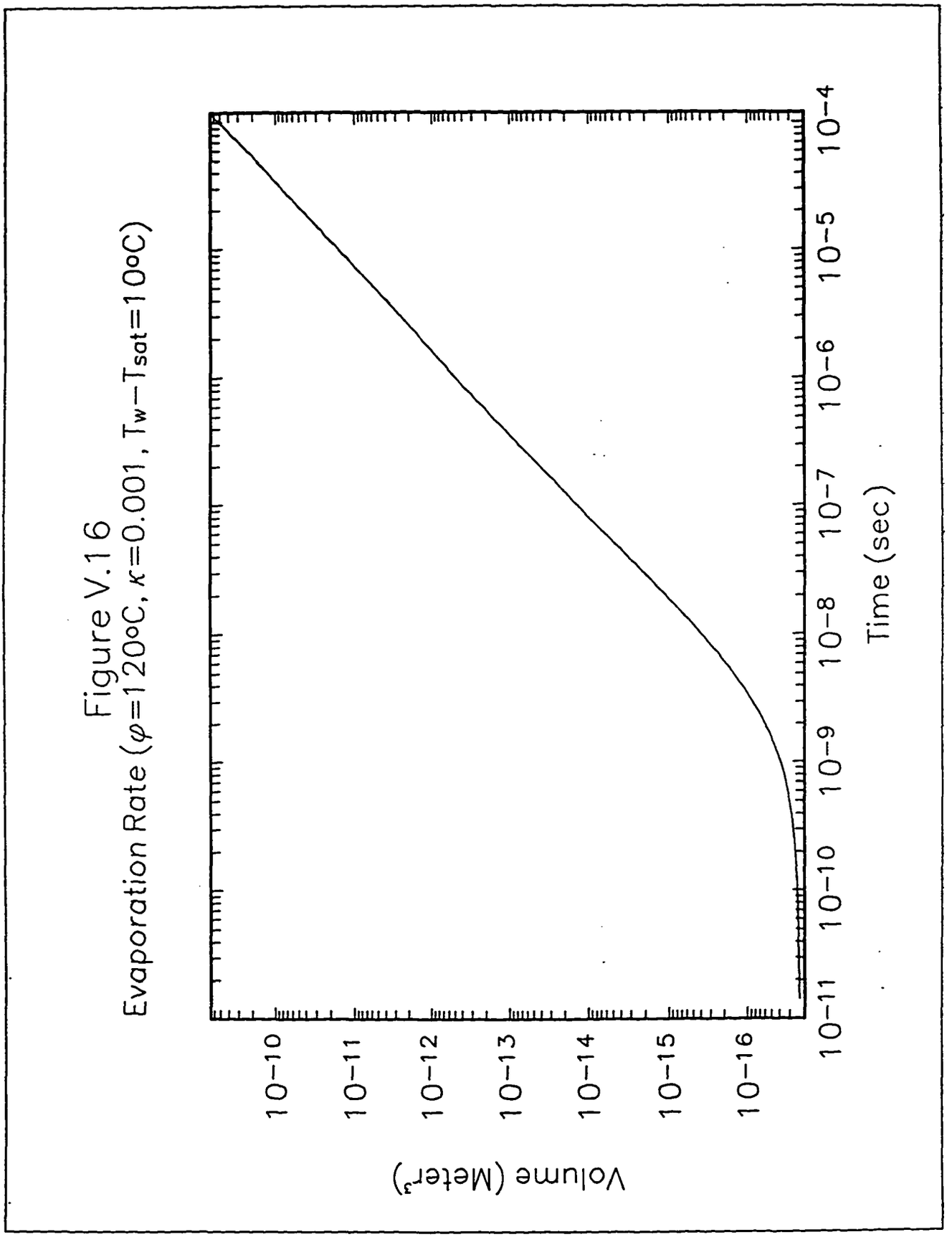

Figure V.16
Evaporation Rate (φ=120°C, κ=0.001, $T_w - T_{sat}$=10°C)

Figure V.17
Reconstruction of the typical boiling curve

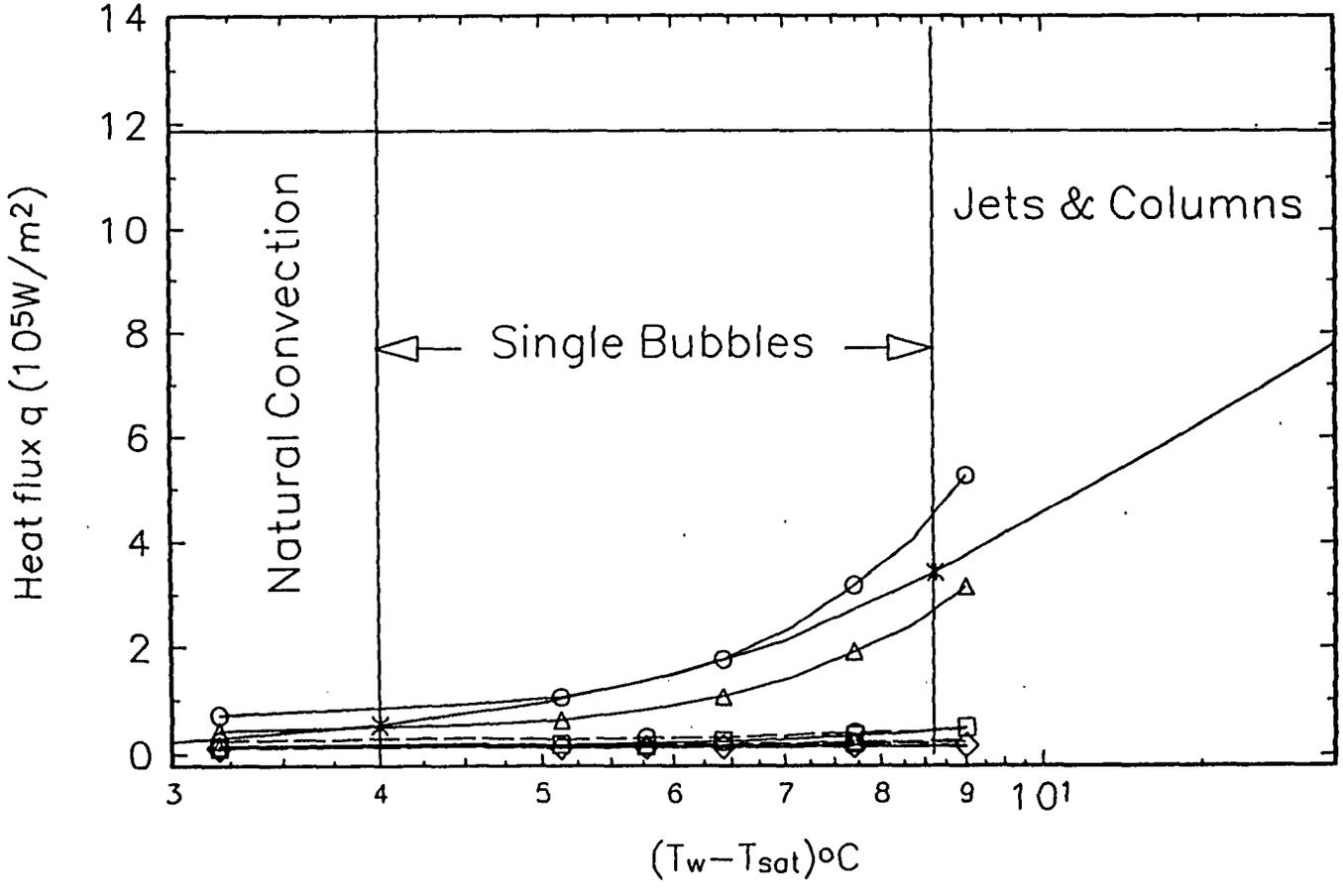

CONCLUSIONS

In this thesis we have studied the fundamental mechanisms of nucleate pool boiling. Because of the tremendous heat transfer enhancement associated with the incipience of the nucleate boiling, this topic has drawn great interests from a vast number of investigators. However, due to the inherent complexity of the problem, very limited precise theoretical progresses have been made this far. In this thesis, we have examined the quasi-static conduction from a heating solid plate to an instantaneously equilibrated vapor bubble in a liquid layer in the limits of small Reynolds and Peclet numbers, Capillary and Bond numbers. We focus on the effects of the solid-liquid conductivity ratios, the attachment or detachment of the embryonic vapor bubbles to the solid-liquid interface, and the number of bubbles per unit area. As an attached bubble grows, there is a small region in the vicinity of the contact line where nearly all of the conduction heat transfer occurs. Scaling lengths by the characteristic dimension of this region keeps the Peclet (and Reynolds) numbers small and ensures that convective transfer is not significant there. The local heat transfer enhancement calculated within this thesis reveals that conductive heat transfer is of sufficient magnitude to account for the observed dramatic heat transfer enhancement associated with nucleate boiling incipience, contrary to conventional interpretations of the phenomenon. Further investigations also reveal the important role that the bubble density plays. In the conduction process regulating this density can change the enhancement of the heat transfer rate by more than a hundred fold in some extreme cases and without the involvement of convective heat transfer.

Future studies on this topic should consider convective and transient terms of both the heat transfer and Navier-Stokes equations, as well as deforming, large, and interacting bubbles. Since the existence of the vapor bubble and its contact regions are so important to the heat transfer enhancement, one simply can not

afford to ignore the effect of the ebullition cycle; one must consider and model dynamic bubble growth, the bubble detachment processes and the processes that determine the bubble frequency, e.g., the waiting period for the local reheating after bubble detachment. Although our studies have shown that the conductive contributions are critical whenever there is a dramatic heat transfer enhancement, the picture will not be complete without explicitly including these other factors.

REFERENCES

1 Bakr, A. A. 1986 *The Boundary Integral Equation Method in Axisymmetric Street Analysis Problems, Lecture Notes in Engineering.* Edited by C. A. Brebbia and S. A. Orszag, Springer-Verlag.

2 A. Calka and R. L. Judd. 1985 Some aspects of the interaction among nucleation sites during saturated nucleate boiling. *Int. J. Heat Mass Transfer* **28**, No.12, 2331-2342.

3 Chen J., Dagan Z., Maldarelli C. 1991 The axisymmetric thermocapillary motion of a fluid particle in a tube. *J. Fluid Mechanics* **233**, 425-437.

4 V. V. Chekanov. 1977 Interaction of centers in nucleate boiling, *Teplofiz, Vysok. Temp.* **15**, 121-128.

5 H. B. Clark, P. S. Strenge, and J. W. Westwater. 1959 Active sites for nucleate boiling. *Chem. Engr. Prog. Symp.* Ser **55**, 29, 103-110.

6 R. I. Eddington, D. B. R. Kenning and A. I. Korneichev. 1978 Comparison of gas and vapor bubble nucleation on a brass surface in water. *Int. J. Heat Transfer* **21**, 855-862.

7 R. I. Eddington and D. B. R. Kenning. 1978 The prediction of low boiling bubble population from gas bubble nucleation experiments. *Proc. 6th Int. Heat Transfer Conference.* Toronto, 1, 275-279.

8 Forster H. K., and Zuber, N. 1955 Dynamics of vapor bubbles and boiling heat transfer. *AIChE J.* **55**, 37-42.

9 M. V. Fyodorov *et al.* 1989 Vapor bubble growth in boiling under quasi-stationary heat transfer conditions in a heating wall. *Intl J. Heat and Mass Transfer* **32**, No. 2. 227-242.

10 Ganatos P., Weinbaum S. and Pfeffer R. 1980 A strong interaction theory for the creeping motion of a sphere between plane parallel boundaries, Part I. *J. Fluid Mechanics* **99**, Part 4, 739-753.

11 Gluckman, M. J., Pfeffer, R. and Weinbaum, S. 1971 A new technique for treating multiparticle slow viscous flow: Axisymmetric flow past spheres and spheroids, *J. Fluid Mech.* **50**, 705.

12 R.W. Graham. 1965 Experimental observations of transient boiling of subcooled water and alcohol on a horizontal surface. *NASA TND-2507.*

13 P. Griffith and J. D. Wallis. 1960 the role of surface conditions in nucleate boiling. *Chem. Eng. Prog. Symp.* Ser. **56**, 30, 49-63.

14 Guy, T. B., and Ledwidge, T. J. 1973 Numerical approach to non-spherical vapor bubble dynamics. *Int. J. Heat Mass Transfer* **16**, 2393-2405.

15 Hsu, Yih-Yun, Graham, Robert W. 1976 *Transport processes in boiling and two-phase systems.* Hemisphere.

16 John H. LienHard. 1989 *A heat transfer textbook.* Second Edition, Prentice-Hall Inc.

17 Lin Huang, Zeev Dagan. 1993 Heat transfer to a bubble suspended in a liquid layer near a solid plate. *33rd Heat Transfer and Fluid Mechanics Institute.* California State University, Sacramento.

18 Lin Huang, David Rumschitzki & Zeev Dagan. 1995 Heat transfer to a bubble in a liquid layer near a solid plate in a finite cell. *Boundary Elements XVII.* Edited by C.A. Brebbia, S. Kim, T.A. Osswald and H. Power, Computational Mechanics.

19 R. L. Judd and C. H. Lavadas. 1980 The nature of nucleation site interaction. *J. Heat Transfer* **102**, 461-464.

20 Kim, Charn-Jung, and Kaviany, Massoud. 1990 A numerical method for phase-change problems. *Int. J. Heat Mass Transfer* **33**, No. 12, 2721-2734.

21 Kutateladze, S. S. 1948 On the transition to film boiling under natural convection, *Kotloturbostroenie* **3**, 10.

22 Lebedev, N. N. 1972 *Special functions and their applications.* Dover.

23 Lee, R. C., and Nydahl, J. E. 1989 Numerical calculation of bubble growth in nucleate boiling from inception through departure. *J. Heat Transfer* **111**, 474-479.

24 Madhaven, S., and Mesler, R. 1970 *A study of vapor bubble growth on surfaces, heat transfer*, 5. Elsevier. Amsterdam.

25 B. D. Marcus. 1963 Experiments *On the mechanism of saturated pool boiling heat transfer*. Ph.D thesis. Cornell University, Ithaca, New York.

26 Rohsenow, W. M. 1952 A method of correlating heat transfer data for surface boiling of liquids. *Trans. ASME*, **74**, 969-976.

27 S. S. Sadhal. 1989 Heat transport to a slowly growing bubble on a solid surface. *Q Jl Mech. Appl. Math.*, **42**, Pt. 4.

28 L. E. Scriven. 1959 On the dynamics of phase growth. *Chem. Engng Sci.* 10(1), 1-14.

29 Snyder, N. W. and Edwards, D. K. 1976 Post conference comments-summary of conference on bubble dynamics and boiling heat transfer, JPL Memo 20*-137, p. 38, June 14*-15, 1956. Reported in Hsu and Graham.

30 Vedat S. Arpaci and Poul S. Larsen 1984 *Convection Heat Transfer*. Prentice-Hall Inc.

31 You S. M., BAR-Cohen A., Simon T. W. 1990 Boiling incipience and nucleate boiling heat transfer of highly-wetting dielectric fluids from electronic materials, *Proc. Second Intersoc Conf.* Thermal Phenom Electron Syst I THERM-II., 90-96.

32 You S. M., Simon T. W., BAR-Cohen A., Tong W. 1990 Experimental investigation of nucleate boiling incipience with a highly-wetting dielectric fluid (R-113), *Intl. J. Heat Mass Transfer*. **33**, No. 1, 105-117.

33 Zijl, W., Ramakers, F. J. M., and Van Stralen, S. J. D. 1979 Global Numerical Solutions of Growth and Departure of a Vapor Bubble at a Horizontal Superheated Wall in a Pure Liquid and a Binary Mixture. *Intl. J. Heat Mass Transfer*. **22**, 401-420.

34 Zuber, N. 1959 *Hydrodynamic aspects of boiling heat transfer*, Ph. D. Thesis, University of California, Los Angeles.

NOMENCLATURE

All primed length are dimensional, while unprimed are those which are scaled by the radius of the vapor bubble, a'.

The temperatures (unprimed) are scaled as $T = (T' - T'_v)/(T'_s - T'_v)$.

a' vapor bubble radius

$\dot{a}' = \kappa_\ell \Delta T'/(a'\rho_v h_{fg})$ time derivative

$\bar{a} = \begin{cases} a & \text{suspended or } \varphi \le \pi/2 \\ c & \varphi \ge \pi/2 \end{cases}$

a_n unknown set of coefficients

$A = 4\pi a^2$ bubble surface area

$A_\pm$ constants

$A^\bullet$ arbitrary constant

$\tilde{A}, \tilde{B}$ constants

$A(\kappa, \varphi)$ function

$B_\pm$ constants

$B(\xi, \eta, \beta)$ function

c' dry spot's radius

$c_1(\chi)$, $c_2(\chi)$, $c_3(\chi)$, $c_4(\chi)$ unknown functions

$Bond = (g\Delta\rho a^2)/\sigma = (g(\rho_\ell - \rho_v)a^2)/\sigma$ Bond number

$Ca = u'\mu/\sigma$ Capillary number

c_ℓ thermal conductivity

c_p specific heat of water with constant pressure

C_{sf} surface correction factor

d' distance from the center of the sphere to the liquid-solid interface

$\bar{e}$ unit vector

$E_\pm, F_\pm$ unknown constants in collocation techniques

$E(m)$ complete elliptic integrals of first kind $E(m) = \int_0^{\frac{\pi}{2}} \sqrt{1 - m^2 \sin^2 \alpha}\, d\alpha$

$F(\lambda) = \cosh \lambda h \sinh \lambda H + \kappa \sinh \lambda h \cosh \lambda H$

$g_\pm(\xi, \eta)$ functions

h' solid plate thickness

h_{fg} latent heat

H' liquid layer thickness

H_η, H_ξ metric factor

$j_s := \dfrac{j'_s a'}{\kappa_s (T'_s - T'_v)}$ temperature gradient

$J_0(x)$ Bessel function of zeroth order

$K(m)$ complete elliptic integrals of second kind

$$K(m) = \int_0^{\frac{\pi}{2}} \frac{d\alpha}{\sqrt{1 - m^2 \sin^2 \alpha}}$$

$$m := \frac{2\sqrt{R_p R_q}}{\sqrt{[(R_p + R_q)^2 + (Z_p - Z_q)^2]}}$$

n_{R_q}, n_{Z_q} normal vector componenets of point q on the surface Γ_q.

$\bar{n}$ normal unit vector

N Number of bubbles

$Nu = Qa'/\left[A\kappa_\ell (T_s' - T_v')\right]$, Nusselt number

$Pe = a'\dot{a}'/\alpha_\ell = RePr_\ell$ liquid Peclet number

$P_n(x)$ Legendre polynomials

$Pr_\ell = \nu_\ell/\alpha_\ell$ liquid Prandtl number

P_v Bubble's interior pressure

Q_ℓ heat flux across the liquid-solid interface of the composite cell without the bubble

Q_s heat flux across the liquid-solid interface of the composite cell with the bubble

Q_v total heat flux into the bubble

$\bar{r}_p$ point inside the finite region of interest of volume V

$\bar{r}_q$ point on the boundary ∂V.

$r = r'/a'$ $R = R'/a'$ $Z = Z'/a'$ dimensionless length scales

r_b' radius of the spherical bubble

r_b'' and r_b''' two principal radius of curvature of a nonspherical bubble

(r', θ, ψ) spherical coordinates

(R', Z', ψ) Cylindrical coordinates

R_c' Radius of the cell

$Re = a'\dot{a}'/\nu_\ell$ Reynold's number

s Radian measured from bubble's central line or contact line

$t_d \cong a'^2/\alpha_\ell$, diffusive time scale

$t_g \cong a'/\dot{a}'$ growth time scale

$t_s \cong (a'\rho_\ell \nu_\ell)/\sigma$ surface tension time scale

$t_v \cong a'^2/\nu_\ell$ viscous time scale

$T^{spherical}$ Collocation solution in spherical coordinates

$T^{cylindrical}$ Collocation solution in cylindrical coordinates

T_f' free surface temperature (boundary condition), dimensional or dimensionless

$T_\pm'$ liquid/solid temperature

T_s' solid wall temperature (boundary condition)

T_v' saturated vapor temperature (boundary condition)

T_{sv}' solid-vapor interfacial temperature

$T_{s\ell}' := \dfrac{T_f'\kappa h' + T_s'H'}{\kappa h' + H'}$ solid-liquid interfacial temperature far from a bubble

T_{sat}' saturation temperature for a flat liquid-vapor interface.

$T = (T' - T_v')/(T_s' - T_v')$ dimensionless temperature

$\hat{T} := (T' - T_\infty')/(T_v' - T_\infty')$ dimensionless temperature in toroidal coordinates

$T_\pm^1$ dimensionless solutions when $T_f|_{z = H-d} = 1$

$T_\pm^0$ dimensionless solutions when $T_f|_{z = H-d} = 0$

$\tilde{T}_\pm(u, v)$ dimensionless temperature for large bubbles

u' velocity of the vapor-liquid interface

$\alpha = \alpha_1 + i\alpha_2$ complex plane

$\alpha_c = R_c - c$ distance from the edge of dry spot to the edge of the cell, on the solid-liquid interface

α_ℓ liquid thermal diffusivity

$\Delta T' := T_{s\ell}' - T_v' = \dfrac{(T_f' - T_v')\kappa h' + (T_s' - T_v')H'}{\kappa h' + H'}$ temperature difference

∇ gradient operator

∇^2 Laplace's operator

ν_ℓ liquid kinetic viscosity

φ contact angle

κ_s solid thermal conductivity

$\kappa_\ell = \rho_\ell c_\ell \alpha_\ell$ liquid thermal conductivity

κ_v vapor thermal conductivity

$\kappa = \kappa_\ell/\kappa_s$ conductivity ratio

$\delta = (d - a)/2a$ dimensionless gap thickness between the bubble and the solid plate

(ξ, η) toroidal coordinates

λ H/h

μ liquid viscosity

Φ and $\nabla\Phi$ are asymmetric Green's function

$\phi_1(\tau)$ - $\phi_4(\tau)$ unknown functions

ρ_ℓ liquid density

ρ_s solid density

ρ_v vapor density

σ surface tension

$\sigma_{s\ell} = Q_s/Q_\ell$ heat transfer enhancement due to the bubble's presence

$\sigma_{vs} = Q_v/Q_s$ fraction of heat leaving the solid that contributes to vaporization

Γ_q Boundary surface enclosing the domain

$\omega = (\overline{a} / R_c)^2$ bubble density (ratio of area covered by vapor over that of the total cell)

$\omega := u + iv = Ln\frac{\alpha - \alpha_C}{\alpha + \alpha_C} = \ln\frac{r_C}{r_A} + i(\theta_C - \theta_A)$ is the transformation in large cell approximation